NASA/CR-20240000278

Hybrid Thermally Efficient Core (HyTEC)
HyTEC Phase 1—Combustor
Final Report

Dan Kirtley, Michael Guerette, Gerardo Salazar, and D'Arcy Stone
GE Aerospace, Evendale, Ohio

June 2024

NASA STI Program Report Series

Since its founding, NASA has been dedicated to the advancement of aeronautics and space science. The NASA scientific and technical information (STI) program plays a key part in helping NASA maintain this important role.

The NASA STI program operates under the auspices of the Agency Chief Information Officer. It collects, organizes, provides for archiving, and disseminates NASA's STI. The NASA STI program provides access to the NTRS Registered and its public interface, the NASA Technical Reports Server, thus providing one of the largest collections of aeronautical and space science STI in the world. Results are published in both non-NASA channels and by NASA in the NASA STI Report Series, which includes the following report types:

- TECHNICAL PUBLICATION.
  Reports of completed research or a major significant phase of research that present the results of NASA Programs and include extensive data or theoretical analysis. Includes compilations of significant scientific and technical data and information deemed to be of continuing reference value. NASA counterpart of peer-reviewed formal professional papers but has less stringent limitations on manuscript length and extent of graphic presentations.

- TECHNICAL MEMORANDUM.
  Scientific and technical findings that are preliminary or of specialized interest, e.g., quick release reports, working papers, and bibliographies that contain minimal annotation. Does not contain extensive analysis.

- CONTRACTOR REPORT.
  Scientific and technical findings by NASA-sponsored contractors and grantees.

- CONTRACTOR REPORT.
  Scientific and technical findings by NASA-sponsored contractors and grantees.

- CONFERENCE PUBLICATION.
  Collected papers from scientific and technical conferences, symposia, seminars, or other meetings sponsored or co-sponsored by NASA.

- SPECIAL PUBLICATION.
  Scientific, technical, or historical information from NASA programs, projects, and missions, often concerned with subjects having substantial public interest.

- TECHNICAL TRANSLATION.
  English-language translations of foreign scientific and technical material pertinent to NASA's mission.

Specialized services also include organizing and publishing research results, distributing specialized research announcements and feeds, providing information desk and personal search support, and enabling data exchange services.

For more information about the NASA STI program, see the following:

- Access the NASA STI program home page at http://www.sti.nasa.gov

NASA/CR-20240000278

Hybrid Thermally Efficient Core (HyTEC)
HyTEC Phase 1—Combustor
Final Report

Dan Kirtley, Michael Guerette, Gerardo Salazar, and D'Arcy Stone
GE Aerospace, Evendale, Ohio

Prepared under Contract 80GRC021CA010

National Aeronautics and
Space Administration

Glenn Research Center
Cleveland, Ohio 44135

June 2024

Acknowledgments

This material is based upon work supported by the National Aeronautics and Space Administration under contract Number 80GRC021CA010 with Linda Nabors (NASA Glenn) as Contracting Officer and Martha Jaskowiak (NASA Glenn) as Technical Monitor. The authors are grateful for the contributions of the following individuals at GE Aerospace, GE Global Research, and NASA Glenn Research Center personnel who made significant contributions to the project and allowed for the successful execution and completion of the task objectives.

Swirler Attachment Contributors:

Gerardo Salazar (GEA), Dan Kirtley (GEA), Nathan Hermanson (GEA), Gil Adkins (GEA), Dustin Wirick (GEA), Janith Samarasinghe (GE GRC), and Mathew Thariyan (GE GRC).

Nickel Diffusion Contributors:

D'Arcy Stone (GEA), Rob Fecke (GEA), Alex Mayfield (GEA), Roy M. Sullivan (NASA GRC), Daryl Werner (GEA), Elizabeth Young (Georgia Institute of Technology), and Bob Zhou (GEA).

EBC Advancement Contributors:

Michael Guerette (GEA), Sivakumar Ramasamy (GEA), Guruvenket Srinivasan (GEA), Suresh Viswanathan (GEA), Glen Kirby (GEA), Stephen Pontsler (GEA), Mano Manoharan (GEA), Claire Henderson (GE Research), Julin Wan (GE Research), Vidya Ramaswamy (GE Research), Reza Sarrafi-Nour (GE Research), Michael Presby (NASA GRC), Martha Jaskowiak (NASA GRC), Kang Lee (NASA GRC), Roy M. Sullivan (NASA GRC), and Josh Stuckner (NASA GRC).

This work was sponsored by the Advanced Air Vehicles Program at the NASA Glenn Research Center.

Level of Review: This material has been technically reviewed by NASA expert reviewer(s).

This report is available in electronic form at https://www.sti.nasa.gov/ and https://ntrs.nasa.gov/

NASA STI Program/Mail Stop 050
NASA Langley Research Center
Hampton, VA 23681-2199

Contents

List of Figures

List of Tables

List of Equations

List of Acronyms

Acronym	Definition
5HP	5-Hole Probe
ADP	Aero Design Point
APS	Air Plasma Spray
ASTM	American Society for Testing and Materials
ATAG	Air Transport Action Group
ATMS	Advanced Thermal Management Systems
BOS	Background Oriented Schlieren
CDR	Conceptual Design Review
CFD	Computational Fluid Dynamics
CMAS	Calcium-Magnesium-Aluminum-Silicate
CMC	Ceramic Matrix Composite
CTE	Coefficient of Thermal Expansion
CUI	Controlled Unclassified Information
DAQ	Data Acquisition System
DCR	Design Consensus Reviews
DDR	Detailed Design Review
EBC	Environmental Barrier Coating
FAR	Fuel Air Ratio or Full Annular Rig
FAR36	Fuel Air Ratio for the combustor
FRAP	Fast-Response Aerodynamic Probe
GEA	General Electric Aerospace
GRC	Global Research Center
HCF	High Cycle Fatigue
HE	Hybrid Electric
HTP	High Temperature & Pressure
HW	Hot Wire
HyTEC	Hybrid Thermally Efficient Core
IATA	International Air Transport Association
KPP	Key Performance Parameter
LTAG	Long-Term Aspirational Goal
NASA	National Aeronautics and Space Administration
NDTL	Notre Dame Turbomachinery Lab
P3	Pressure of air at inlet of combustor (Feed Pressure)
P4	Pressure inside of the combustor
P4’	P4 pressure variation inside combustor
PDR	Preliminary Design Review
PL	Proportionality Limit
PLC	Programmable Logic Controller
PSP	Pressure Sensitive Paint
PSV	Pre Swirl Vane
RANS	Reynolds Averaged Navier-Stokes
RCA	Root Cause Analysis
RFR	Red Flag Review
RPM	Rotations Per Minute
SEM	Scanning Electron Microscopy
Si	Silicon

SOA	State of the Art
SS	Steady State
T3	Temperature of air at inlet of combustor
TCA	Tunable Combustor Acoustics
TGO	Thermally Grown Oxide
TP	Thrust Piston
TPM	Technical Performance Measures
TRL	Technology Readiness Level
TRR	Test Readiness Review
TRT	Transonic Research Turbine
TTF	Target To Fire
UNFCCC	United Nations Framework Convention on Climate Change
VFD	Variable Frequency Drive
ΔP/P	Dome pressure drop over feed pressure

Executive Summary

The objective of the HyTEC – Combustor Technology project is to develop technology for a compact, low emissions, rich-burn combustor that maintains a high-level of durability. To accomplish this, the combustor will incorporate CMC liners and a CMC Dome to enable improved air utilization for mixing and NOx reduction. In particular, three technology areas were matured: metallic swirler attachment to the CMC dome, Nickel diffusion in CMC, and EBC advancements with improved durability. The maturation of these technology areas is critical to successfully designing a combustor for an engine intended to demonstrate increased thermal efficiency with integrated high-power density-core engine technologies.

As part of the project, multiple swirler attachment architectures were matured through the design process, manufactured, and tested in simulated engine conditions. These architectures utilized two different approaches to attachment: a pressure loaded approach and a clamped approach. Each approach required testing at simulated engine conditions to mature the technology. These tests were developed to ensure that the probable failure mechanisms for each architecture were assessed relative to its long-term durability. After successfully testing both approaches, the pressure loaded approach was chosen based on its simplicity and its similarity to the attachment approach used on lean burn combustors. Finally, this successful testing resulted in the swirler attachment technology achieving TRL 4 status.

Another aspect of concern with the metallic swirler attachment is the potential for nickel diffusion into the CMC to cause durability shortfalls. A series of tests were completed to understand both the amount of nickel that is expected to diffuse into the CMC and the effect this diffusion will have on mechanical properties of the CMC. After successfully completing this testing, the reduction in local mechanical properties was found to not have an impact on the overall durability of the CMC Dome.

To further improve the overall durability, three different EBC coating architectures were also studied. Coupons were produced using each coating and subjected to a series of laboratory testing. One coating was found to have an overall superior durability in laboratory testing and survived rig testing without indication of degradation. This successful testing resulted in the EBC technology achieving TRL 5 status.

Overall, a design approach was successfully down-selected that achieves both the TPM requirements and the need for TRL 4+ status. This design incorporates a pressure loaded swirler attachment with an improved EBC coating (Architecture 1). This combination allows the continued use of a CMC dome and results in an improved durability for the proposed compact core combustor.

1. Introduction

Through its history, GE Aerospace (GEA) has established a strong tradition of investing in revolutionary technologies and has had the pleasure of doing so for some time now in partnership with NASA across numerous projects. The HyTEC project has continued this tradition with a focus on a suite of compact core technologies that aim to gain significant fuel burn reductions while maintaining or improving durability against the current best in class.

Concerns about the impact of climate change are increasing globally, and along with the greater focus on climate change there is a greater focus on the contributions of the aviation sector. The aviation industry has recognized this and in October 2021, International Air Transport Association (IATA) and Air Transport Action Group (ATAG) (where GEA is a member), increased the industry commitment by pledging to achieve zero Carbon (CO_2) emissions from aviation by 2050. This view is consistent with the corresponding goal laid out in the FAA's 2021 Aviation Climate Action Plan. Moreover, last year at the 41st International Civil Aviation Organization Assembly, a long-term global aspirational goal (LTAG) for international aviation of net-zero carbon emissions by 2050 was established in support of the UNFCCC (United Nations Framework Convention on Climate Change) Paris Agreement's temperature goal. While it is clear a combination of measures will be necessary to achieve these goals, GEA believes the most credible path to doing so is through aggressive product innovations, which will facilitate a step-change improvement in the fuel efficiency of the fleets and serve as the bedrock of technologies for the future generation of products.

It is also clear that significantly impacting these targets requires a concentrated focus on the single aisle market. As of 2019, single aisle aircraft accounted for ~45% of the industry's carbon dioxide (CO_2) burden – the largest contribution from any market segment. Furthermore, the continuation of trends, such as seat upgauging and increased travel range for single aisle aircrafts, will continue driving share shift away from twin aisles and towards single aisles – thereby increasing both the market opportunity and the associated sustainability burden contributed from this segment. Put simply, impacting the aviation industry CO_2 emissions requires direct and immediate action in the single aisle space.

Realizing the critical need for a step change in capability order to meet industry commitments, GEA has developed an ambitious $2B+ technology demonstration program focused on enabling a core fuel burn benefit, aligned with NASA goals, of 5%+ core and an overall 20% fuel burn and emissions reduction over the state of the art generation of products. To achieve this, GEA is focusing on a disruptive open rotor and compact core propulsion and power system architecture that combines various synergistic technologies which will deliver a step change in capability in order to meet industry commitments. Importantly, this includes an advanced compact core that is enabled with both hybrid electric (HE), advanced thermal management systems (ATMS), and advanced materials. The efficiency of the open rotor propulsor makes the compact core more critical than for a high bypass ratio ducted engine architecture.

GEA is the industry leader in core technology, which includes its combustor technologies. To realize these overall engine goals described above, a step-change improvement is needed within the combustor.

2. Technology Background

The combustion development program is starting with aerodynamic features based on a recent state of the art narrow body commercial design combined with learnings from a legacy combustor certification program. However, the cycle conditions, scale, emissions, and life requirements of the next generation motivate multiple new features/technologies beyond the current state of the art. Relative to the HyTEC – Combustor Technology project, the compact low emissions rich-burn combustor will incorporate CMC liners and a CMC dome to reduce weight of a narrow body sized engine and enable improved air utilization for mixing and NO_X reduction while maintaining a high level of durability.

To mature this technology, three main areas of focus will be developed. First, the new architecture requires feature testing to evaluate multiple approaches for attaching a metallic swirler to a CMC dome. While the aerodynamic performance of the chosen attachment method is critical, the long-term durability is equally important. To validate the potential durability, three different approaches were chosen for testing: 1) A design that relies on pressure to load the swirler against the dome, 2) A design that utilizes a threaded joint with a spacer to overcome the thermal growth mismatch, and 3) A design that utilizes a threaded joint while using elastic strain to overcome the thermal growth mismatch.

To further understand the durability of this swirler attachment, a deeper understanding of nickel diffusion into CMC is needed. This is the second area of focus and will be accomplished by breaking down the phenomenon into two parts: 1) the rate at which nickel diffuses into CMC and 2) the impact this diffusion has on material properties. This will be achieved in two ways. First, nickel diffusion testing will be completed to determine the rate at which nickel diffuses as a function of material selection, time, and temperature. This data will then be used to develop a nickel diffusion model. Secondly, mechanical behavior testing will be completed with CMC bars that have significant nickel diffusion to understand how the material capability degrades.

Beyond the maturation related to the mechanical attachments of metallic components, the significant use of CMC relies heavily on the capability of the EBC coating to protect the CMC. Therefore, the third focus area is the EBC capability relative to each of its typical failure mechanisms. Several EBC coating architectures were tested to demonstrate durability. This testing included coupon testing related to multiple failure mechanisms for EBC at various engine conditions and engine-simulative rig testing. The overall best coating for the predicted combustor environment reached TRL 5.

Maturation in these three areas provides the groundwork to a successful combustor that will be compact, meet performance and emission metrics, and continue to hold the high level of durability typical of General Electric's single aisle engines.

3. Design / Test Program

3.1 Swirler Attachment

3.1.1 Design Concepts

Several designs were conceived through benchmarking previous experience with metal to CMC interfaces, combustor components attachment methods, and novel ideas. For the HyTEC project, concept selection criteria were identified and used to rank/compare the designs. Three ranked concepts were down selected and designated G01 thru G03. These three concepts were evaluated as most likely to succeed as well as providing a benchmark to evaluate their success to previous efforts.

The G01 design relies on the pressure drop that occurs across the domeplate to load the swirler and flare assembly against the dome. Retention tabs mounted onto the metallic structure of the combustor prevent the rotation of the swirler assembly due the aerodynamic torque from the reaction of swirling the air, as well as retaining the assembly axially when the combustor is not in operation and the pressure delta across the dome is not present. The use of dome pressure drop to load the air swirler has been in use in legacy designs for lean burning combustors which allow for the mixer to float relative to the dome while remaining seated, this approach is novel for a rich burn application being demonstrated in this test.

The simplicity of the design provides several benefits which include part count reduction, ease of manufacture through simpler parts, ease of assembly, and resilience to wear at the metal to CMC interface.

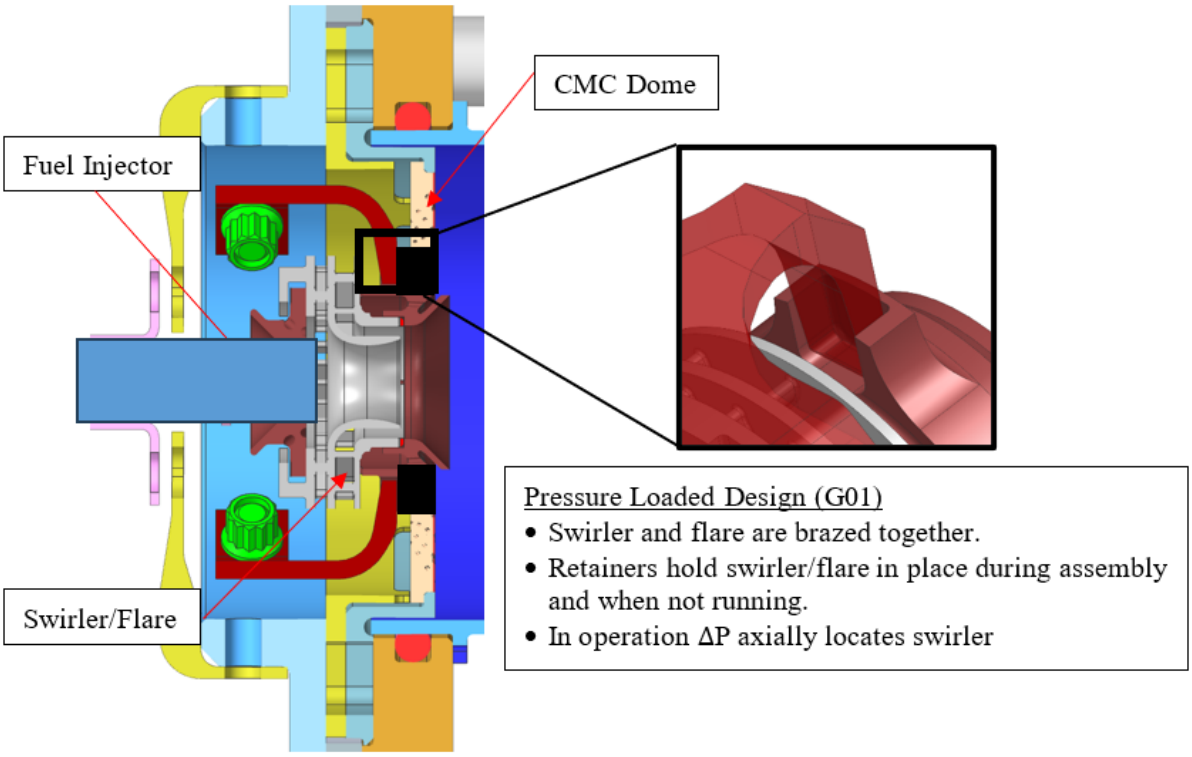

Figure 1: Cross-Section Outline of G01 Design

The G02 design utilizes a threaded joint that clamps onto the CMC domeplate. The bolted joint is designed such that the resulting clamping load is sufficient to retain the swirler and overcome its rotation at all operating conditions. A feature of the design is the spacer, which besides facilitating the bolted joint meet its requirements, it serves as an assembly aid. During assembly, castellation features on the flare engage with the spacer such that retaining the spacer will also prevent the flare from spinning when torque is applied to the swirler.

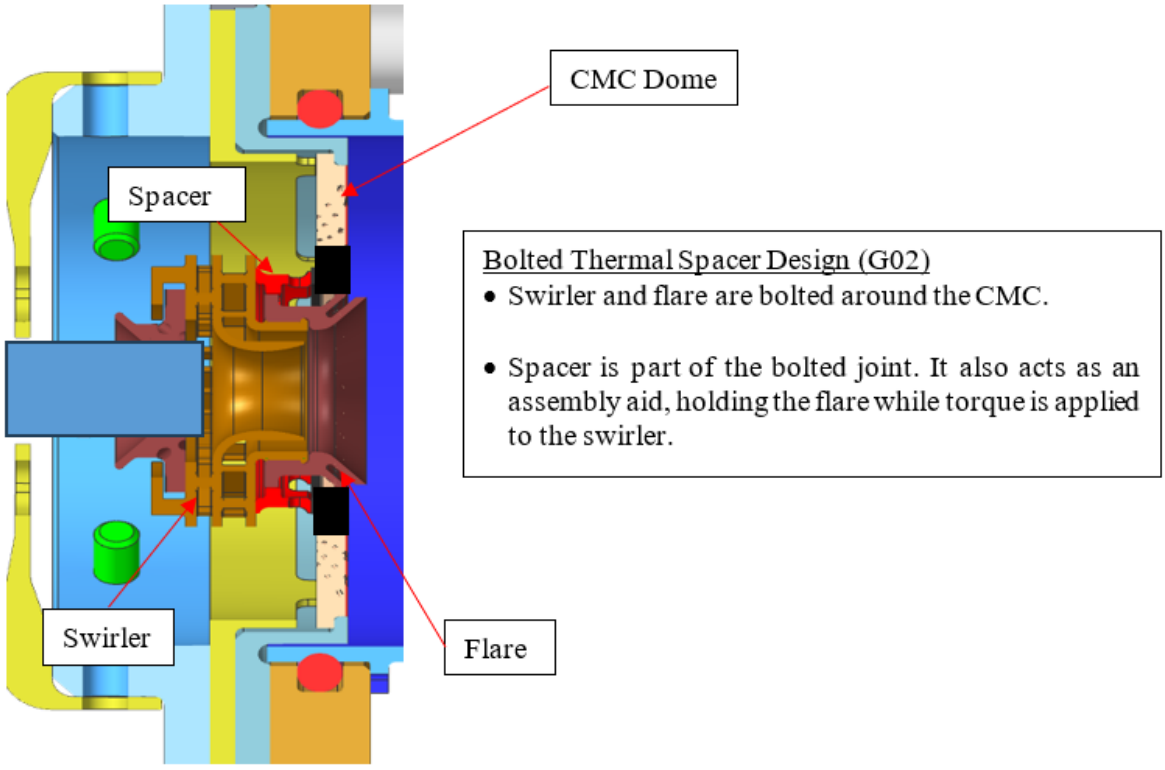

Figure 2: Cross-Section Outline of G02 Design

The G03 design also utilizes a threaded joint, however the preservation of the clamp at hot condition is achieved through the use of elastic strain in the Bolt/Nut. Deformation of the bolt acts as a spring, in which the thin flat portion bends (without yielding) at cold temperature. During operation the deformed portion of the bolt flattens out using the stored strain to preserve clamp.

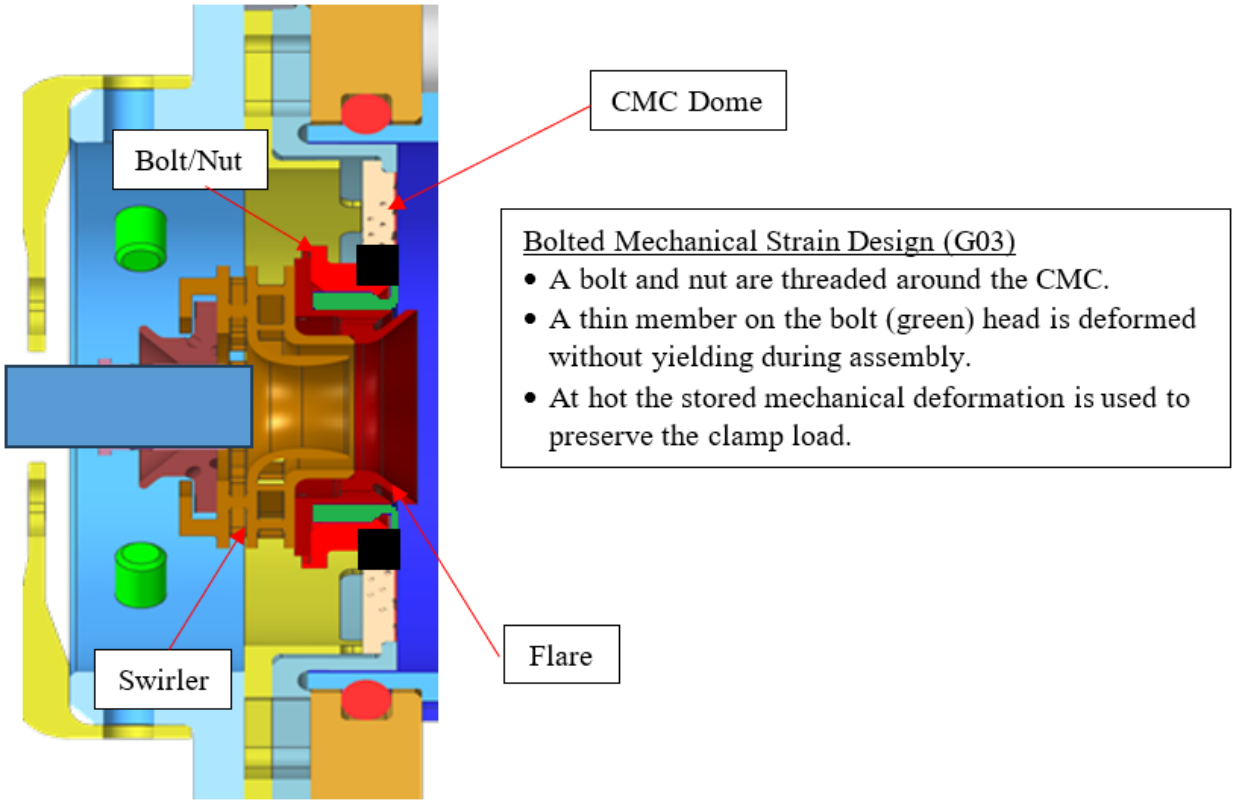

Figure 3: Cross-Section Outline of G03 Design

All three configurations were built around the use of the same, current state of the art, aerodynamic design of a rich burn combustor. This allows the team to use a proven combustor aero design that is understood to ensure that the testing of the metal to CMC attachments is not confounded with those of new swirler/flare/fuel nozzle development effort. This provides a strong benchmark to isolate any changes in performance. If differences are found, the switch from a double wall metallic dome to a single wall CMC dome is a strong candidate as the primary cause.

Along with the combustor performance, the combustor dynamic conditions created by the chosen combustor design have been mapped, well characterized, and demonstrated to match engine experience. Therefore, the single cup dynamics rig used for the HyTEC project will be subject to a dynamic environment that mimics those that would occur during engine operation.

Lastly the use of an existing combustor design lends itself to readily available components such as swirler castings and fuel nozzles which are otherwise long lead items to procure for a new development design.

3.1.2 Test Rig Overview and CMC Incorporation

Testing of the CMC assemblies is done using two single cup combustor rigs. The Tunable Combustor Acoustics (TCA) rig operates at lower power conditions where combustor dynamics are typically seen. A movable piston on the aft portion of the rig allows for changing the downstream volume to target different combustor dynamics frequencies. The frequency that can be targeted would correspond to the speed of sound divided by two times the length from the dome to the piston head. A layout of the TCA rig is shown in Figure 4.

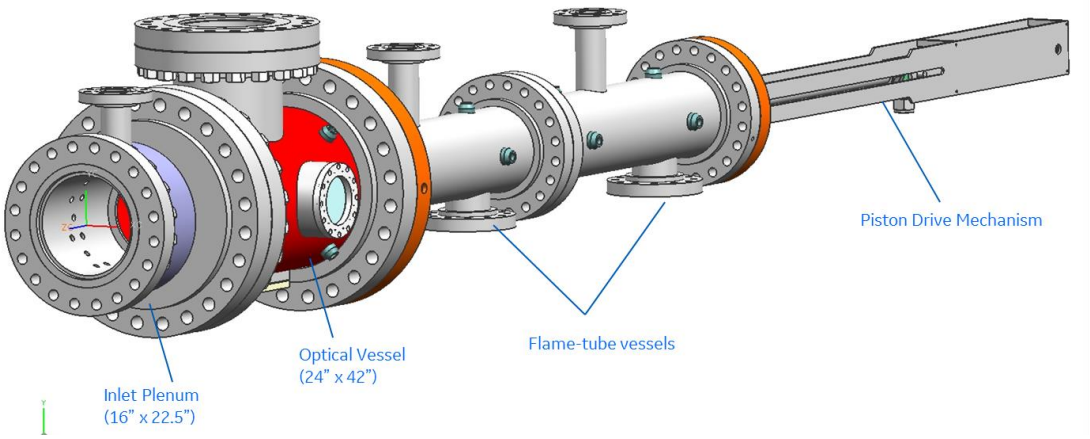

Figure 4: TCA Rig Overview

The High Temperature and Pressure (HTP) rig is designed to test the ferrule/swirler/flare/nozzle combinations at and even beyond full engine conditions. For the HyTEC project, the HTP rig allowed testing the proposed designs at several engine cycle conditions as well as a dwell at full engine power to gain insights of the long term durability.

For the HyTEC project, a set of retention plates were designed in order to replace the existing TCA/HTP rig metallic domes with CMC dome assemblies. The retention plates retain the circular CMC domes by capturing the outer diameter of the domeplate with only a small amount of clearance. During testing the pressure differential from the dome loads it against the plate. Tabs on the metallic retention plates line up with notches on the CMC to provide circumferential clocking as well as anti-rotation of the domeplate from the aerodynamic torque imposed by the swirler.

Figure 5 shows a cross-section of the two retention plates (shown in yellow and blue) with a CMC domeplate in the middle. The longer tabs on the forward retention plate (shown in yellow) provide the anti-rotation, while the shorter ones hold a small gap with the CMC to prevent it from falling off while there is no pressure differential.

The plates at their outer diameter have the same geometry as the metallic domeplate they replace, allowing them to be swapped in with no changes required to the rest of the rig.

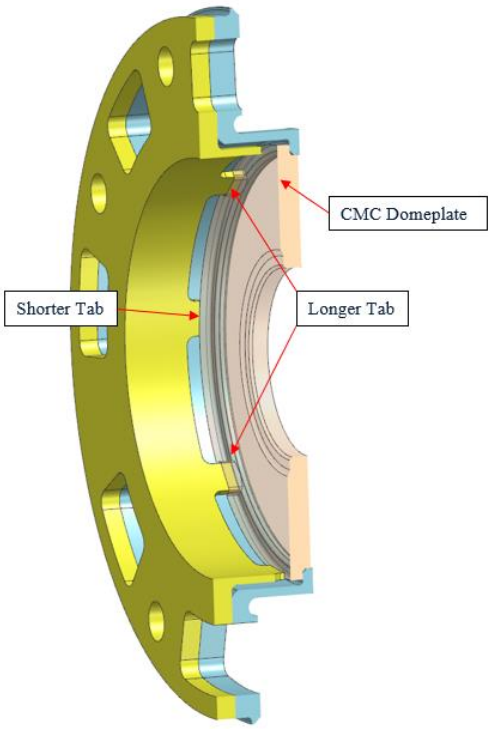

Figure 5: Cross-Section View of TCA/HTP CMC Dome Retention Plates

When mounted in the single cups rigs, the boundary conditions of the swirler and flare mimic those of the engine. The fuel nozzle is either mounted by separate brackets to the rig in the case of the TCA or as a case mounted nozzle in the HTP. In conjunction with the floating ferrule used to seal the fuel nozzle with the swirler, the nozzle does not provide retention of the swirler or flare, like the arrangement in the engine.

A wear coating is used on the anti-rotation tabs of the G01 configuration. The tabs themselves are made of a cobalt alloy with good wear capabilities. The interfacing flare hardware is made of a single crystal nickel alloy, with poorer wear capabilities. Wear coating is sintered to the flare during the braze operation that brazes the flare and swirler together. The coating is cobalt based, providing a Cobalt-to-Cobalt interface reducing wear on the flare.

3.1.3 Assembly Stack-ups

To evaluate the hardware capability and operating condition of the test article, the maximum test cell conditions were used.

For evaluation, the HTP maximum rig conditions are used as they result in the maximum material temperatures of the parts and therefore present the limiting condition for the test article and fuel nozzle alignment. Arithmetic stack-ups of the components' dimensions with allowable manufacturing tolerances at assembly and operation are calculated to ensure assembly is possible and operation of the test article at test conditions is done to design intent.

For the HTP rig, the fuel nozzle is mounted on the outside of the pressure vessel unlike the TCA fuel nozzle which is mounted alongside the rest of the rig. This arrangement on the HTP results in a shift of the nozzle tip location between the cold assembly condition to that during testing at hot conditions. A cold to hot

evaluation of the radial and axial shift of the nozzle, rig, and test article was completed to determine the shift of the fuel nozzle tip relative to the swirler in order to properly locate the nozzle during assembly.

A laser system inserted at the aft of the rig is used to verify the alignment between the nozzle and swirler ferrule during assembly. The mounting plate, referred to as a wedge, that the fuel nozzle sits on has oversized bolt holes to allow adjustment of the plate on the pressure vessel to achieve the desired alignment prior to tightening the bolts.

3.1.4 Test Article Analytical Capability

Evaluation of the test article capability was done both at the cold and hot conditions to evaluate the assembly loads put on the parts as well as the material capability at hot condition. A bolted joints analysis was done to ensure bolted joint met design criteria during testing.

For cold assembly, the G02 design has the limiting condition as the torque is applied to the cast swirler whose material is less capable than the material used on the torquing feature in the G03 design. Moreover, the torque is transmitted through the swirler vanes which have small radii. Figure 6 shows the boundary conditions used to evaluate the assembly stresses on the G02 components.

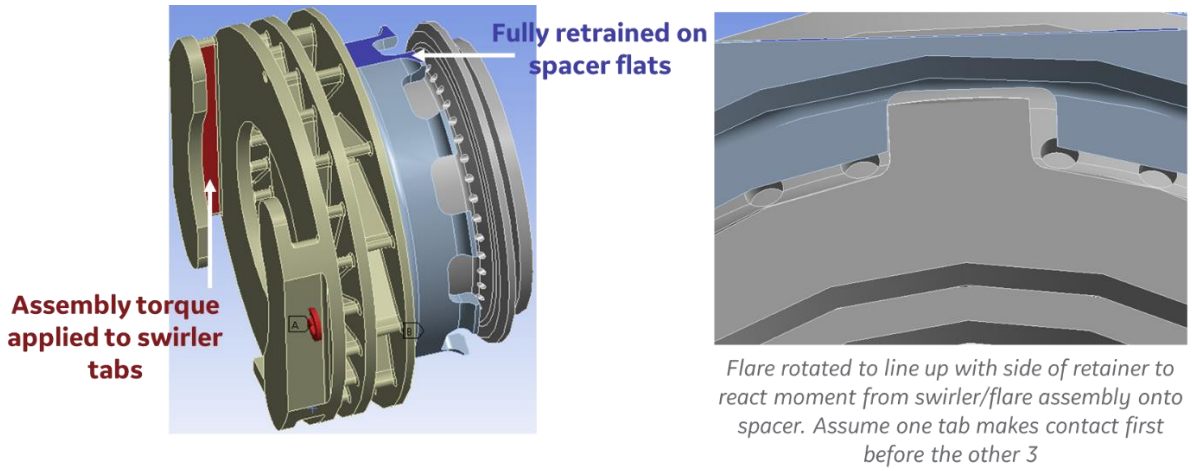

Figure 6: G02 Assembly Stresses Model Boundary Conditions

Peak stresses at assembly occur on the small fillets on the swirler, flare and spacer. For the spacer the tabs are only used as an assembly aid and once put together there is no load through them. The flare and swirler, which serve as aerodynamic features, do not see stresses above the yield stress of the material. There is no plastic deformation of these parts that would affect the aerodynamic features or otherwise affect their aerodynamic performance.

For the G02 design, an evaluation was made to calculate the clamp load loss in the joint at full HTP conditions. At the HTP design point the clamp load drops by approximately 30% to 40% from the cold assembly clamp load.

The aerodynamic torque of the swirler combined with its vibrational load impart a transverse load of <5% the predicted clamp load at operation.

Accounting for the friction coefficient between the CMC and the metallic components, the minimum clamp load at temperature required is approximately 10% of that calculated in operation, giving the G02 design a >10x margin to the required clamp load to overcome the transverse loads from the swirler.

For the G03 design, the deflection of the bolt head acts as a spring which at hot condition uses the stored energy to preserve the clamp load on the joint. The calculated strain calculation is done to determine the amount of cold deflection the thin member of the G03 design must undergo to retain the design intended clamp in operation.

Figure 7 below shows the material stress relative to its yield stress for the required stretching. The through thickness stress is within the 0.2% yield strength for the material at the design temperature. The ultimate strength is above the peak stress at the radii. The thin wall member will elastically deform (with only yielding at the surface of the material at the radius).

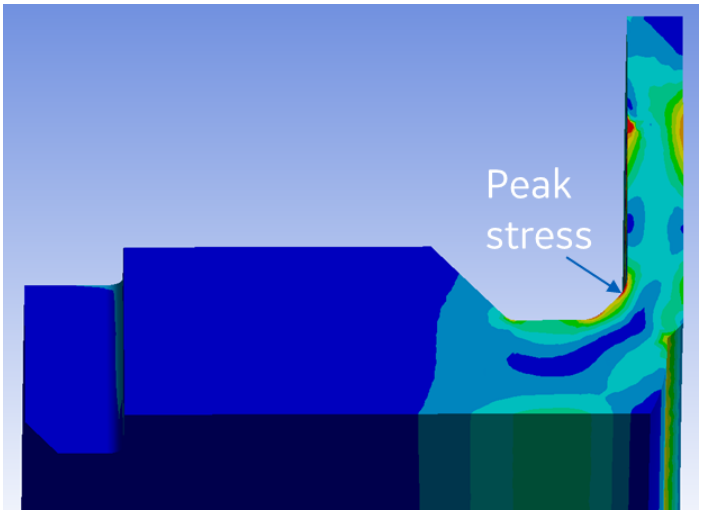

Figure 7: G03 Assembly Stresses

The thermal capability of the CMC domeplates was also evaluated to help in the calculations done thus far and to evaluate the material's durability during testing. The cooling pattern on all three configurations was designed to preserve the same flow as used on the baseline combustor rig. As stated in section 3.1.2 this is done to mimic the baseline aero performance for which the combustor dynamic response is well characterized.

Computational fluid dynamics (CFD) is utilized to predict the thermal condition of the CMC domes. The solution allows mapping the surface gas temperature as well as the heat transfer coefficient onto the part which not only gives the peak material temperatures but allows for evaluation of the thermal strain on the CMC, CMC recession, and appropriate material curve to use in evaluating cyclic capability.

Figure 8 shows the hot gas temperature mapped onto the surface of the P01 dome with 1D heat transfer calculated temperatures at various points in the dome, including the predicted peak temperature. All temperatures are predicted to be within the material design conditions for the CMC and EBC materials used on the dome.

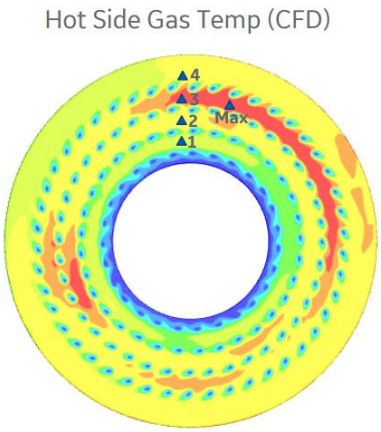

Figure 8: Predicted Gas Temperature from CFD and Material Temperatures

Using the hot side as boundary conditions, a conduction solution is used in a finite element model (FEM) to calculate the through thickness thermal gradient and the resulting thermal strain in the part. Combined with the pressure load from the combustor dome pressure drop and the plug load from the swirler, this provides the strain/stress on the CMC part. Evaluated to the material fatigue curves, all three dome configurations are calculated to have greater than 100 cycles of capability for use in testing.

A thermal solution was also completed with the EBC removed. This solution is used to evaluate the time for recession through the CMC thickness at the peak temperature location assuming coating loss during testing. Recession analysis calculates >100 hours needed to go through the thickness of the part in case of coating spall. This is more than the 100 hours required to ensure test completion.

Modal evaluation of the CMC domes is summarized in Figure 9. The calculated modes of the three different designs are in the 80kHz range. This is well above the maximum frequency that is explorable in the TCA rig. As such, there are no modes to be excited during testing to cause high cycle fatigue failure during testing.

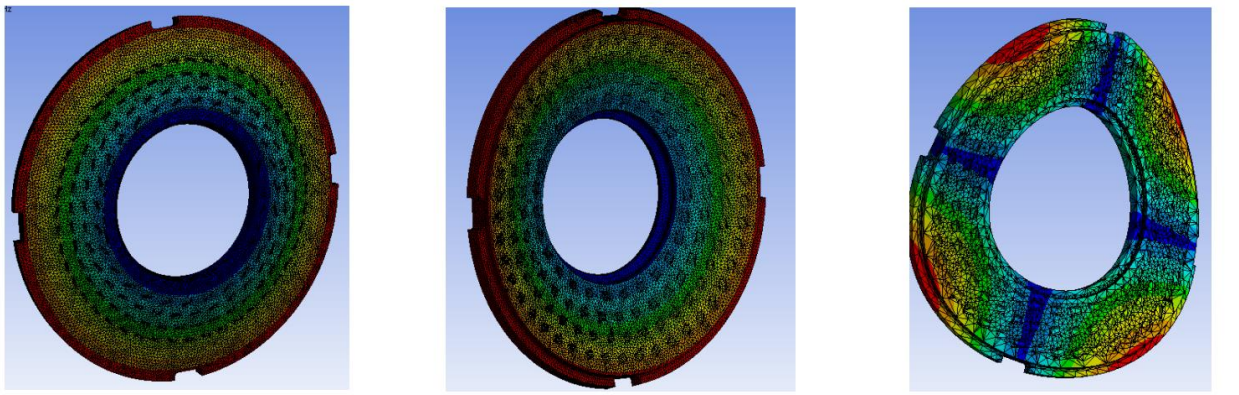

Figure 9: CMC Deflector Modes with Swirler Point Mass at Eyelet

3.2 Nickel Diffusion

The CMC dome in the G01-G03 design is connected to the deflector made from a single crystal Nickel alloy. With the temperature of the hardware being above 1,300°F (704°C), there is a concern about the durability of the hardware due to possible interaction between these two materials. SiC CMC contacting Ni containing alloys have shown a bimodal diffusion reaction in the laboratory. Ni infiltrates into the CMC creating nickel silicides within the SiC matrix, while the Si diffuses into the alloy, also creating nickel silicides, but also drives the other elements to precipitate out and/or interact with each other. This process starts to be observed at hardware life timescales (See *Table 12*) around 1,300°F (704°C). There is an increase in the diffusion rate at T>1,772°F (967°C); the lowest eutectic temperature point is seen in the Si-Ni phase diagram (Figure 10). To assess the risk to the durability of the hardware from this process first requires understanding the extent of the diffusion that the part will experience. Secondly, the mechanical properties of this new material that has been created at the interface is needed for hardware assessment.

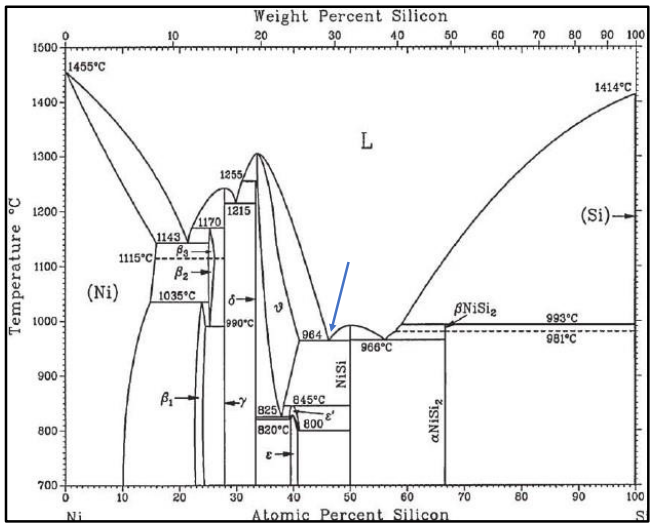

Figure 10: Ni-Si Phase diagram (T.B. Massalski 1990)

3.2.1 Diffusion modeling

To establish a predictive model for the diffusion into the CMC, a series of isostatic diffusion tests were performed across the variable space of time, temperature, and Ni concentration in the alloy, geometrically represented in Figure 11. As each of these variables increases, the rate of diffusion also increases. Three different alloys were selected based on a ~15% Ni wt.% difference between them; Hastelloy X, René N5, and Inconel 600 with 48.1 wt.%, 63.45 wt.%, and 76.83 wt.%, respectively. The remainder of the alloy elemental composition is listed in Table 1. The three temperatures of 1,600, 1,700, and 1,800°F were selected to establish measurable diffusion within a short time and reduce test rig time needed. To get sufficient diffusion to measure, the tests at 1,700 and 1,600°F were run for 50, 100, 200 hours. For the 1,800°F test however, since the diffusion rate is much faster than the other two temperatures, the time had to be decreased to 25, 50, and 75 hours due to the finite thickness of the CMC coupon. An 1,800°F isostatic diffusion test for 200 hours would result in diffusion through the full thickness of the CMC, rendering depth measurements impossible. The test conditions are listed in Table 2.

Table 1: Weight percentage of the elemental composition of the alloys utilized in the isostatic diffusion tests

Ni Based Alloy			
wt%	Hastelloy X	René N5	IN600
Ni	48.10	63.45	76.83
Co	0.7	7.4	0.069
Fe	18.7	0.1	8.79
Cr	21.9	7.1	15.92
Al	0.18	6.20	0.14
Ti	0.02	0.01	0.19
Ta		6.44	
Nb		0.01	0.083
V		<0.01	
W	0.55	4.91	
Re		2.89	
Mo	8.49	1.42	
C	0.07	0.06	0.063
Hf		0.15	
B	0.002	<0.0001	
Zr		0.02	
Y		<0.0001	
Mn	0.61	<0.01	0.42
Cu	<0.0001	<0.01	0.08
Zn		0.00	
Mg		0.0	
Si	0.28	0.03	0.16
S	0.000	0.000	0.001
P	0.008	0.002	
La		<0.0001	
Sn		0.00	
N2		0.0003	
Tot	100.00	100.00	100
Density	0.297	0.312	0.307

Table 2: Parameters selected for the isostatic diffusion tests

Diffusion test plan				
three (3) alloys with differing Nickel content	three (3) test temperatures	test duration for 1800 °F	Test duration for 1700 and 1600 °F	two (2) repeats
HAST X René N5- Inconel 600	1800 °F 1600 °F 1500 °F	75 h 50 h 25 h	200 h 100 h 50 h	2
				54 Tests

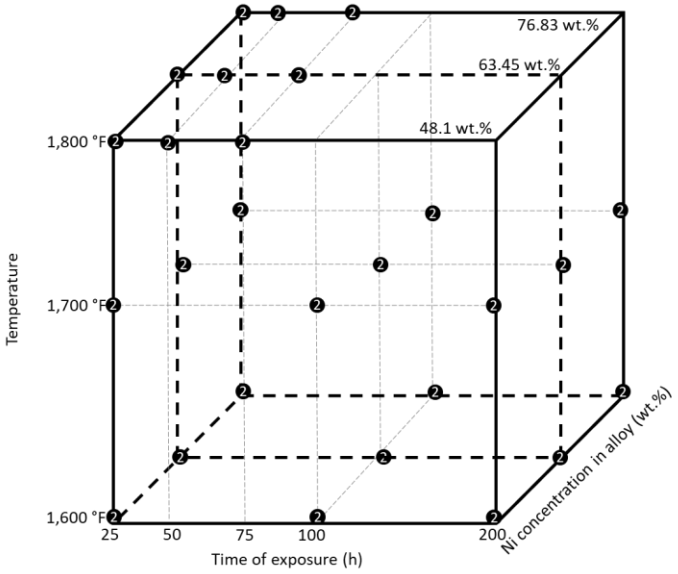

Figure 11: Geometric representation of the diffusion test parameter space

Isostatic diffusion tests are performed by utilizing a 1" metal button and a 0.250 in^3 SiC/SiC CMC cube machined from a 32 ply $(0/90)_s$ panel. A schematic of the test set-up can be seen in Figure 12. The CMC specimen is oriented such that the 0/90 plies are parallel to the contacting test surface. A pressure of 1.5 ksi is required across the contact interface to ensure intimate contact between the samples and promote consistent diffusion results.

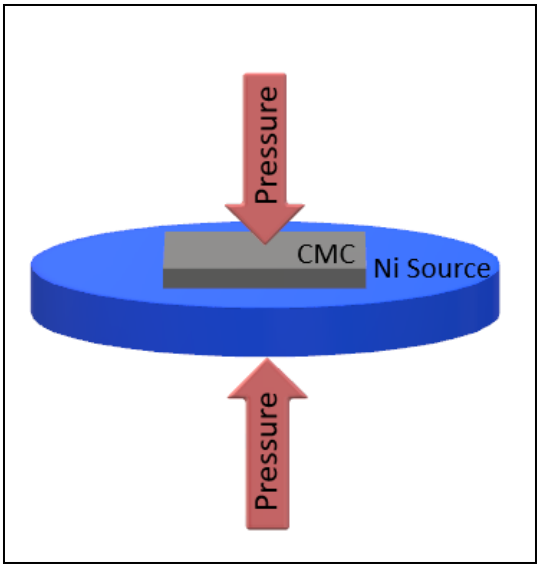

Figure 12: Schematic of the test coupons during isostatic diffusion tests

The diffusion process made use of three different rigs within the Materials Behavior organization within GE Aerospace: 1036.20, 1004.10, and 1050.05. Each rig was outfitted with a 3.5" igniter element furnace. To begin, the CMC sample contact surface area was measured to determine required load to achieve the 1.5 ksi cross sectional pressure. Procedurally, the sample stack was installed in the machine with Teflon tape between the CMC piece and the metallic test sample. The sample stack was placed between two WG300 non-stick pucks to isolate the CMC test block from the metallic fixturing on the rig. A small load was applied, making an impression into the Teflon tape. The tape was removed and inspected for consistent contact across the sample surface. The metallic sample was instrumented with a thermocouple and reinstalled at -20lbs to secure the metallic sample against the CMC sample. Heat was applied using an igniter furnace to the desired temperature. Once temperature set point was achieved, the coupons soaked for a minimum of 1 hour, to achieve thermal equilibrium, prior to applying the required pressure of 1.5 ksi to initiate the diffusion process. Following the soak period, load was applied at a constant rate and held for the test duration. At the end of the test, the load was automatically removed, and the furnace was shut down to eliminate further exposure.

Following diffusion, the samples were imaged using a macroscope. The macroscopy was done using a Keyence VHX-1000 Macroscope. The diffusion side of both the CMC and metal samples were imaged to characterize the surface material gain or loss. Following macroscopy, the samples were sectioned. First, both metal and CMC samples were encased in Huntsman Araldite two-part epoxy. This encasing step was completed to protect the diffusion zone from damage. The metal samples were sectioned using an abrasive saw, following Figure 13 below. The metal samples were cut across the diagonal of the diffused zone to maximize the cross-sectional surface area. The CMC samples were also sectioned at a diagonal, however utilizing a diamond saw.

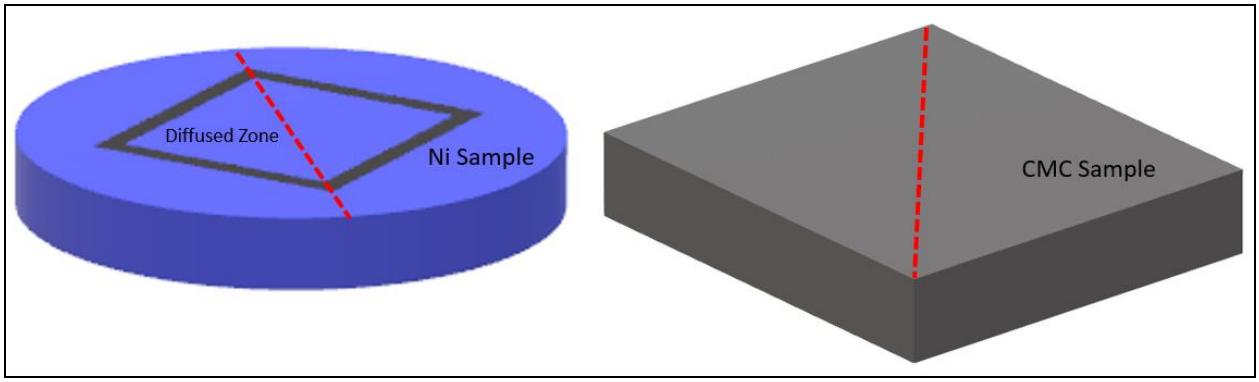

Figure 13: Sectioning Diagram for Metal and CMC Samples

Polishing of the sectioned material was done to improve visualization of the diffusion zone. Half of each sample was mounted and polished and the other half of each sample was retained as is. Each of the cut samples were mounted within Huntsman Araldite. Vacuum was pulled on each sample in order to help fully infiltrate the samples. After the epoxy curing was complete, the grinding process took place.

The metal samples were placed in a grinding machine, in which the platen rotates at 300 RPM counterclockwise, while the specimen mover head rotates at 150 RPM counterclockwise. The machine was set to apply 150N of pressure on the samples. The diamond grinding disks used were acquired from Allied High Tech. Each grinding step was 2 min long with increasing grit sizes of 220, 320, and 600. A constant stream of water was used during the grinding process, the discs were dressed using an Aluminum Oxide stone and the samples were rinsed with water between each cycle iteration. After grinding, the metal samples were polished via Struers-MD Mol cloth with Allied 3 µm Polycrystalline Diamond Suspension for 190 s. A final polish for 70 s on an Struers MD-Chem cloth with Meller Optics Inc Colloidal Silica was performed and the samples were cleaned with dish soap, rinsed, and dried.

The CMC samples initial grinding is performed with the same method as the metal with the exception that the final 600 grit grind is not performed. However, a series of polishing suspensions were used to get the final surface finish.

Following mounting and polishing, the samples were characterized using two different methods. The metallic sample diffusion depth was measured using an optical microscope. A representative example of a diffusion measurement of a metal sample can be seen in Figure 14. The diffusion zone was typically observed to be a darker species. For each sample, the measurement was taken at the point of deepest diffusion into the sample that was present across the mount.

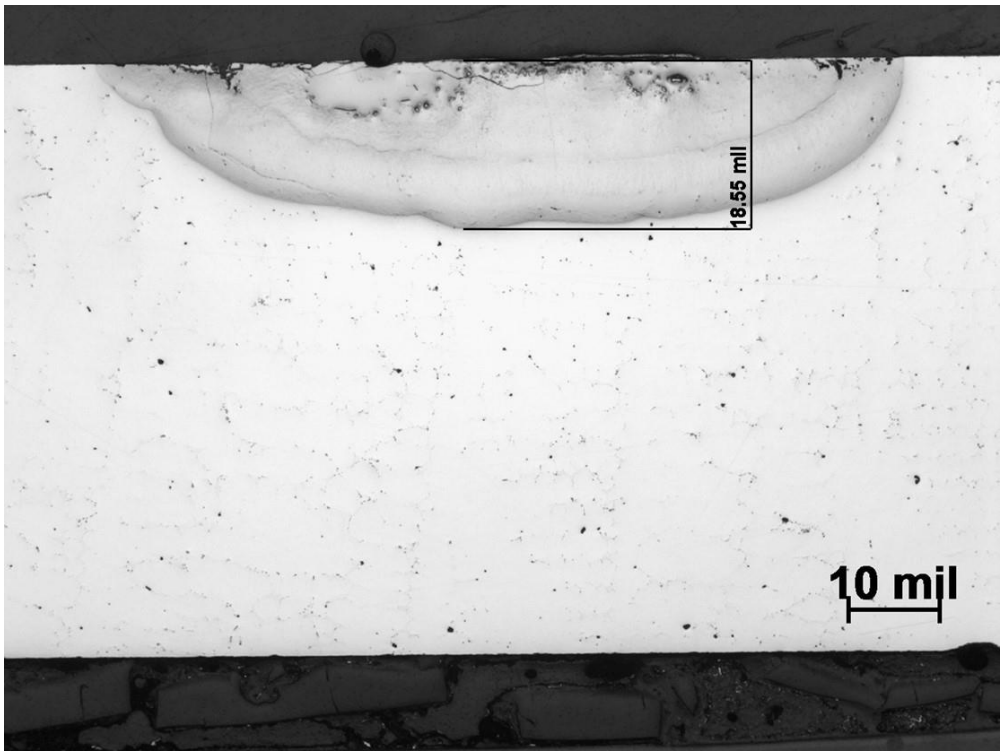

Figure 14: Representative Diffusion Measurement of the metal button after isostatic diffusion testing

The CMC samples were characterized using scanning electron microscopy (SEM) and energy dispersive x-ray (EDX) because the diffused zone is not visible with optical microscopy. A representative measurement can be seen in Figure 15, where the Ni diffusion is the lighter colored area. In the same way as the metal samples, the deepest diffusion across the sample was measured and recorded. After testing, cracks within the coupon are seen due to adhesion to the metal coupon due to creep occasionally occurring.

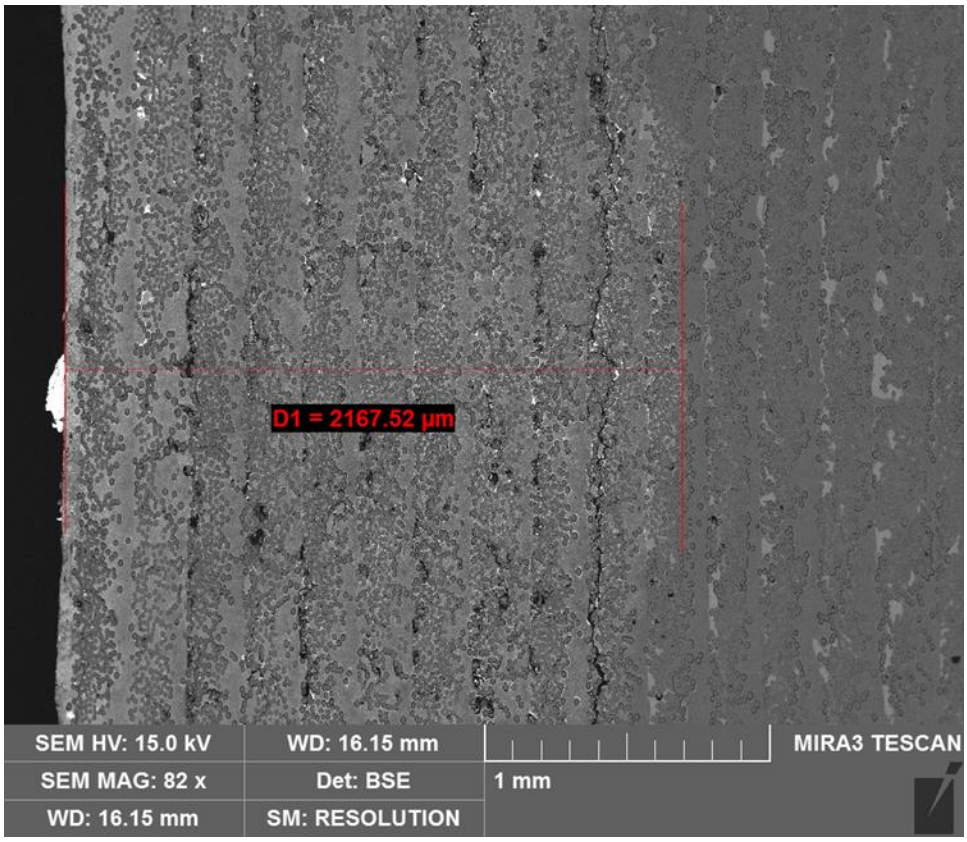

Figure 15: Representative SEM Diffusion Measurement of the CMC after isostatic diffusion testing

It can be noted that after the samples were completed and characterized, some of the samples indicated lower diffusion than expected. These samples were repolished per above specifications and remeasured. In the case of the Hastelloy X Ni source, the samples did not exhibit the predicted trend, so the retained other half of each sample was mounted and polished for remeasurements. After all the additional characterization, the deepest measurement for each sample was reported. The raw diffusion data provided to NASA for the modeling effort is in Table 19 of the Appendix.

After the maximum diffusion depth into the CMC was measured for all tests, some tests were selected for further characterization. For these coupons, the nickel wt% was measured at different depths into the diffusion zone. This was performed to understand the nickel concentration as a function of depth. Microprobe was used for some tests, however the spot size on that system produced scattered measurements that were likely due to localized diffusion not being homogenous. Using EDS, a large spot size is possible which measures the average Ni concentration within the area chosen within the matrix. Measurement points are only taken within the matrix zone between fiber-plies as the Ni does not interact with the SiC fibers at these temperatures and will decrease the average measured Ni concentration.

3.2.2 Mechanical Properties of Diffusion Product

Table 3: Mechanical property tests and temperatures utilized on Ni diffused CMC test bars

Mechanical testing
Tensile tests: 16 across multiple temperatures (70, 1,500, 2,200, and 2,400°F)
Interlaminar shear: 8 tests at 70°F
HCF test: 8 tests at 1,500°F

Mechanical properties of the diffusion product are needed to assess the hardware after diffusion has occurred. For the combustor dome and swirler, the tensile, interlaminar shear, and high cycle fatigue (HCF) properties were used for the original design assessment, therefore these same properties for Ni diffused CMC are tested and measured. The new curves of CMC with Ni diffusion are utilized in the durability assessment modeling. Table 3 outlines the temperatures at which the different tests were run.

Before mechanical property testing could occur, manufacturing development work was needed to produce a highly Ni diffused CMC test bar. For the Nickel source, Nickel 200/201 (99.5 wt.% Ni) was utilized to get consistent diffusion products in the CMC test bars. Trials were run with blanks of CMC strips from 8-ply panels. Each test bar utilized two Nickel 200/201 plates and each plate was only used once. Manufacturing trials were conducted to establish what time at temperature will produce a consistently diffused coupon. The manufacturing set-up has the CMC test coupon sandwiched between two pieces of Nickel 200/201 as seen in Figure 16.

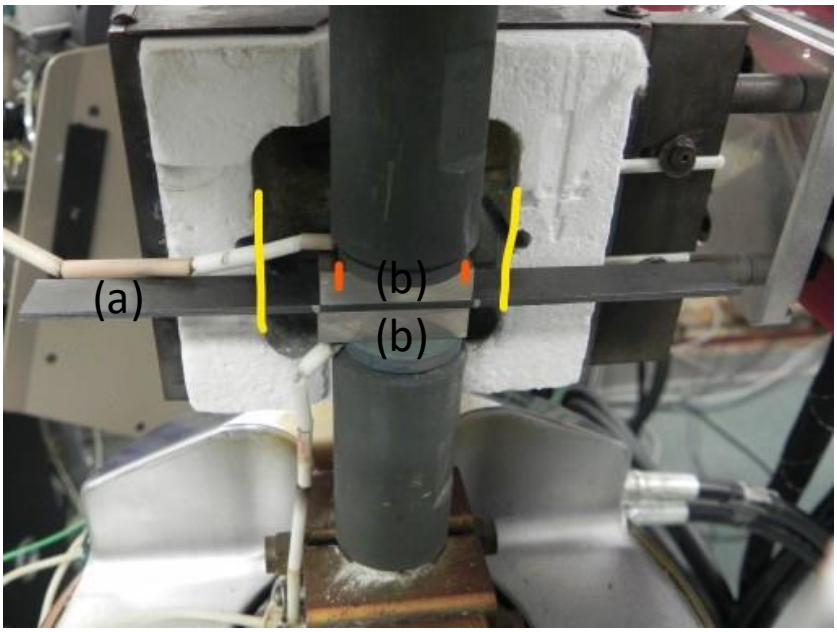

Figure 16: Image of CMC test bar manufacturing process
(a) CMC sandwiched between two
(b) Nickel 200/201 metal plates

To manufacture coupons at a reasonable rate, 1,800°F was selected as it is slightly above the temperature that the diffusion rate increases drastically. High temperatures were avoided during the trials to limit the Nickel 200 interaction with the physical surface of the CMC. Once diffusion initiates, creep, and adhesion of the metal to the CMC can occur with increasing temperature and/or increasing stress. Three stress values were tried, with 1.5 KSI causing adhesion of the Nickel 200 to the CMC, and 0.5 KSI not having enough intimate contact to have consistent diffusion across the interface. The utilization of 0.9 KSI avoided both issues.

Table 4: Mechanical test bar manufacturing development trial tests.

Test #	Temperature [F]	Stress [ksi]	Time [hr]
DTB-2022-01	1,800	1.5	12
DTB-2022-02	1,800	0.9	60
DTB-2022-03	1,800	1.5	120
DTB-2022-04	1,800	0.5	120
DTB-2022-05	1,800	0.9	120
DTB-2022-06	1,800	0.9	160

During the trials outlined in Table 4, processing time was constantly increased as each iteration did not hit full saturation of the test bar. Seen in Figure 17, after 120h at 1,800°F there is a diffusion gradient across the gauge section of the test bar with the middle having a Ni% of 10.7-12.6 wt.%. Review of the microprobe data generated during the diffusion modeling testing shown in Figure 18, shows that independent of time of test and alloy used during the test, most of the diffusion zone spans 5-14% Ni wt.%. Fielded hardware would also have this same gradient range and the nickel concentration in the middle of the test bar falls within this range. This consensus of the nickel concentration in isostatic tests and the test bars was sufficient to utilize 1,800°F for 120 hours for the manufacturing of the test bars.

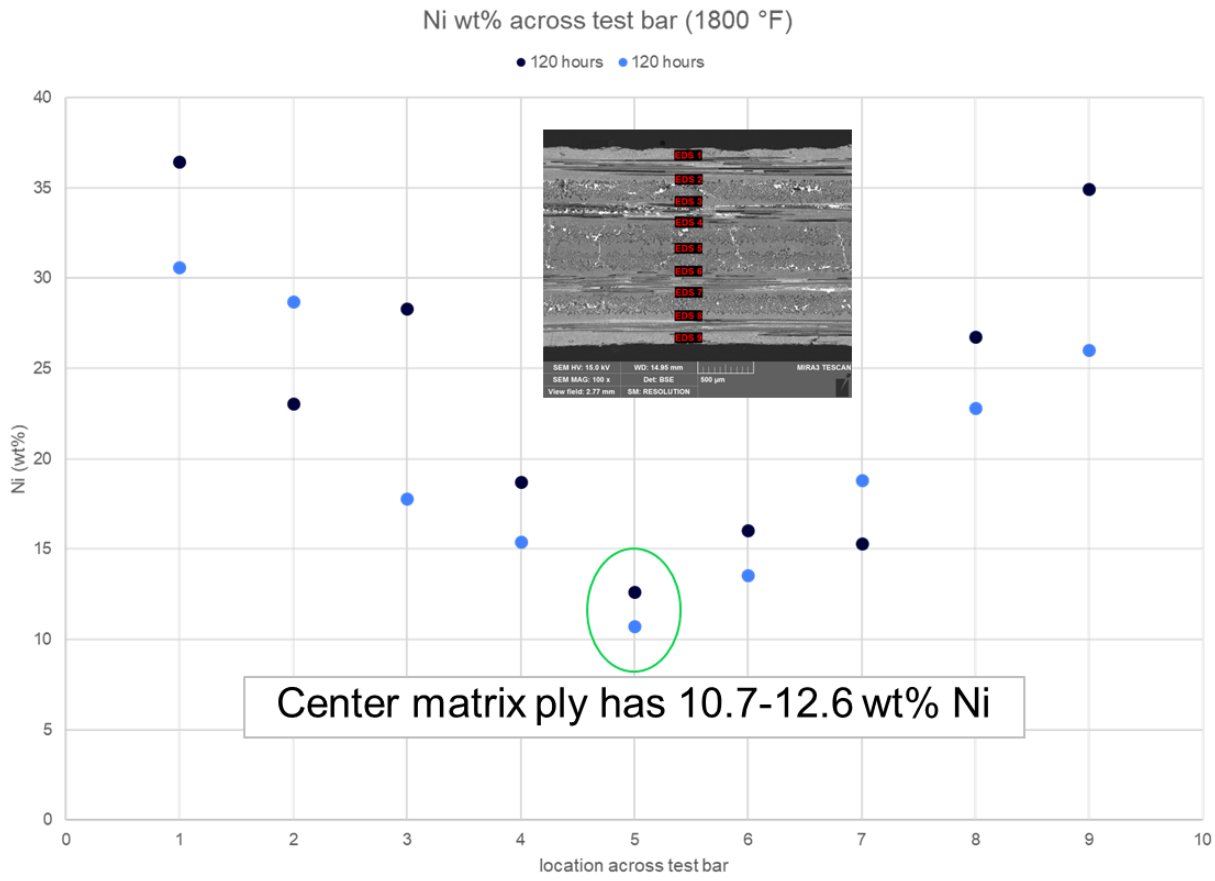

Figure 17: Nickel wt% across the gauge section of two independent tests (denoted by light blue and dark blue) after production trial at 1,800°F for 120 hrs (inset) locations through the CMC test bar where the Ni concentration was measured.

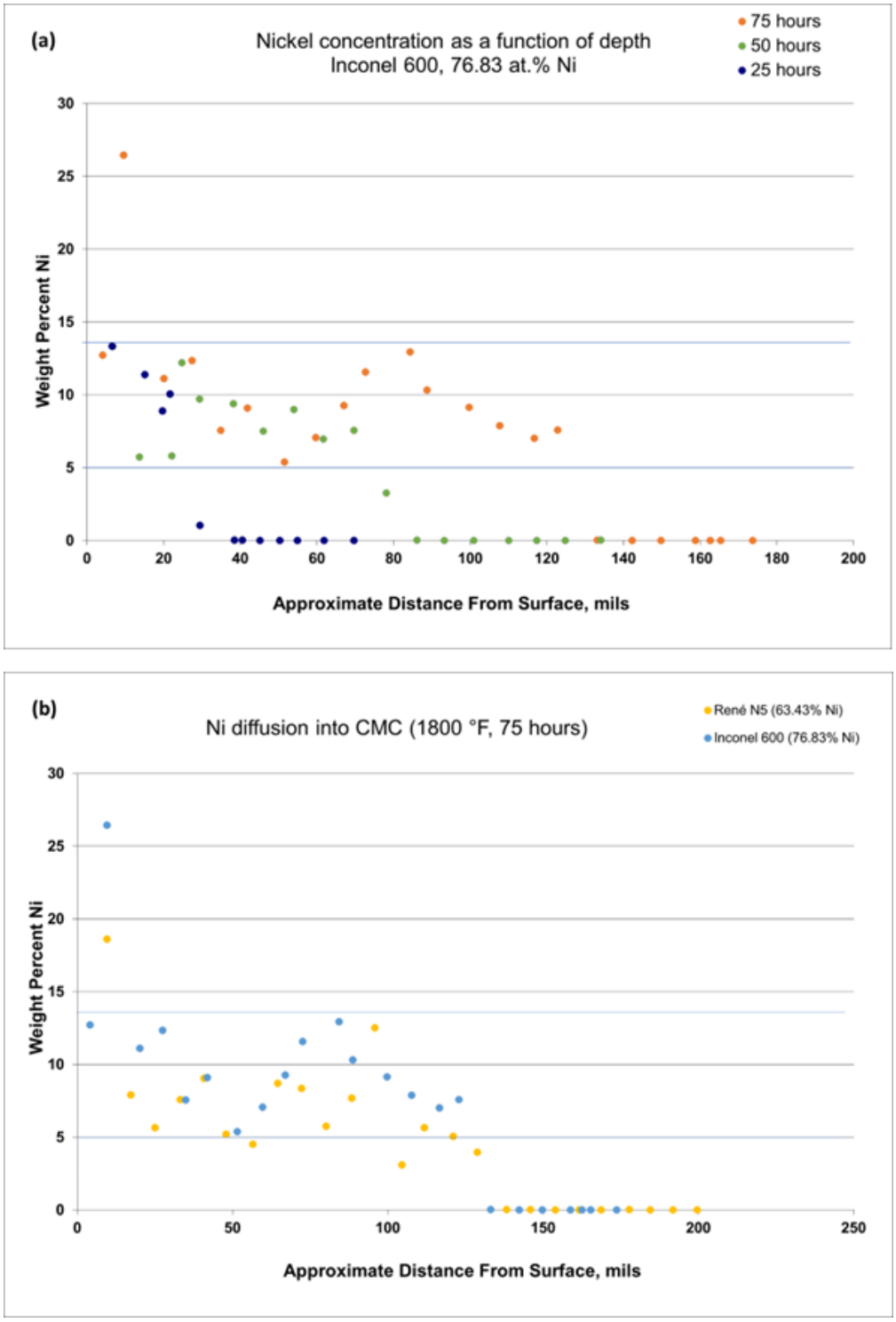

Figure 18: Microprobe data of nickel wt.% as a function of depth into the CMC at 1,800°F: (a) three different test durations and (b) René N5 (63.43 wt.% Ni) and Inconel 600 (76.83 wt.% Ni).

To increase the rate of coupon production, a stack method, as seen in Figure 19 was used. After manufacturing, both sides of the test bars were scanned by a Keyence VR-3200 and the loss of any material was documented.

Mechanical property tests were performed at Cincinnati Test Laboratory (1775 Carillon Blvd, Cincinnati, OH 45240). Tensile tests were performed to ASTM C1359 with four repeat tests at four temperatures.

The shear beam test set-up is seen in Figure 20. A 4-point asymmetrical shear test method was utilized for the shear test[3]. The high cycle fatigue was performed at 1,500°F at a frequency of 30 Hz and a min/max fatigue stress ratio of 0.05 (R=0.05) per ASTM C1360[4].

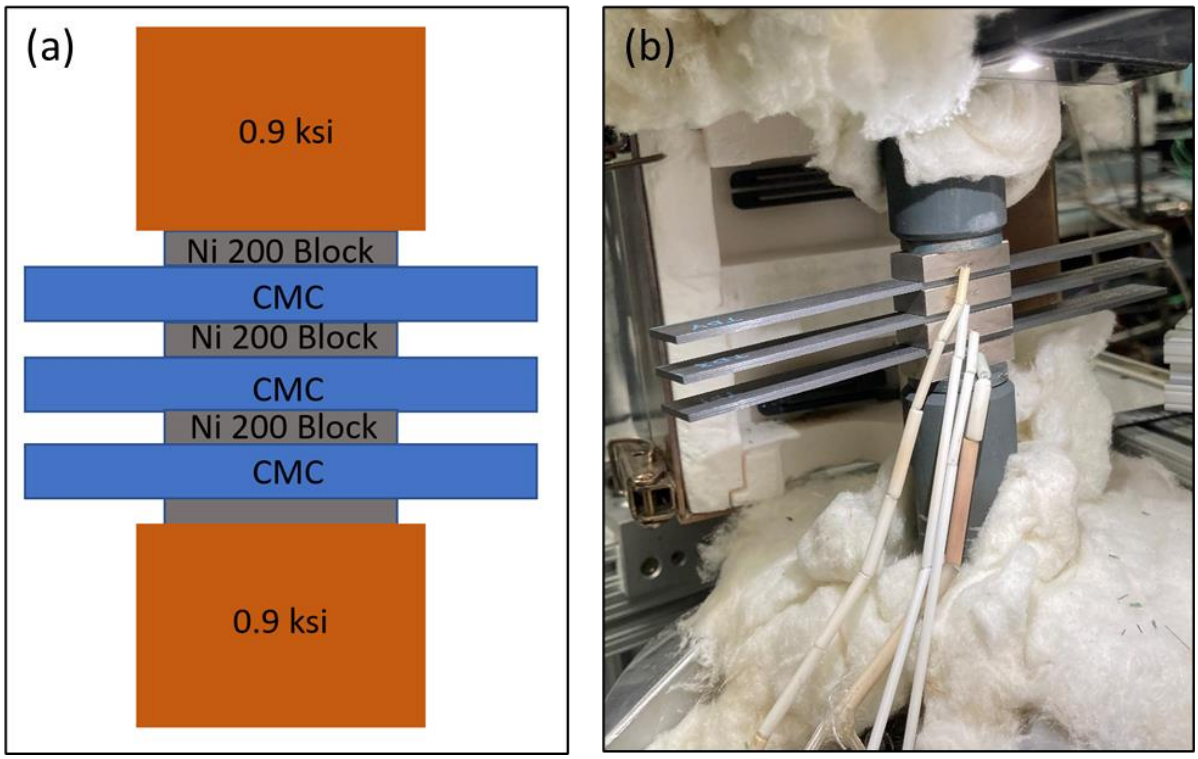

Figure 19: (a) schematic stack-up of nickel 200/201 and CMC for production of test bars and (b) image of set-up on the rig

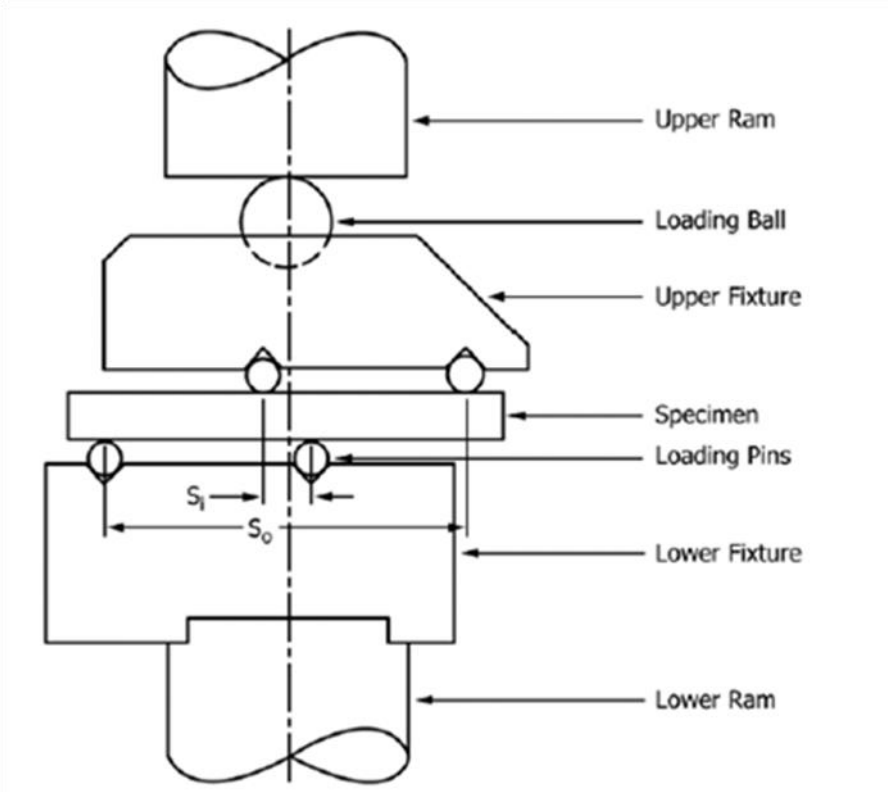

Figure 20: Schematic of the shear beam test setup

3.3 EBC Advancement

The work completed under HyTEC interrogates the durability of the integrated CMC/EBC system in liner-representative conditions by coupon and component/rig testing. EBC is constituted of individual layers such as bond coat, gas-tight layer(s) and a CMAS resistance layer, where these layers provide specific functionalities that influence the overall EBC durability. The silicon (Si) bond coat and the gas-tight layer(s) provide resistance to water-vapor oxidation and the top layer provides resistance to water vapor recession and CMAS attack. In service, various failure modes of these layers can lead to early EBC loss and limit the durability of the underlying CMC.

For the integrated combustion liner, GEA has selected three EBC architectures (Figure 21) applied by air plasma spray (APS). The gas-tight layer uses rare-earth disilicate ($ReSi_2O_7$, REDS) compositions such that a suitable CTE match is made with the bottom Si bond coat and the top CMAS resistant layer. The CMAS resistant layers explored in this project include rare-earth monosilicate ($ReSiO_5$, REMS), REDS, and their combinations, with an intention to provide higher capability/durability relative to the current state-of-the-art EBC.

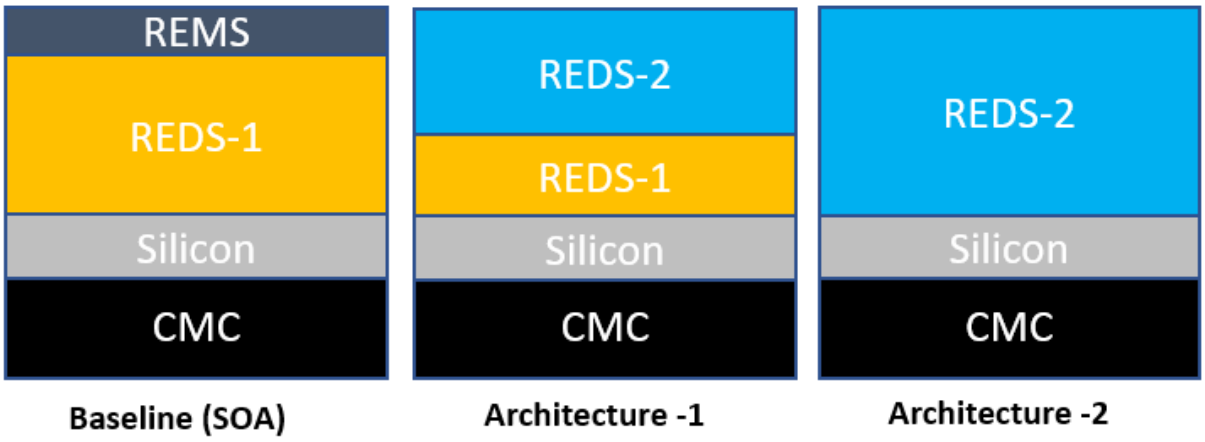

Figure 21: Three EBC architectures tested under this project

Performance of Architectures 1 & 2 are compared against the "state-of-the-art" (SOA) to establish improvement over a Baseline architecture.

GEA manufactured all samples for lab-scale testing and hardware for rig-testing. At the coupon level, the performance of the coatings was evaluated by lab-scale tests at NASA. At the rig level (single-cup flame tube combustion rig), testing of a CMC/EBC dome component at simulated engine conditions was performed at GEA to retire the established risks and demonstrate TRL5 maturity for one of the three EBC architectures.

NASA's test facilities probed: (i) coating volatility and permeability in high temperature steam environment (ii) thermo-mechanical capability using high flux laser rig (iii) CMAS resistance using high flux laser testing and (iv) hot particle erosion. A summary of laboratory-based testing is given in Table 5.

Utilizing the experimental data obtained using CMC/EBC coupons from the above tests, a comprehensive model to project the CMC/EBC durability will be generated by NASA, which will be leveraged to support the life prediction for combustion liners.

Table 5: Coupon-based laboratory testing conducted at NASA to assess EBC performance

EBC Coupon Test	Conditions
Steam Testing (Dimension 1"x 0.5")	Test Temperature: 2200 & 2400 °F Environment: 90% H_2O + 10% O_2 Duration: 500, 1000 & 2000 h Cycle: 1 h hot, 20 min cold (< 400 °F) Samples per architecture per condition: 3 Total Samples: 54
Thermal Gradient Testing (Dimension: 1" button)	Condition 1: T_{surf} ≈ 2600 °F T_{back} ≈ 2100 °F Condition 2: T_{surf} ≈ 2600 °F T_{back} ≈ 1900 °F Duration: 500 & 1000 cycles Cycle: 6 min hot/ cold Samples per architecture per condition/ duration: 2 Total Samples: 24
CMAS + Thermal Gradient (Dimension: 1" button)	Condition 1: T_{surf} = 2600 °F T_{back} = 2100 °F Condition 2: T_{surf} = 2600 °F T_{back} = 1900 °F Duration: 500 & 1000 cycles Cycle: 6 min hot/ cold Samples per architecture per condition/ duration: 2 Total Samples: 24
High Temperature Erosion Testing (Dimension: 1 " button)	Erodent Velocity: 100 & 135 m/s Particle (Al_2O_3) Size: 60 & 150 µm Sample Temp: 2200 °F Impingement: 30 & 90° Samples per architecture per condition: 3 Total Samples:72

3.3.1 High temperature steam exposure

Oxidation is a primary EBC failure mode in engine environments. When H_2O and O_2 molecules pass through the top barrier layers (REDS and REMS layers in our EBC architectures) and react with the silicon bond coat, SiO_2 (silica glass or crystobalite) is formed at the interface. CTE mismatch with surrounding phases, volume change associated with $\propto \leftrightarrow \boldsymbol{\beta}$ cristobalite transition near 428°F (220°C), and low mechanical strength of silica invite interface instability and delamination. Thus, we evaluate the efficacy of our topcoat layers by testing in high temperature steam and oxygen and measuring the resulting thickness of thermally grown oxide (TGO). These results populate an oxidation kinetics database to inform EBC lifing models.

The automated steam oxidation rig at NASA (Figure 22) suspends samples within a Pt wire basket in the furnace hot zone. The steam tube remains fixed in space and the furnace body translates vertically to cycle the samples from hot to cold. The isothermal hot condition is representative of bond coat temperatures during extremes of engine operation, and the cold condition is below the $\propto \leftrightarrow \boldsymbol{\beta}$ cristobalite transition temperature to invite maximum mechanical instability. Test conditions are summarized in Table 5.

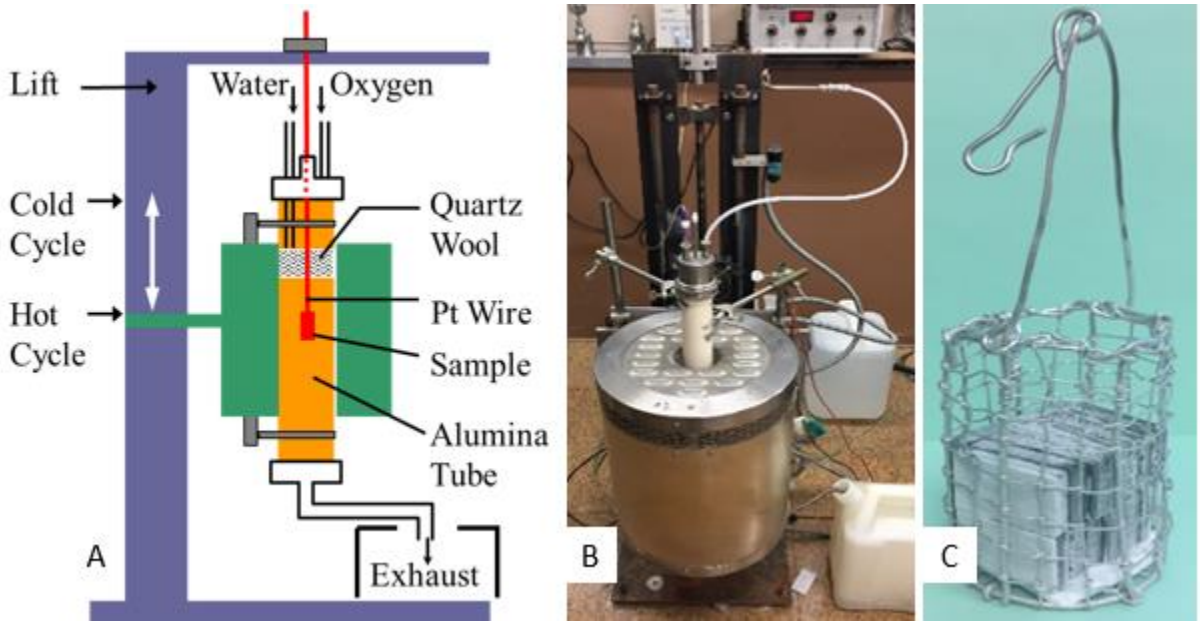

Figure 22: A) Schematic of NASA automated steam oxidation rig
B) Image of NASA automated steam oxidation rig in operation
C) Pt wire basket with CMC/EBC samples for steam oxidation testing

Oxide growth with time is represented with a linear-parabolic equation. (Deal B.E. and Grove A.S., J. Appl. Phys. 36 (12) 3770 (1965)). Shape of the oxide thickness curve depends upon value of parameters A and B. Oxide thickness can be reduced by increasing value of A or decreasing value of B (Sullivan R.M., J. Eur. Ceram. Soc. 39 (16) 5403-09 (2019)).

Equation 1: Linear-parabolic equation to describe TGO growth for uncoated or coated substrates

$$x_o^2 + Ax_o = Bt \ \ for\ uncoated\ or\ coated\ substrate$$

Equation 2: TGO equation parabolic rate parameter for either uncoated or coated substrates

$$B = 2\frac{\gamma_{ox}}{N_1}P \ \ for\ uncoated\ or\ coated\ substrate$$

Equation 3: TGO equation thickness rate parameter for uncoated substrates

$$A = 2\frac{D_{ox}}{k} \ \ for\ uncoated\ substrate$$

Equation 4: TGO equation thickness rate parameter for coated substrates

$$A = 2\frac{D_{ox}}{k} + 2\gamma_{ox}\sum_{i=1}^{\#\ coatings}\frac{\delta_i}{\gamma_{c\,i}} \ \ for\ coated\ substrate$$

Table 6: Linear-parabolic TGO equation constituents

x_o	Oxide thickness
t	Time
A, B	Parameters
P	Partial pressure of oxidant in gas environment
γ_{ox}	Permeability of oxidant in oxide
N_1	Molar density of oxidant in oxide
D_{ox}	Diffusivity of oxidant in oxide
k	Reaction rate constant
γ_i	Permeability of coating layer *i*
δ	Thickness of coating layer *i*

3.3.2 High heat flux laser testing without CMAS

Static thermal stress and cyclical thermal fatigue limit the suitability of many materials for use in jet engines. High thermal gradients can substantially strain coating materials and challenge their intrinsic fracture strength as well as layer interfaces. Cyclic thermal loading exploits material instability by introducing a range of transient stress states that must be tolerated by the material system repeatedly. For these reasons we ensure engine suitability of our EBC coatings by thermal cycling through relevant thermal gradients for liner conditions. Test conditions are summarized in Table 5.

3.3.3 High heat flux laser testing with CMAS

Calcium-Magnesium-Aluminum-Silicate (CMAS) deposits on hardware can form when engines ingest runway dust or airborne particulates such as volcanic ash. This can harm the EBC when melt penetrates micro-cracks in the coating to impart unwanted thermal stresses, and chemical reaction with rare earth mono/ disilicates at high temperatures can also degrade the EBC layers. Depending on the region of operation, this degradation mode may operate within the component lifetime. If instability associated with TGO growth is overcome, this is often the next degradation mode of concern for CMC/EBC hardware exposed to substantial dust/ash ingestion.

Table 7: CMAS Composition

Oxide	CaO	MgO	$AlO_{1.5}$	SiO_2
Mol %	30.67	8.25	12.81	48.27

CMAS glass tape (3/4 sample diameter) was applied to provide 8mg/cm^2 loading. Composition of the CMAS is reported in Table 7, with melt temperature near 2,264°F / 1,240°C. The tape was burned out at 2,400°F / 1,316°C for 0.5 h. Significant glass remained at the center and there were indications of mud flat cracking of the EBC under the glass. In heat treatment trials, small impurities were observed after recovery from 36 minutes at 2,400°F / 1,316°C (dark spot) likely from crucible fracture (ZrO_2) during cooling (Figure 23).

Figure 23: CMAS tape furnace application at 2,400°F/ 1,316°C
From left to right: before heat treatment, 12 min, 24 min, 36 min

3.3.4 High temperature solid particle erosion

Particle ingestion has the potential to reduce the service life of coating materials as the particles entrained in the gas stream impact surfaces and create micro-scale damage and material removal. In practice, other damage modes typically reduce EBC life to below the timeframe when this damage mode becomes dominant.

To study EBC erosion rate of our three architectures at NASA, a Mach 0.3 burner rig with particle injection is used to accelerate alumina erodent at high velocity and temperature to the EBC surface (Figure 24). Samples are exposed to 10 intervals of 1g erodent with weight measurement between each exposure. Erosion rate [mg/g] is determined by linear regression of last 6 data points from cumulative mass loss vs. cumulative erodent curves. Test conditions are summarized in Table 5.

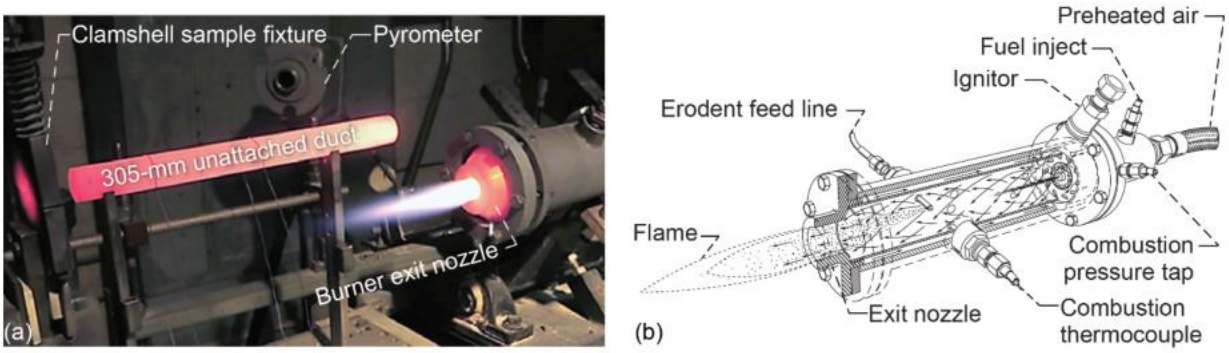

Figure 24: Modified Mach 0.3 Burner Rig with Particle Injection
(a) Burner exit nozzle, unattached duct, and sample holder (b) Burner placed before duct
** Presby et. al. NASA/TM-20230003935 *Presby. M and Harder B. Ceram. Int. 47 (12) 121026-1 (2021).*
**Fox et al. NASA/TM—2011-216986*

Erosion rate vs. particle kinetic energy (U_k) offers a convenient means for representing various particle masses (m_p) and velocities (v). The surface-normal component of velocity can be used to compare experiments where the erodent is delivered at various angles (α) to the surface ($U_{k,N}$).

Equation 5: Erodent particle kinetic energy

$$U_k = 0.5 m_p (v)^2$$

Equation 6: Surface-normal component of erodent particle kinetic energy

$$U_{k,N} = 0.5 m_p (v \sin\alpha)^2$$

4. Test Results / Analysis

4.1 Swirler Attachment

Metallic hardware components were procured from a combination of outside vendors or machined from material stock at the GE Evendale development machine shop. CMC Domes were fabricated at the GE Evendale CMC development shop.

The test plan shown in Figure 25 was used for the TCA (Tunable Combustor Acoustics) and HTP (High Temperature & Pressure) rigs. Since the G01 configuration does not employ a bolted joint, this configuration was tested in the TCA to get as much wear from combustor dynamics input before testing in the high temperature environment. For the G02 & G03 configuration, which have swirlers bolted to the CMC, they were tested in the HTP rig first to obtain the joint relaxation from hot temperature operation and related loss in clamp prior to testing in the TCA with the relaxed joint.

The cycle conditions shown for each rig in Figure 25 are representative of those experienced during commercial engine operation. For TCA, conditions are those in which known combustor dynamics are observed and well characterized in the baseline combustor.

TCA

Air Period	Config	Test Day Goals
1-2	G01	Rig check-out Dynamics mapping to compare to baseline Locate conditions to set for dynamics hold
3	G01	Go to identified dynamics point Hold dynamics at 4 psi pk-pk for air period
Swap configurations. Send flare/swirler & CMC deflector to Evendale to measure wear on G01 interfaces. Swap in G02 dome from HT&P		
4	G03	Go to identified dynamics point Hold dynamics at 4 psi pk-pk for air period
Swap configurations. Send G02 assembly to Evendale, do not disassemble bolted joint. Swap in G03 configuration from HT&P		
5	G02	Go to identified dynamics point Hold dynamics at 4 psi pk-pk for air period
Remove G03 dome. send G02 assembly to Evendale, do not disassemble bolted joint.		

HT&P

Air Period	Config	Test Day Goals
1	G03	Rig check-out While heating up monitor strain gauges As time allows complete temp hold at T/O conditions
2	G03	Go to cruise condition, take interface temperatures Go to climb condition, take interface temperatures Go to T/O condition, hold for test period
Swap configurations. G02 dome to be put into TCA. Swap in G01 dome after getting wear data from Evendale		
3	G01	Go to cruise condition, take interface temperatures Go to climb condition, take temperatures Go to T/O condition, hold for test period
Swap configurations. Send G01 flare/swirler & CMC deflector to Evendale to measure wear. Swap in G03 configuration		
4	G02	Go to cruise condition, take interface temperatures Go to climb condition, take interface temperatures Go to T/O condition, hold for test period

Figure 25: Single Cup Rig Executed Air Periods

4.1.1 TCA Rig Testing

Testing in the TCA started with the G01 configuration, testing of the G02 & G03 configuration was done in the TCA after that hardware had completed their test period in the HTP rig. Test data were similar for all three configurations, a summary from the TCA test period from the G01 is shown in Figure 28 as representative of the conditions the CMC assemblies were exposed to.

Each TCA dwell period was set to expose the CMC assembly to over 10,000,000 cycles at a target average amplitude. This would meet the HCF cyclic requirement and amplitude which combustor components are expected to endure during their operational life.

Figure 26 shows pictures of the G01 assembly mounted in the test rig prior to testing.

Dome assembly with fuel nozzle assembled to mount plate prior to installing into rig

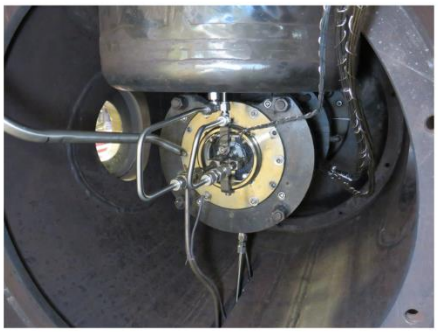

Test article built-up inside pressure vessel prior to closing rig for test

Figure 26: TCA Rig Assembly Build-Up Images

Initial test periods for the TCA covered a rig shakedown to ensure rig, facility, instrumentation, and test article are performing as required. These initial test periods also included combustor dynamics mapping to compare the response with the single wall CMC dome to that of a double wall metallic dome used in the baseline to see if the dome change caused any changes in frequency or amplitude. During this mapping phase the combustor dynamics dwell point conditions were identified. Dynamics mapping showed the single wall CMC dome did not have a significant change in the dynamics response of the combustor from the baseline.

Figure 27 shows the P4' frequency response between those measured in the TCA during HyTEC testing. The TCA showed a good match in the peak frequencies matching those observed in the engine.

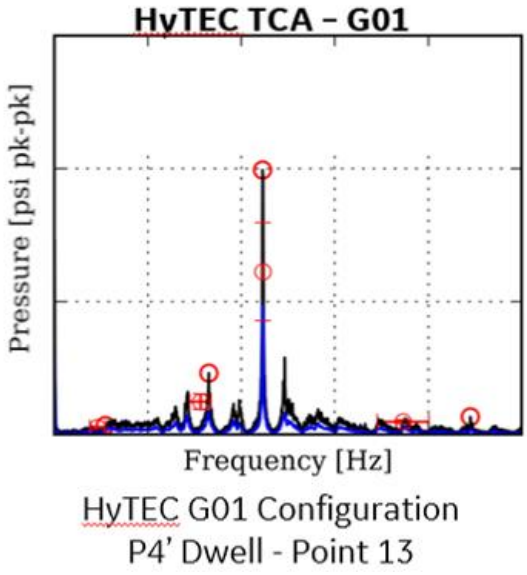

Figure 27: TCA P4' Frequency Response

The following figures outline how each of the test period was executed.

Figure 28 shows a test period in the TCA. The top graph shows the combustor cycle conditions (Pressure, Temperature, Fuel/Air Ratio); the bottom graph shows the measured combustor dynamics during the test with the phases of the test outlined.

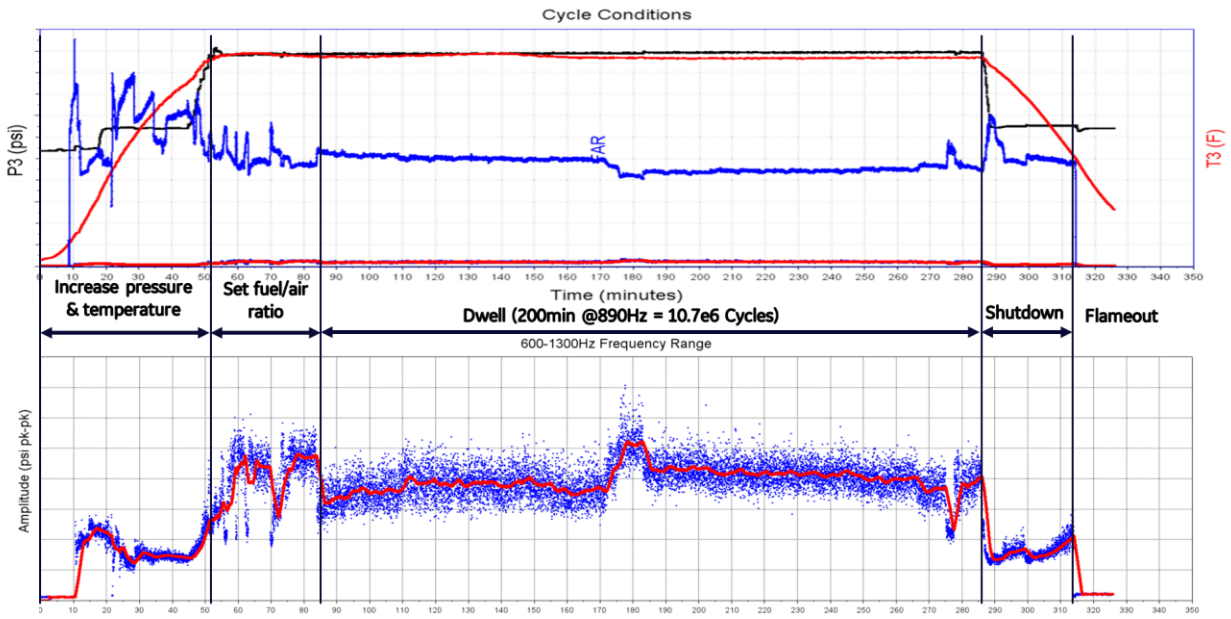

Figure 28: TCA Test Period Summary

Throughout testing the frequency response was monitored. Checking the frequency response remained representative of engine operation, similar to that shown in Figure 27.

Instrumentation in the flare pieces recorded temperatures on the hot side of the flare as a comparison to baseline to check the effects of the attachment methods did not impact the flare cooling. Thermocouples were also fitted on the metal piece at the metal/CMC interface to document the temperature at the interface for later use in evaluating nickel diffusion into the CMC. Figure 29 shows the flare temperatures on the G01 configuration during TCA testing. Hot side flare temperatures in the HyTEC campaign were all within the range of previous tests done during the baseline combustor development.

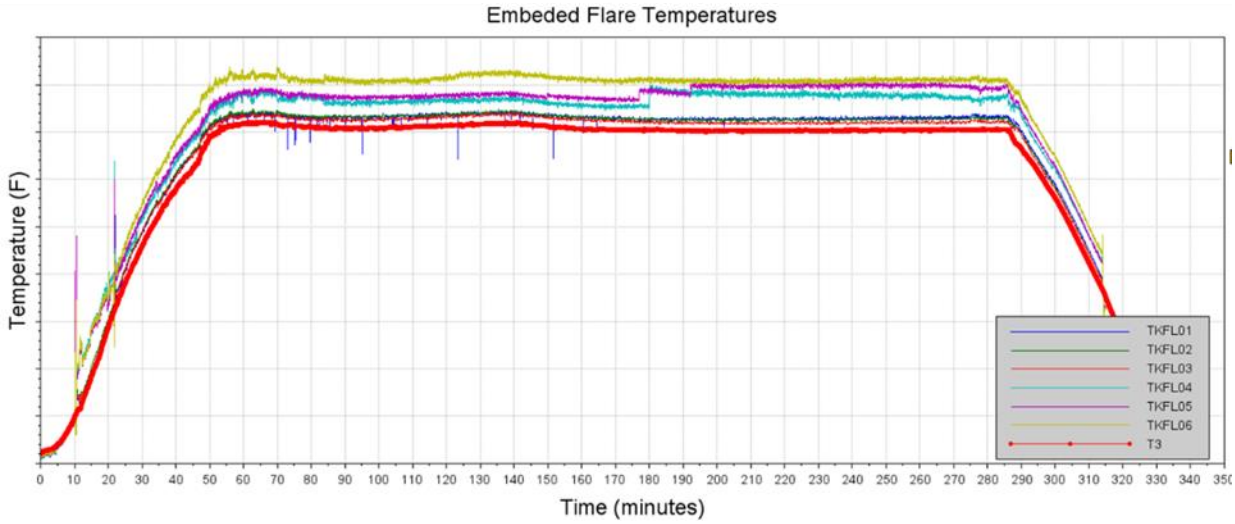

Figure 29: TCA Flare Temperatures

Interface temperatures between the flare and CMC were close to T3, a more detailed breakdown of interface temperatures for the different configurations are documented in the HTP rig test results as that testing covered cycle conditions representative of commercial engine testing.

4.1.2 HTP Rig Testing

HTP testing began with the G03 configuration as the G01 configuration was testing in the TCA. Test data were similar for all three configurations, a summary from the HTP test period from the G01 is shown in Figure 31 as representative of the conditions the CMC assemblies were exposed to.

Each HTP rig test period was structured to mimic the engine cycle conditions representative of the cruise, climb, and take-off phases of commercial engine. Once the take-off condition was reached, the rig would be held at that condition for the reminder of the test period before flaming out. Data was collected at each of the cycle conditions to record temperature data at the CMC to metal interface for later evaluation of Ni diffusion.

Figure 30 shows the G03 assembly in the HTP test article mount prior to being installed into the pressure vessel.

Figure 30: HTP Test Article Assembly

Similar to the TCA testing, the initial test period was used as a rig check-out to verify correct functioning of the rig and instrumentation. Subsequent test periods would step through the representative cycle conditions and complete a dwell at take-off conditions for the remainder of the test period. Figure 31 plots the pressure (P3), temperature (T3), and fuel air ratio (FAR) during a test period.

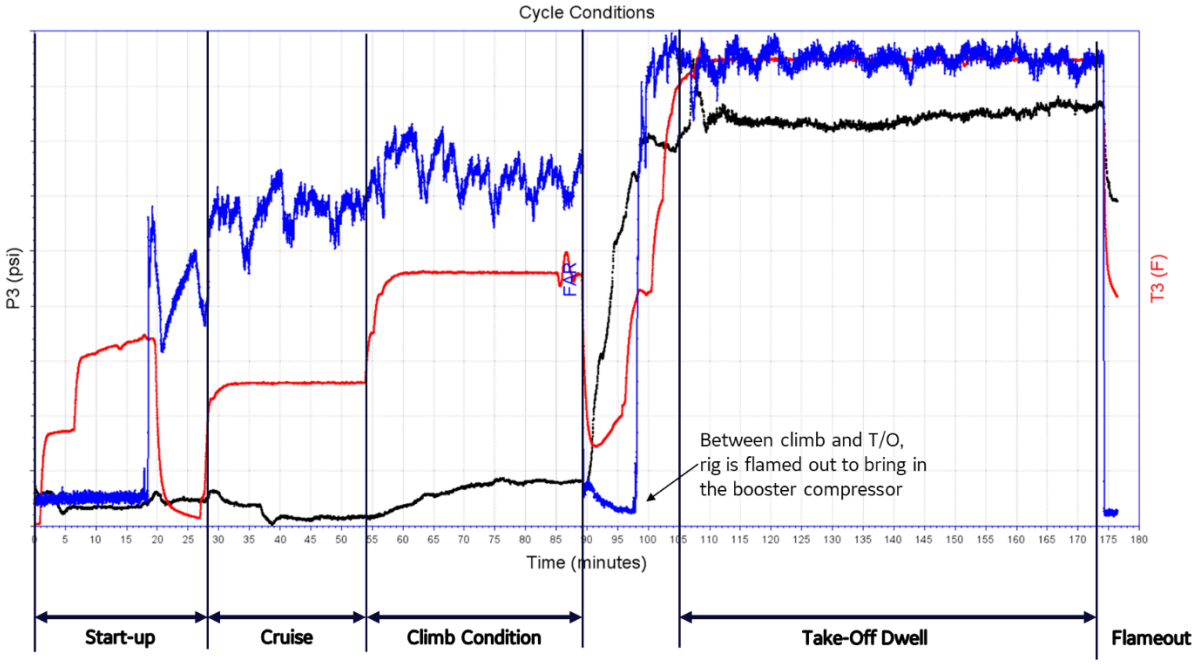

Figure 31: HTP Test Period Summary

Figure 32 shows the temperature measured on the G01 configuration. The CMC to metal interface thermocouples measured approximately 40°F over T3 for the test period for all cycle conditions. Flare temperatures show a dependence on the FAR & P3 conditions. For the HTP the fuel flow and pressure are higher than the cold cruise point being run on the TCA. As such there are changes to the fuel spray characteristics. At cruise and climb conditions, the temperatures increase with the higher gas temperature, at Take-off power the fuel impinges on the flare acting as liquid cooling on the surface of the flare resulting in temperatures below T3.

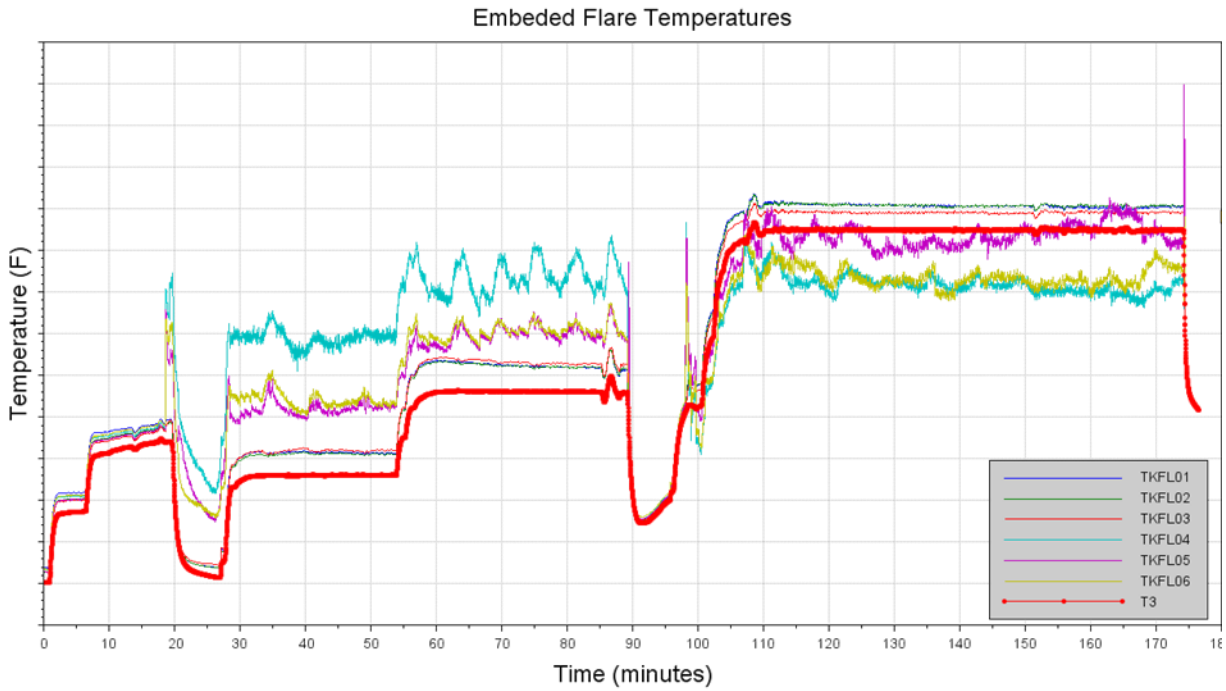

Figure 32: HTP Flare Temperatures

Measured temperatures on the metal to CMC interface in both the G01 and G02 configurations showed the G02 had higher temperatures all conditions. The G02 bolted assembly has metal around the CMC, so part of the interface is inside the combustor resulting in the higher temperature at the interface.

4.1.3 Single Cup Hardware Condition

During configuration swaps in the TCA and HTP, hardware was inspected for distress and documented. The figures in this section show representative images for the condition of the assembly components from new make to completion of testing. All hardware was found in serviceable condition with no meaningful distress.

Figure 33 and Figure 34 show the swirler/flare assembly and CMC dome for the G01 configuration. For the flare, like with subsequent configuration carbon build up on the hot surface present as this configuration ran at low power allowing for this coke to build up. This material is burnt up during high power operation of the HTP.

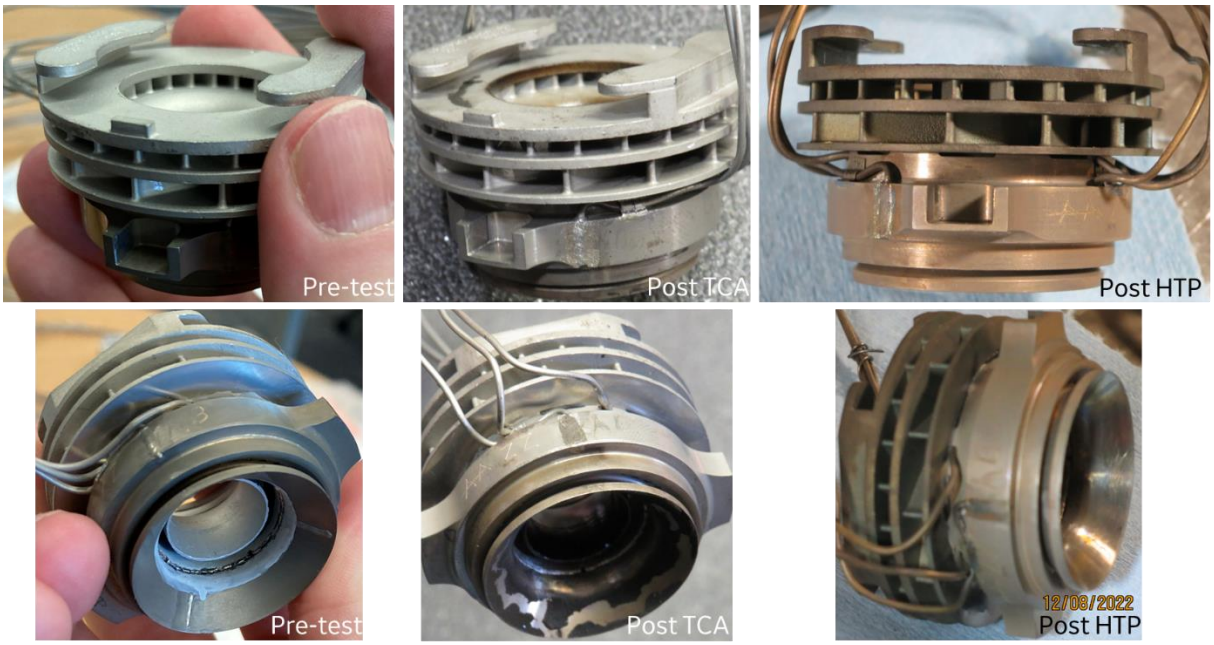

Figure 33: G01 Swirler/Flare Assembly Images

Figure 34: G01 CMC Dome Images

Figure 35 shows the G02 assembly condition during testing. The assembly remained together during both TCA and HTP tests with the bolted joint clamped. There is no evidence of swirler rotation relative to the dome indicating the assembly remained clamped at power.

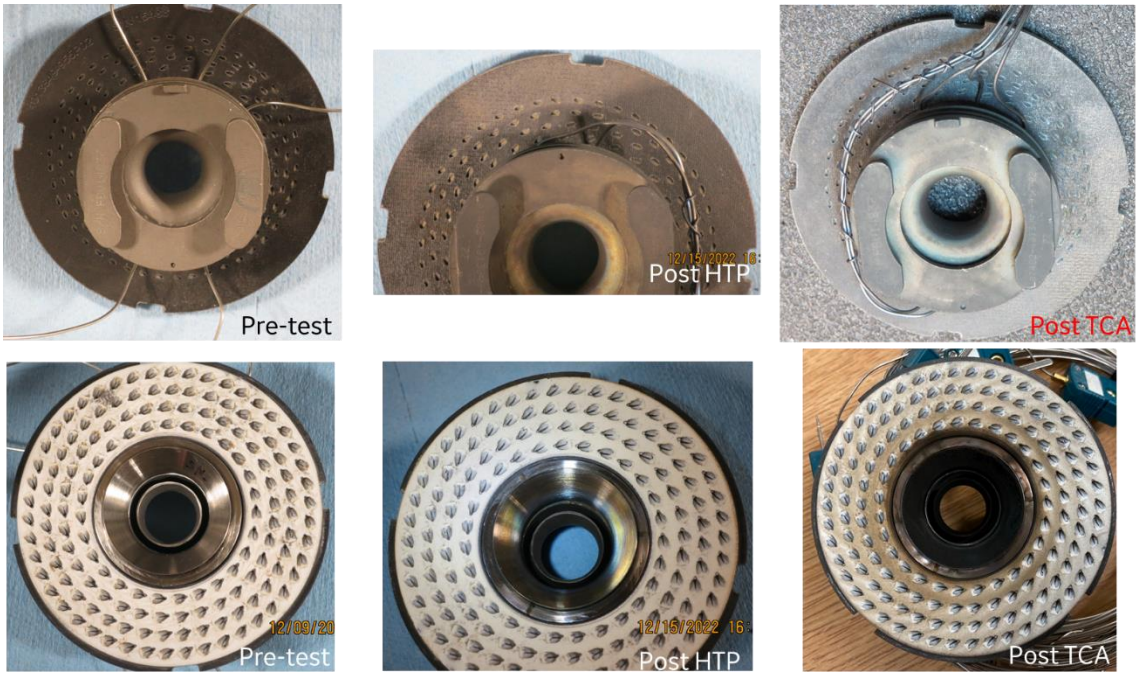

Figure 35: G02 Assembly Images

Figure 36 shows the G03 assembly condition during testing. The assembly remained together but comparing the images between the HTP and TCA shows evidence there was some amount of rotation of the swirler in the assembly. Aerodynamic and thermal test data for the configuration were consistent with the previous two, which would be indicative that the swirler was not in free rotation and continued to provide a stable flame. Furthermore, a swirler in free rotation would cause flame out of the rig as the swirler would no longer be swirling the air to mix the fuel and air. In addition, there were no wear marks on the assembly to indicate the part was rotating freely. At cold condition, the part remained clamped to the CMC dome. It is theorized that the dynamic input from the TCA combustor dynamics caused the swirler to walk around the assembly.

The forward side images of the assembly include dashed lines in the HTP and TCA images, in which the dome assembly was set in the same orientation to visually see the amount of rotation observed of the swirler during TCA testing.

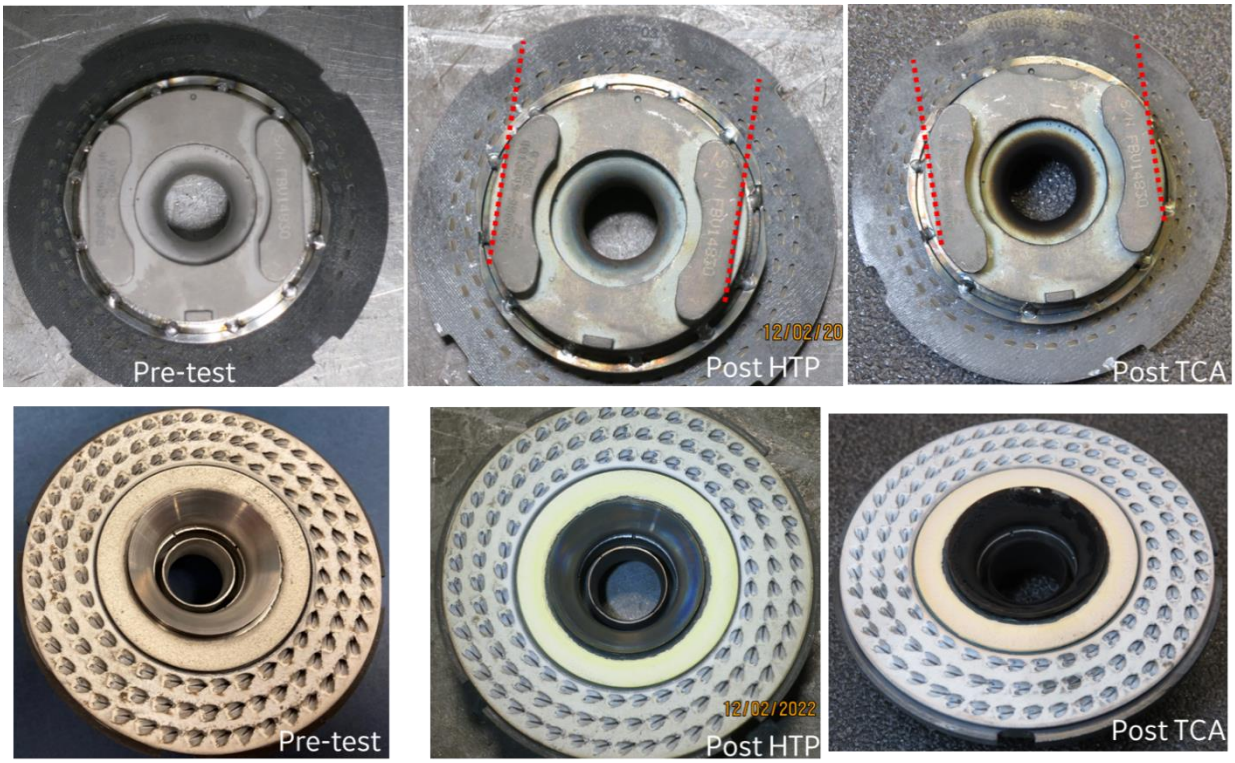

Figure 36: G03 Assembly Images

4.1.4 Furnace Testing & Post-Test Bolted Joint Assessment

In addition to the testing done on the TCA and HTP rigs, a spare set of G02 and G03 assemblies were used to do a furnace test to evaluate the effect of relaxation on the bolted joints from prolonged operation at high temperature as an engine in commercial service would experience from repeated take-off cycles. Figure 37 shows the bolt preload loss due to relaxation on a typical combustor bolted joint.

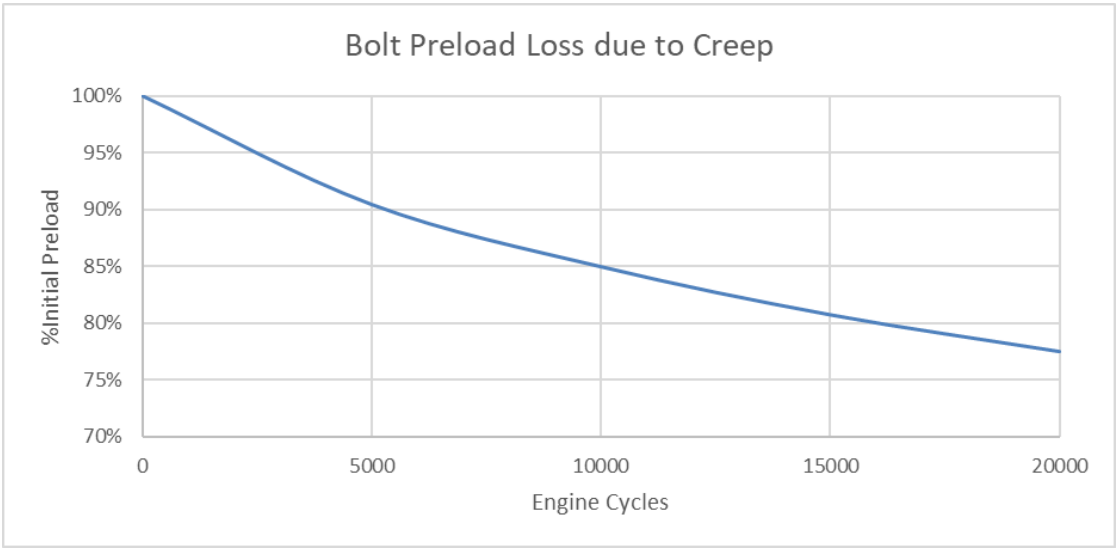

Figure 37: Typical Combustor Bolted Joint Preload Loss Over Engine Cyclic Operation

Most of the loss occurs within 10,000 engine cycles. The furnace test was devised to run continuously for 72 hours at temperature to simulate 10,000 cycles worth of pre-load. Like the assemblies tested in the TCA and HTP, the new make torque was measured, and then a slip test was done to measure the amount of torque required to make the swirler rotate.

For reference the swirler is calculated to impose an aerodynamic torque of <5% of the required torque during high power operation. Cold to hot analysis of the bolted joint calculates a 35% loss of clamp load at hot condition.

Table 8 records the measurement taken of the swirler/flare torque values. The slip value is the torque applied to the swirler (in the tightening direction) to make it rotate, the break-away value is the torque required to dis-assemble the bolted joint.

Table 8: G02 & G03 Slip and Break-Away Torque Values

	TCA/HTP Hardware		Post Furnace Exposure		Retorque to New Make Torque	
	Slip Value	Break-Away	Slip Value	Break-Away	Slip Value	Break-Away
G02	50%	64%	16%	24%	100%	100%
G03	30%	14%*	56%	429%**	100%	100%

All values reported as a percent of torque at new make for each configuration.

** Measured torque was below the minimum of the gauge being used.*
*** During dis-assembly a bang was heard prior to the joint coming loose. Likely the bolted joint had seized.*

Data shows that both single cup testing as well as the furnace test caused a loss of clamp load, as observed by the decrease in slip value. The G02 and G03 assemblies were affected differently, with the G02 showing the greatest loss of clamp load after long term exposure to elevated temperatures during the furnace test, losing 84% of its clamp load at cold after the test.

4.1.5 Metal to CMC Interfaces Wear Analysis

After testing and disassembly, the hardware tested in the TCA and HTP rigs was given to the lab for evaluation of the wear interfaces. Inspection was done with an accuracy of up to 0.0002". Table 9 summarizes the wear seen on the CMC to Metal interfaces, as well as the metal-to-metal interfaces on the anti-rotation tabs used in the G01 design. The measured wear is compared to the TPM criterion set prior to the test.

Table 9: CMC and Metal Interfaces Wear Summary

Interface	CMC Wear	Metal Wear	Combined	NASA TPM Criteria
G01 Swirler/Dome	<38% of Req.	< 38% of Req.	< 77% of Req.	< 77% of Req. (Goal) < 100% (Requirement)
G01 Anti-Rotation	N/A	< 13% of Req. (tabs) < 13% of Req. (swirler)	< 25% of Req.	< 25% of Req. (Goal) < 100% (Requirement)

All values reported as a percent of the requirement

For all configurations the amount of wear on the interfaces was well under the target limits set in the TPMs. There was recorded chipping on the outer diameter of some of the CMC domes where they interface with the rig. This interface is not part of the swirler attachment design and is a rig specific interface that would not exist in an engine application. Figure 38 shows the largest chip measured, it was on the G03 dome. Chipping is likely due to handling damage as the edge is unprotected when the part is not installed in the rig. The chip is very localized and does not impact the test results.

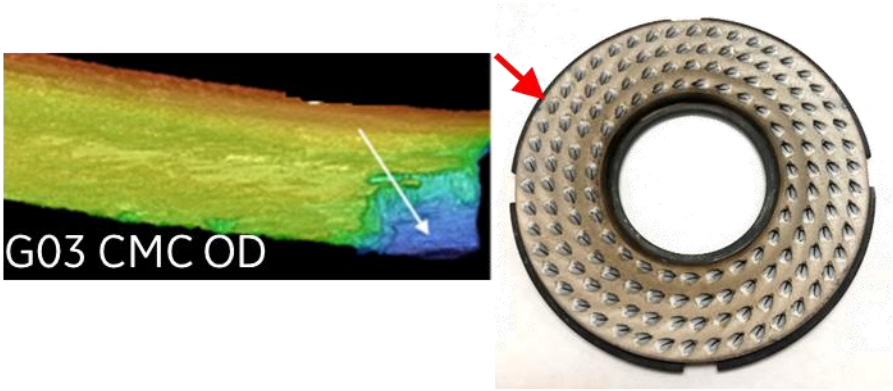

Figure 38: Chipping Detail on CMC Dome Outer Diameter

4.2 Nickel Diffusion

4.2.1 Nickel Diffusion Model

The deepest nickel diffusion depth into the CMC measured during the testing period was analyzed by the modeling team at NASA to try and generate a diffusivity model to predict the diffusion that the swirler will experience over the life of the hardware. Utilizing The Mathematics of Diffusion by John Crank[5], the local, time-dependent nickel mass conservation differential equation for a 1D diffusion into a semi-infinite media with no chemical reaction and a constant diffusivity (D), Equation 7 was used. It is schematically shown in Figure 39.

Equation 7: Differential equation and boundary conditions for 1D diffusion solution

$$\frac{\partial C}{\partial t} + \frac{\partial}{\partial x}\left(-D\frac{\partial C}{\partial x}\right) = 0 \; ; BC: C(0,t) = C_s \; ; IC: C(x,0) = 0$$

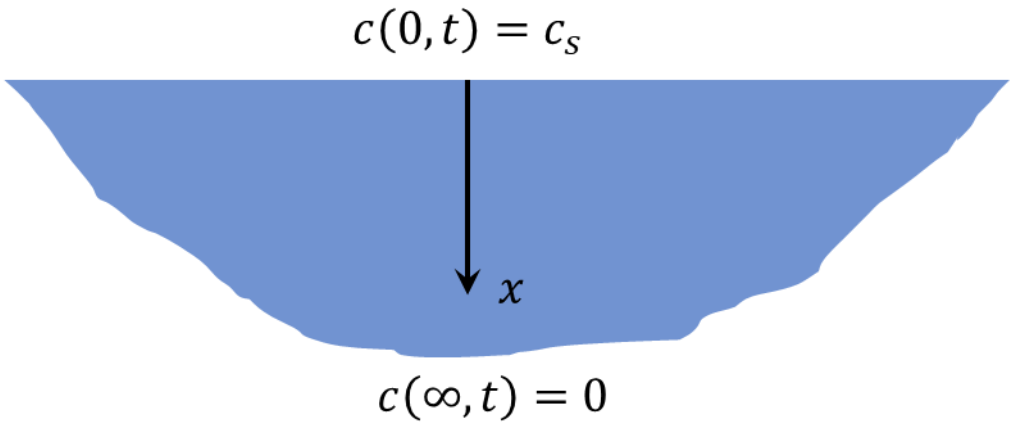

Figure 39: Schematic representation of the boundary conditions for the 1D diffusion equation

The solution to the differential equation is outlined in Equation 8, where C_s is the Ni concentration at the interface within the CMC.

Equation 8: Solution to the differential equation for the 1D diffusion

$$c(x,t) = C_s erfc\left(\frac{x}{2\sqrt{Dt}}\right)$$

or

$$1 - \frac{C}{C_s} = erf\left(\frac{x}{2\sqrt{Dt}}\right)$$

Solving Equation 8 for x when c = 0 leads to
Equation 9. Note, D in this equation is not a function of the Ni concentration.

Equation 9: Solution of Equation 8 to obtain the equation for the diffusivity. Note D is not a function of the concentration.

$$\frac{x}{2\sqrt{Dt}} > 2 \longrightarrow x > 4\sqrt{Dt} \longrightarrow D = \frac{x^2}{16t}$$

Table 10: Calculated diffusivity from the deepest measured penetration for the two alloys, René N5 and Inconel 600, and at the three different temperatures of 1,600, 1,700, and 1,800°F

alloy	Temperature (F)	Time (hr)	Measured depth (mils)	Measured average penetration	Diffusivity (m2/sec)	Average Diffusivity (m2/sec)
Rene N5	1600	50	16.5504, 13.7839	0.385245	5.15E-14	4.37E-14
		100	13.3453, 26.3535	0.504175	4.41E-14	
		200	11.7555, 38.4713	0.63788	3.53E-14	
	1700	50	33.722, 33.1791	0.849645	2.51E-13	1.86E-13
		100	43.9043, 29.6811	0.934535	1.52E-13	
		200	57.6453, 47.7441	1.338445	1.56E-13	
	1800	25	78.9224, 85.3354	2.086075	3.02E-12	3.30E-12
		50	148.8024, 122.9756	3.45158	4.14E-12	
		75	147.6409, 123.7819	3.44707	2.75E-12	
Inconel 600	1600	50	12.2752, 4.1047	0.208025	1.50E-14	2.04E-14
		100	16.2980, 10.1969	0.336485	1.97E-14	
		200	19.7797, 23.6256	0.551247	2.64E-14	
	1700	50	22.7287, 33.0039	0.707805	1.74E-13	1.79E-13
		100	33.4496, 47.8906	1.03302	1.85E-13	
		200	60.2343, 52.1469	1.42724	1.77E-13	
	1800	25	32.2307, 51.4181	1.06234	7.84E-13	1.80E-12
		50	98.5965, 99.2051	2.51208	2.19E-12	
		75	148.6244, 106.3717	3.23845	2.43E-12	

Using
Equation 9, the data for René N5 and Inconel 600 at all three temperatures in the Table 19 (Appendix), the diffusivity for each material and temperature pair was calculated. The data from the HastX was not included in the modeling effort due to the scatter in the diffusion measurements, likely caused by the low nickel

concentration in the alloy. This behavior needs further investigation. There were two tests performed for each material, temperature, and time condition. The average depth of the two was used for x in Equation 8. The calculated diffusivities at the three-time durations were averaged to yield a diffusivity for each alloy and at each temperature. All the data is reported in Table 10.

The log of the diffusivity for the data in the last column of Table 10 was graphed vs 1,000/T(K) and is shown in Figure 40. Two linear fits were performed on the data. The linear fit of y = -57.87x + 19.001 with the higher R^2 value (0.998 compared to 0.9544) was used to generate the Arrhenius equation for the diffusivity as a function of temperature. Converting the linear equation y = -57.871x + 19 to the Arrhenius equation for diffusivity as a function of temperature gives (Equation 10).

Equation 10: Arrhenius equation for the diffusivity as a function of temperature (Kelvin)

$$D(T) = e^{19.001} \times e^{\left(\frac{-57,871}{T}\right)} \frac{m^2}{sec}$$

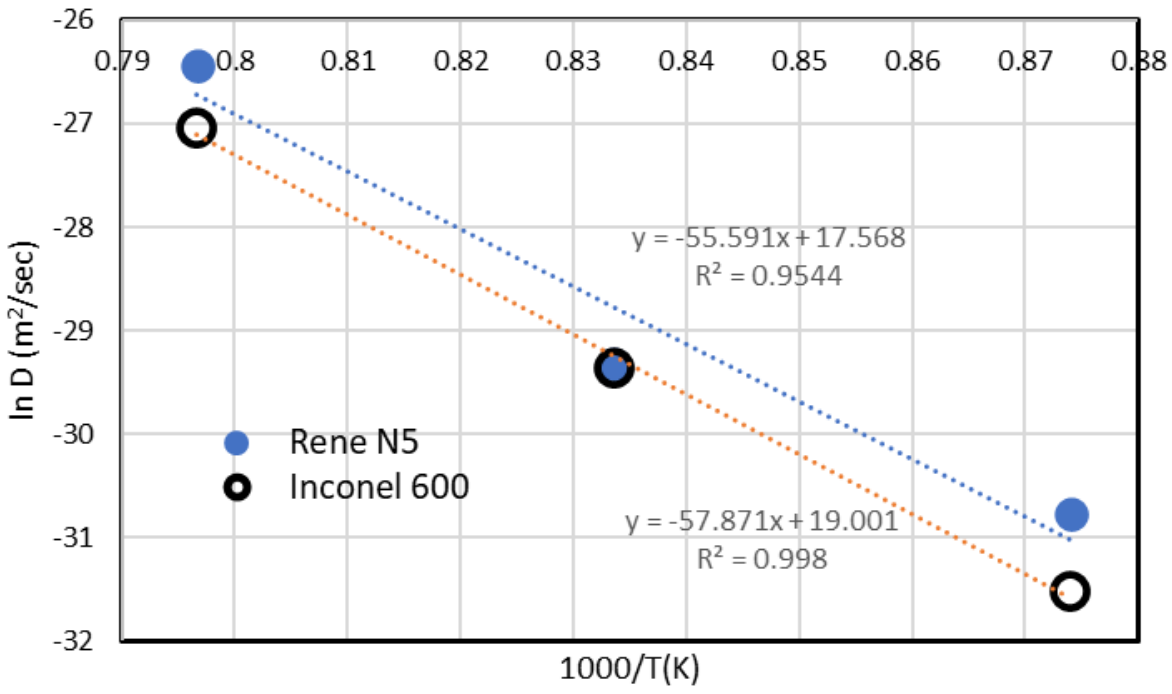

Figure 40: The log of the diffusivity vs the inverse temperature for René N5 and Inconel 600 at 1,600, 1,700, 1,800°F

Table 11: Wt.% Ni in the alloy, Wt.% Ni in the CMC at the interface with the alloy, and the conversion of C_s to mol/m³

Alloy	Ni Conc. in alloy (%)	C_s (%)	C_s (mol/m³)
René N5	63.45	35	19100
IN600	76.83	45	24557

The nickel concentration, regardless of the time duration of the test, at the interface with the alloy for the René N5 and the Inconel 600 were 35 and 45 Wt.%Ni, respectively (Table 11). This is the only noticeable

difference between the two alloys for all the tests run at 1,700°F. The penetration depth of the nickel into the CMC did not appear to be affected by the nickel content in the alloy. There is a linear trend (Equation 11) of the nickel concentration in the CMC at the interface (x=0) versus the percentage of the Ni in the alloy, graphed in Figure 41. Additional data points are needed to check if the trend is truly linear, as this is based on only two data points and the initial condition C(0,0) = 0.

Equation 11: Linear relationship between nickel concentration in the alloy (x) and the nickel concentration in the CMC at the interface

$$y = 0.5719x;\ R^2 = 0.9991$$

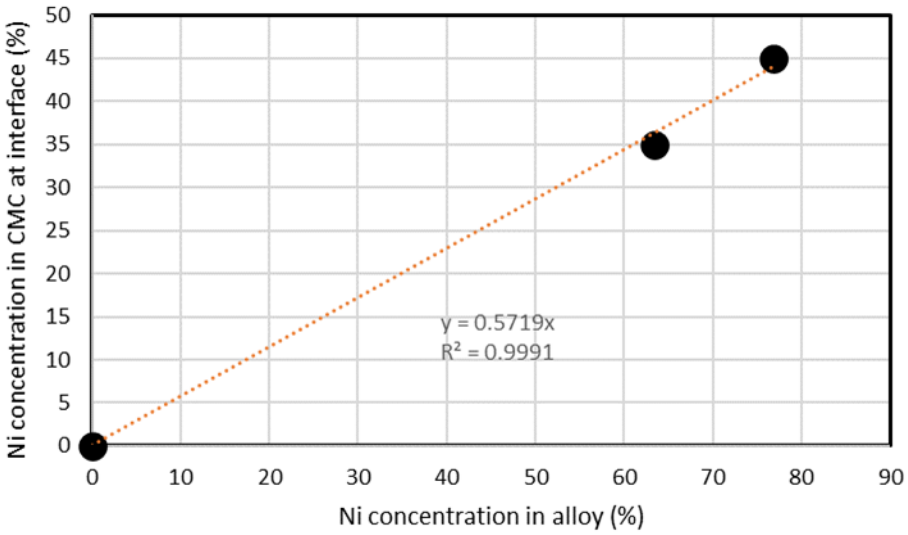

Figure 41: Nickel concentration in the CMC at the interface with the alloy as a function of the nickel concentration in the alloy

The diffusion behavior for the tests run at 1,700°F for the Inconel 600 and René N5 were further characterized by line scan and are presented in Figure 42 and Figure 43, respectively. The diffusivity model was graphed against the data generated for the N5 and Inconel 600 tests performed at 1,700°F for 50, 100, and 200 hours. For each condition there were two separate, independent tests performed. The diffusivity model had good agreement with all 12 tests as can be seen in Figure 42 and Figure 43. Furthermore, examination of the tests run at 1,800°F, utilizing René N5 as the alloy, it appears that there is no discernable difference between the 50 and the 75-hour tests other than the total diffusion depth Figure 44. This is consistent with the observations of the tests run at 1,700°F for the René N5 and Inconel 600.

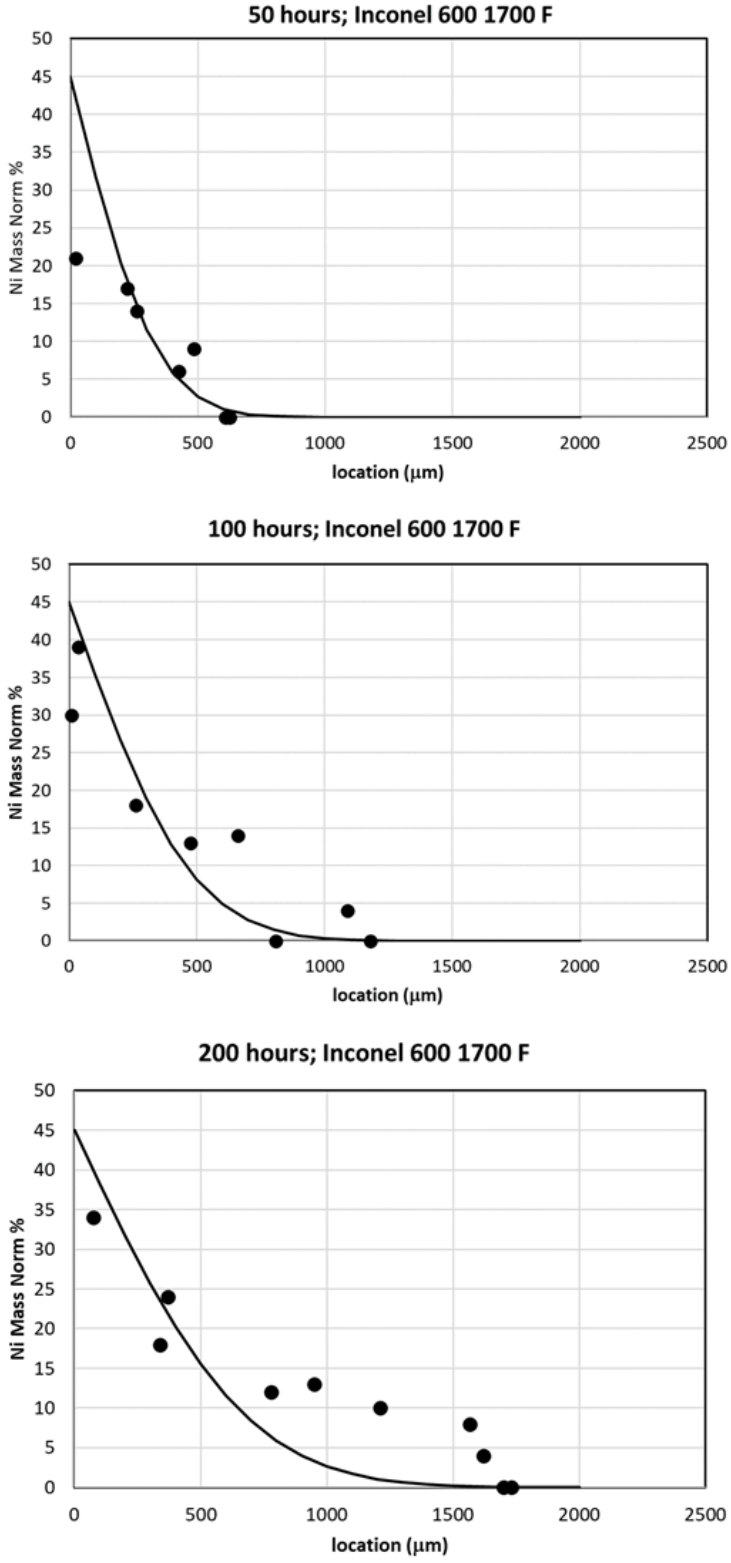

Figure 42: Wt% Ni through the thickness of the CMC for tests run against Inconel 600 at 1,700°F for 50, 100 and 200 hours. Two independent tests for each condition.

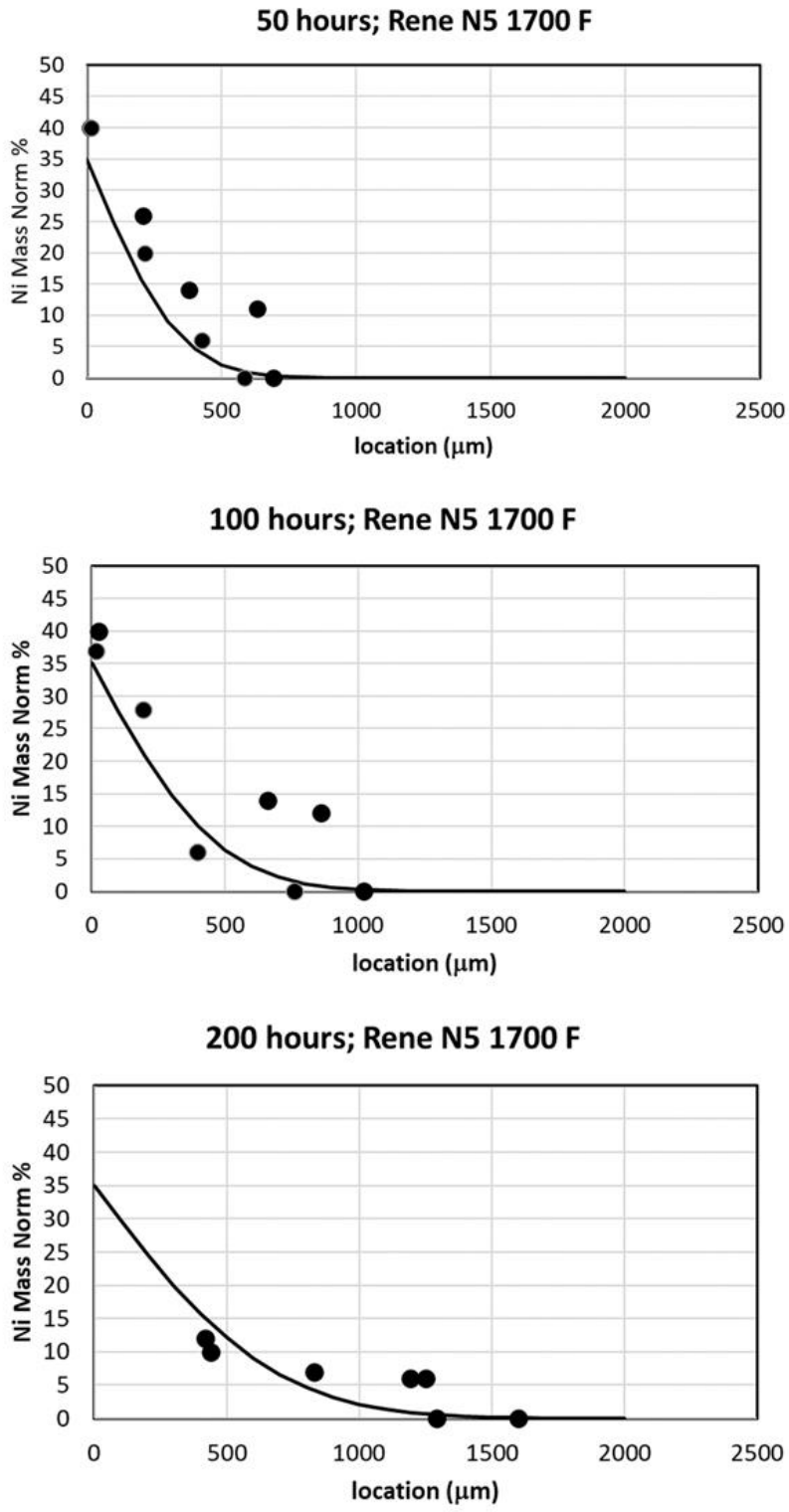

Figure 43: Wt% Ni through the thickness of the CMC for tests run against René at 1,700°F for 50, 100 and 200 hours. Two independent tests for each condition.

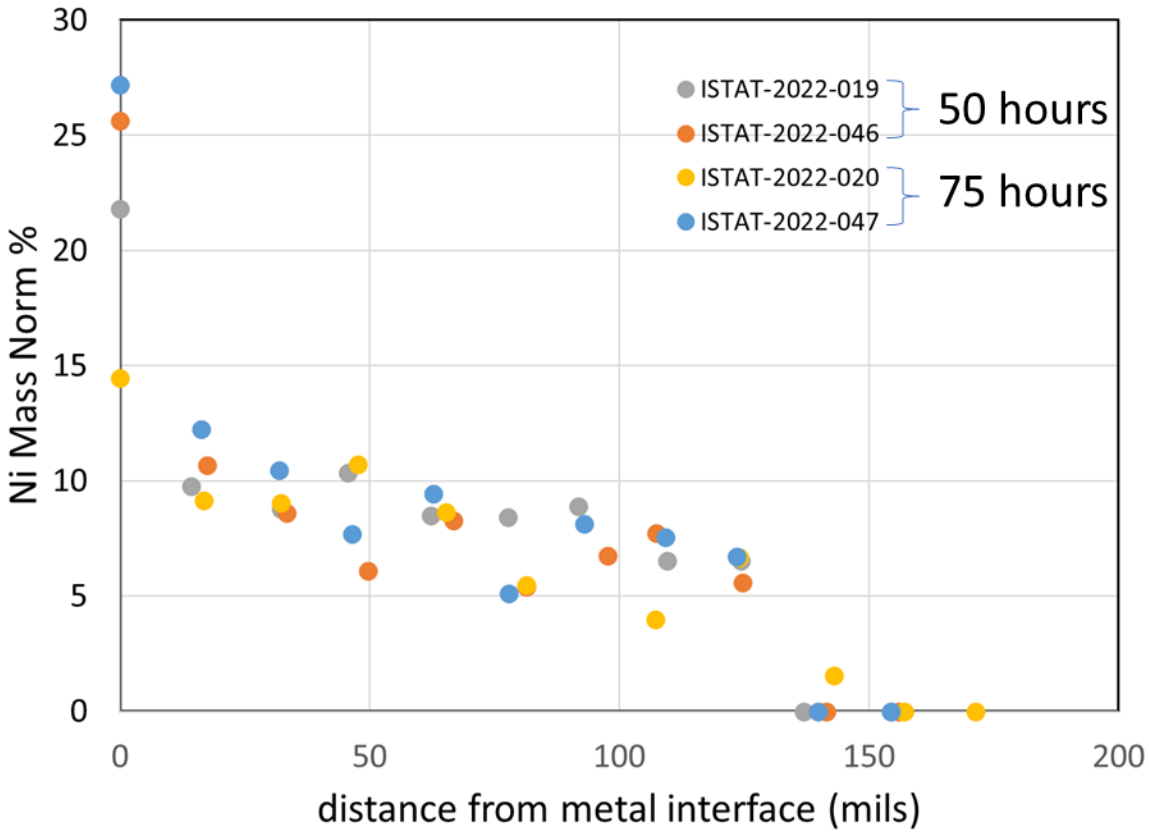

Figure 44: EDX measurements of the %Ni mass of tests run at 1,800°F against René N5 for 50 and 75hrs

Table 12: Diffusion calculation for the G01 & G02 configurations based on the HTP test temperatures and a typical narrowbody mission profile for a target life of the combustor dome

Configuration	Cycle condition	Time for target life (hours)	Temperature at Interface (°F)	Diffusivity (m^2/sec)	Ni Diffusion into CMC (mils)
G01	Cruise	~20,000	1,000	1.80E-23	0.01
	Climb	~6,500	1,111	2.80E-21	0.04
	Take-off	~400	1,300	3.50E-18	0.30
				Total	0.35
G02	Cruise	~20,000	1,165	2.50E-20	0.20
	Climb	~6,500	1,275	1.50E-18	0.90
	Take-off	~400	1,455	4.20E-16	3.90
				Total	5.00

For the G01 and G02 configurations, the temperature for cruise, climb and take-off were measured by thermocouple attached to the flare during the HTP tests. The times for the different cycle conditions are taken from a typical narrowbody mission and target narrowbody combustor life. Utilizing the diffusivity Equation 10 and diffusion depth
Equation 9, the diffusion depth for all three cycle condition was calculated and the total expected diffusion was calculated for the life of the combustor dome (*Table 12*). The total calculated diffusion depth for the G01 and G02 are 0.35 and 5.0 mils, respectively. Relative to the overall thickness of the part, these levels of diffusion are minimal and should help to mitigate any impact on the durability of the components.

4.2.2 Mechanical Properties of Diffusion Product

Table 13: Tensile test data of Ultimate Tensile Strength, Elastic Modulus, and Proportional Limit at 70, 1,500, 2,200, and 2,400°F

Temp (F)	Specimen ID	Thickness (in)	Width (in)	UTS (Ksi)	E (Msi)	PL (Ksi)
70	15590-TD3	0.0713	0.4008	60.81	29.5	15.24
70	15597-TD1	0.0701	0.4007	46.39	35.5	21.3
1500	15591-TD4	0.0728	0.4009	46.89	33.6	29.27
1500	15597-TD2	0.0699	0.4008	40.49	37.4	24.01
2200	15591-TD5	0.0733	0.401	39.87	20.9	17.53
2200	15595-TD3	0.0693	0.4005	38.45	26.1	21.05
2400	15595-TD1	0.0684	0.4011	38.73	21	17.29
2400	15596-TD5	0.0682	0.4005	30.31	20.3	16.07
70	15881-TD5	0.0739	0.4004	62.22	29.2	16.17
70	15892-TD3	0.0744	0.4008	58.15	31.1	19.67
1500	15883-TD2	0.0729	0.3999	52.89	29.9	19.03
1500	15884-TD5	0.0735	0.4015	38.51	32.2	27.11
2200	15884-TD1	0.0736	0.4004	40.82	30.7	28.52
2200	15892-TD4	0.0744	0.4012	41.59	26.7	24.64
2400	15884-TD2	0.0734	0.4005	40.15	19.7	16.06
2400	15885-TD3	0.0741	0.401	27.08	16.8	14.36

The tensile test data for the mechanical testing of the diffused CMCs per ASTM C1359 is listed in Table 13. The Young's Modulus was determined by using the stress and strain data obtained between the stress of 2 Ksi (13.8 MPa) and 15 Ksi (103 MPa). The proportionality limit (PL) was determined by generating a line running parallel to the elastic modulus slope at a strain axis offset of 0.00005 in/in (0.00005mm/ mm).

The temperature effect on UTS, for diffused CMC, between 70 and 2,400°F is shown in Figure 45.

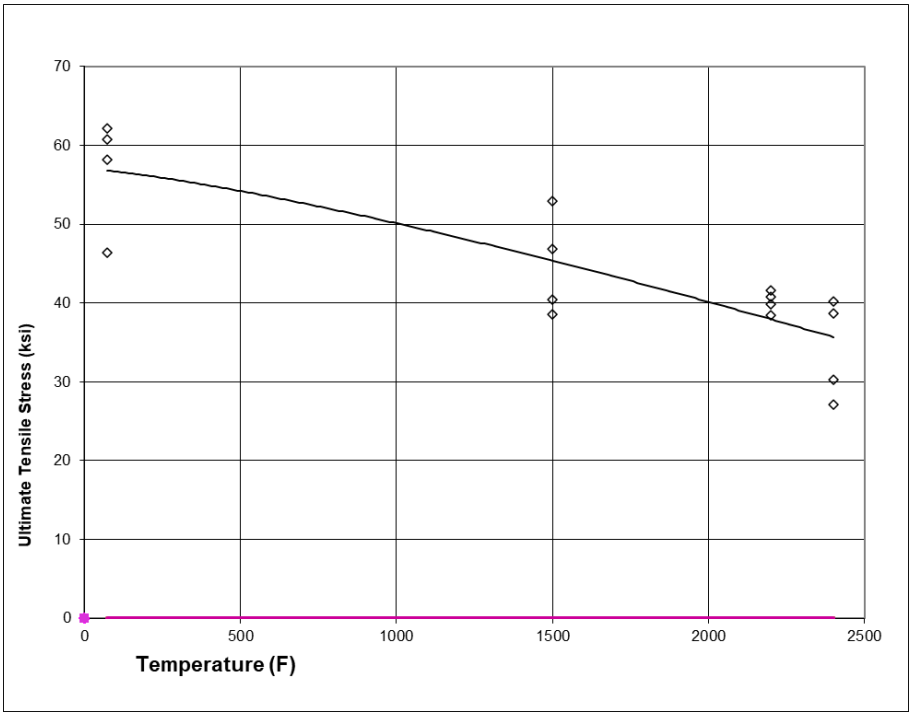

Figure 45: Graph of ultimate tensile stress curve from tensile testing at 70, 1,500, 2,200, and 2,400°F of CMC after nickel diffusion processing (magenta line is an artifact from the modeling code)

The temperature dependent Young's Modulus for the diffused CMC between 71 and 2,400°F in Figure 46, shows that the modulus is constant between the range of 70 to 1,500°F. The distinct drop in the modulus at T>2,000°F is attributed to the softening of the free silicon in the matrix of the CMC. The overall modulus for the diffused CMC throughout the temperature range tested decreased due to the Ni bonding to the Si in the SiC matrix. The knockdown in the modulus of the Ni diffused CMC was higher at 2,400°F than at 70°F.

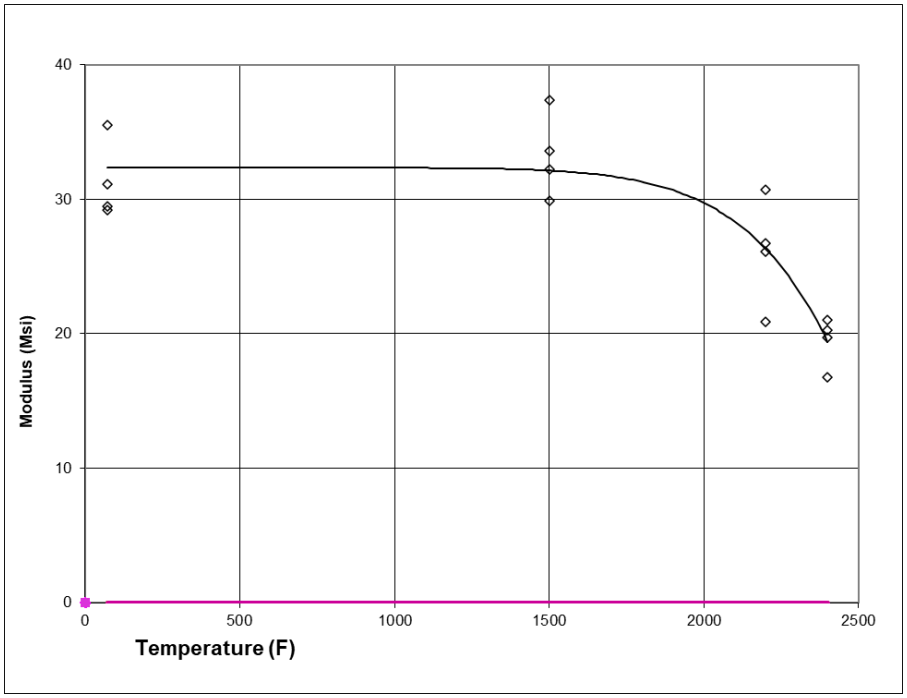

Figure 46: Graph of elastic modulus from tensile testing at 70, 1,500, 2,200, and 2,400°F of CMC after nickel diffusion processing. (magenta line is an artifact from the modeling code)

The proportionality limit (PL) graph for the diffused CMC in Figure 47 shows a larger scatter than normally seen in non-diffused CMC. The formation of the nickel silicide in SiC/Si matrix decreased the RT and the high temperature range of the testing (70-2,400°F). The proportionality limit within the CMC corresponds to the amount of stress required to initiate cracking. The decrease in the PL with the Ni_xSi_y within the SiC matrix, is theorized to be attributed to one of two processes. Either the generated matrix consisting of $SiC/Ni_xSi_y/Si$ is weaker than the SiC/Si matrix, or, the nickel silicide within the silicon carbide acts as a stress concentrator which induces matrix cracking at lower stresses than without nickel silicide inclusions. A lower PL within the diffused CMC will have a decrease in the durability compared to a non-diffused CMC.

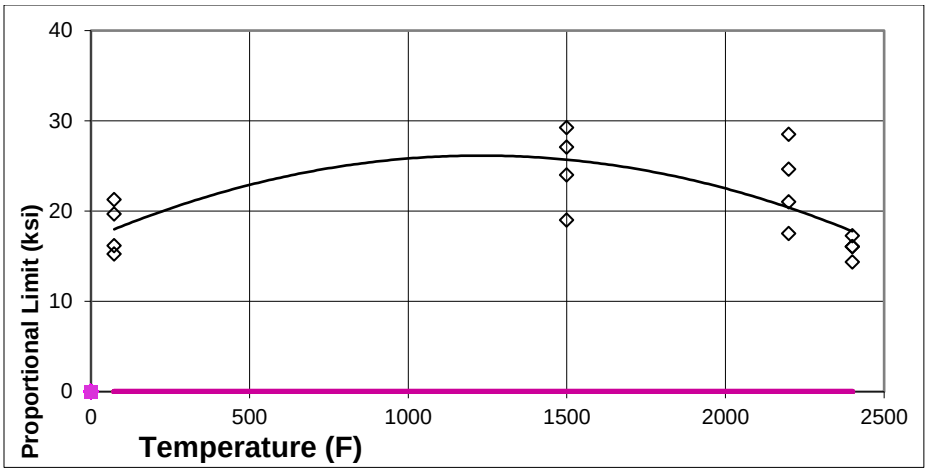

Figure 47: Graph of proportional limit from tensile testing at 70, 1,500, 2,200, and 2,400°F of CMC after nickel diffusion processing. (magenta line is an artifact from the modeling code)

Table 14: Short beam shear testing results at 70°F for Ni diffused CMC

Test #	Specimen ID	Average Width	Average Thickness	Peak Load	Shear Strength
		in	in	lbf	ksi
1	15590-SBS-1	0.251	0.0715	297	14.19
2	15591-SBS-2	0.2511	0.0722	297	14.05
3	15595-SBS-3	0.2511	0.0683	315	15.74
4	15596-SBS-4	0.2509	0.0679	210	10.55
5	15597-SBS-2	0.251	0.0703	189	9.19
6	15601-SBS-3	0.2514	0.0686	238	11.85
7	15881-SBS-1	0.2512	0.0731	323	15.06
8	15883-SBS-2	0.2514	0.0726	275	12.91
9	15885-SBS-3	0.2512	0.0729	269	12.58
10	15886-SBS-4	0.2507	0.0732	236	11.04
11	15888-SBS-2	0.2509	0.0732	192	8.96
12	15892-SBS-3	0.2506	0.074	290	13.4
Mean		0.251	0.0715	261	12.46
Std Dev		0.0002	0.0022	47	2.2
COV (%)		0.1	3.02	17.93	17.64

The data from the 4-point asymmetrical shear test at 70°F is listed in Table 14. The results are graphed in Figure 48. Examination of the test specimens revealed all tests failed in shear mode, not flex mode.

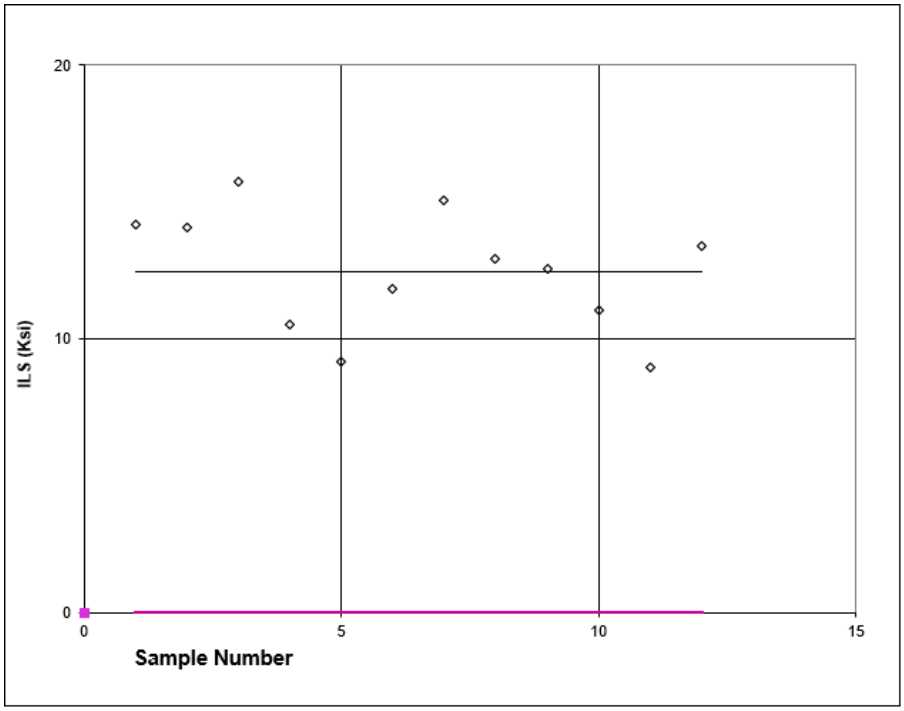

Figure 48: Average interlaminar shear strength at 70°F of individual tests of CMC after nickel diffusion processing. (magenta line is an artifact from the modeling code)

Table 15: High cycle fatigue test results of maximum Stress, maximum and minimum load and number of fatigue cycles to failure (Nf) of nickel diffused CMC tested at 1,500°F

Specimen ID	Specimen Width	Specimen Thickness	Max Stress	MAX Load	MIN Load	Frequency	Nf
	(in)	(in)	(ksi)	(Lbs)	(Lbs)	(Hz)	(count)
15596-TD2	0.4001	0.0679	33	898	45	30	540255
15596-TD3	0.4002	0.0685	30	822	41	30	694190
15595-TD4	0.4001	0.0692	34	942	47	30	1E+06
15590-TD1	0.4008	0.0716	30	861	43	30	117565
15591-TD2	0.4007	0.0727	35	1019	51	30	30216
15597-TD4	0.4005	0.0689	27	745	37	30	3E+07
15881-TD1	0.4006	0.0735	30	882	44	30	52065
15881-TD3	0.4008	0.073	32	938	47	30	152184
15883-TD4	0.4002	0.0717	27	775	39	30	3E+07
15883-TD5	0.3999	0.0718	31	890	44	30	204543
15884-TD3	0.4003	0.0732	28	820	41	30	307365
15884-TD4	0.4004	0.0742	32	950	48	30	25354
15892-TD1	0.4008	0.0745	32	957	48	30	151057
15892-TD2	0.4005	0.0739	29	858	43	30	3E+07
15888-TD4	0.400883	0.07383	32	947	47	30	94595
15888-TD5	0.40075	0.07354	29	856	43	30	888331

The data from the high cycle fatigue (HCF) test performed at 1,500°F is listed in Table 15 and Figure 49. The fatigue limit at 1,500°F is about 28 Ksi, which is similar to the average PL of diffused CMC at 1,500°F found during the static tensile test. This supports the theory that the diffused CMC with Ni_xSi_y is more likely to have matrix cracking compared to a CMC that does not.

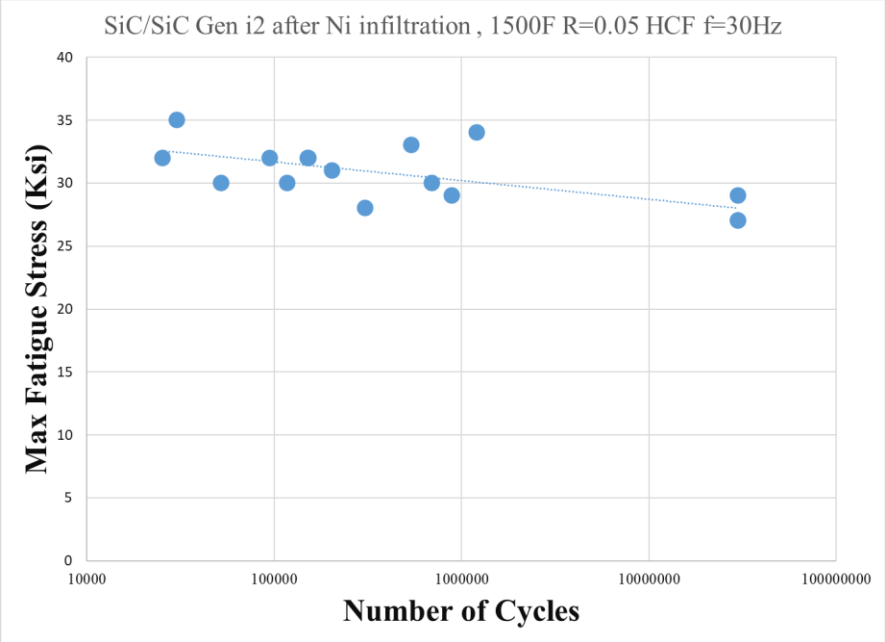

Figure 49: High cycle fatigue results maximum stress vs cycles to failure (Nf) of nickel diffused CMC tested at 1,500°F

4.3 EBC Advancement

4.3.1 High temperature steam exposure

TGO thickness was observed to increase appreciably within the time and temperature window framed by the experimental matrix defined in Table 5. Figure 50 demonstrates the "as-sprayed" TGO thickness and the typical TGO thickness observed after our most extreme test conditions.

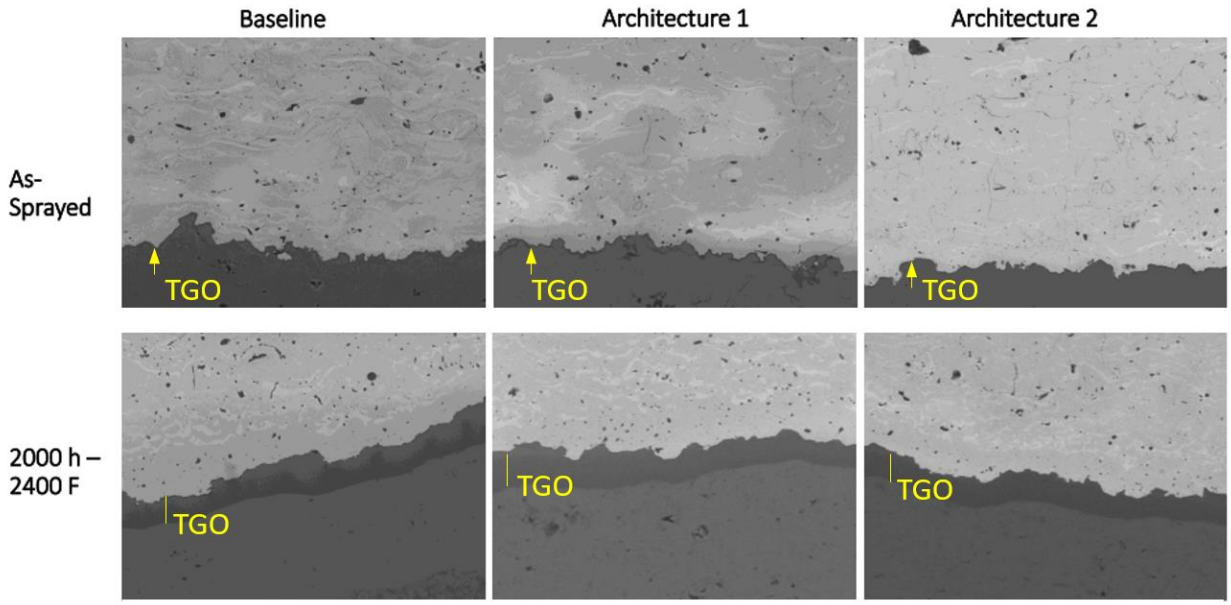

Figure 50: EBC architectures "as-sprayed" and after 2,000 hours at 2,400°F

The convoluted interface between Si and REDS layers leads to variable TGO thickness and measurement requires care. SEM micrographs (magnification 800x) were taken for each sample at 10 different locations along the sample cross-section at equal spacing. GE uses a semi-automated approach in which each of the 10 SEM micrographs are used to define the TGO thickness at 120 locations along the interface length, therefore 1200 measurements are used for the TGO thickness measurement per sample (Figure 51).

NASA uses an automated method (Figure 52) in which the TGO is selected by a machine learning model, and the TGO thickness at each pixel along the central ribbon length is measured. A neural network machine learning model is used to identify the TGO and cracks within the EBC micrograph. This neural network was trained on 100k microscopy images at NASA before training on the EBC task to achieve superior performance. Pixels on the edge of the detected TGO area are iteratively removed until only a center line remains. The direction of pixel removal is perpendicular to the center line. By tracking the number of pixels removed to get to the center line at each location, a radius is obtained at each location along the TGO center line. Multiply the radius by two to get the TGO thickness.

The same set of images was analyzed by NASA and GE, and NASA measurements are consistently ~5% less than GE measurements (Figure 53). The difference is thought to reflect the increased accuracy of determining the shortest distance between TGO boundary features with NASA's approach.

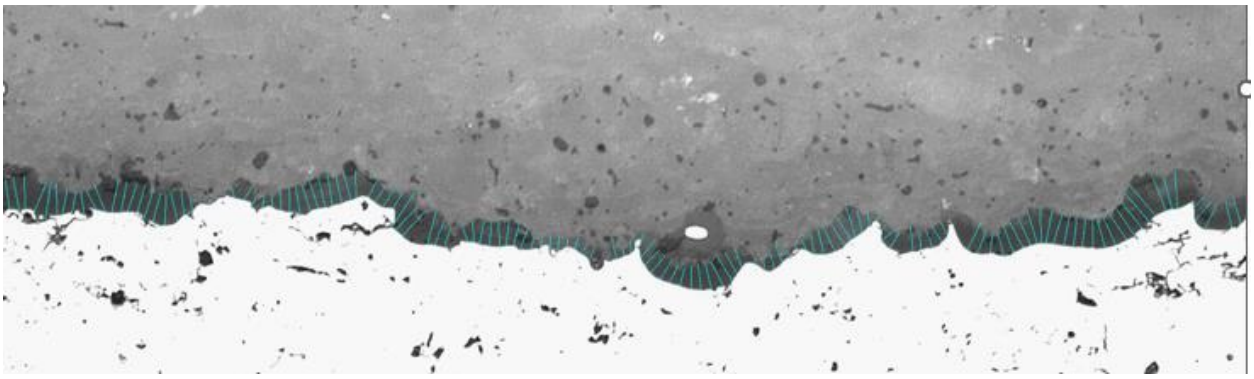

Figure 51: Representative 800x SEM image used in GE semi-automated TGO thickness measurement

SEM images (under a magnification of x800) were taken for each sample at 10 different locations from one end to the other end of sample cross-section at an equal spacing.
TGO layer were measured randomly at 120 locations from each SEM image using GEA semi-automated image analysis method that gives a total of 1,200 measurements per sample.

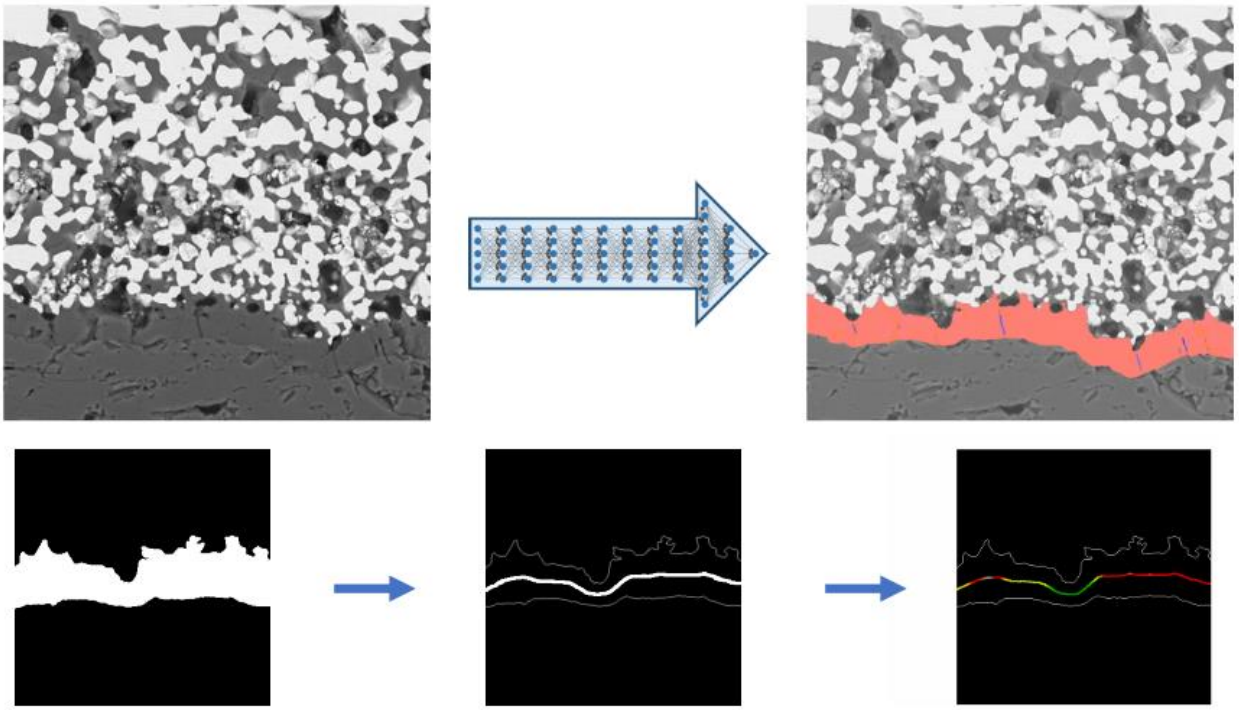

Figure 52: Automated image analysis sequence used at NASA for TGO thickness measurement

Top Panel: A neural network, a machine learning model, is used to identify the TGO and cracks within the EBC micrograph. This neural network was trained on 100k microscopy images at NASA before training on the EBC task to achieve superior performance. Bottom panel: Pixels on the edge of the "detected TGO area" are iteratively removed until only a center line remains. The direction of pixel removal is perpendicular to the center line. By tracking the number of pixels removed to get to the center line at each location, a radius is calculated at each location along the TGO center line. Multiply the radius by two to get the TGO thickness.

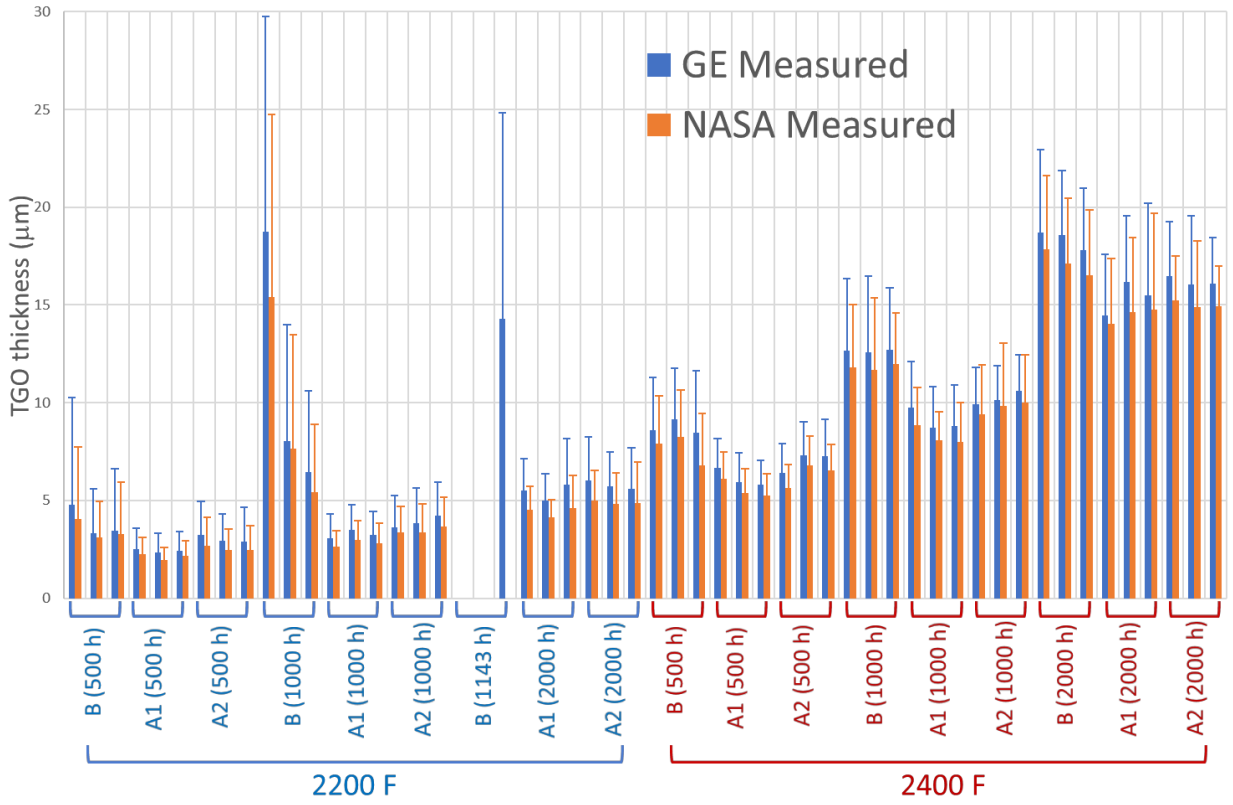

Figure 53: TGO thickness measurements by GE and NASA compared

In Figure 53, note that all three Baseline samples failed after 1,143 h at 2,200°F. There was water dripping because H_2O did not fully vaporize due to a test setup malfunction. Arch.1 and 2 samples tested alongside the Baseline samples were not affected. Neither NASA nor GE thought it was beneficial to repeat the experiment. Note also that one Baseline sample at 1,000 h in 2,200 °F shows 15-20 micron TGO thickness in Figure 53 an artefact from the set of 10 SEM images along the sample length containing a partial coating spallation. This sample was omitted from the box plot in Figure 54, thus only two Baseline samples from 1,000 h at 2,200 °F are represented. The remaining box plots in Figure 54 represent three mean TGO thicknesses and three values for standard deviation, each generated from the series of 10 SEM images which describe each of three samples per condition.

Architectures 1 & 2 are both observed to perform better than the Baseline. Oxidation rates ranking (low to high): Arch 1 < Arch 2 < Baseline (Figure 54 and Figure 55).

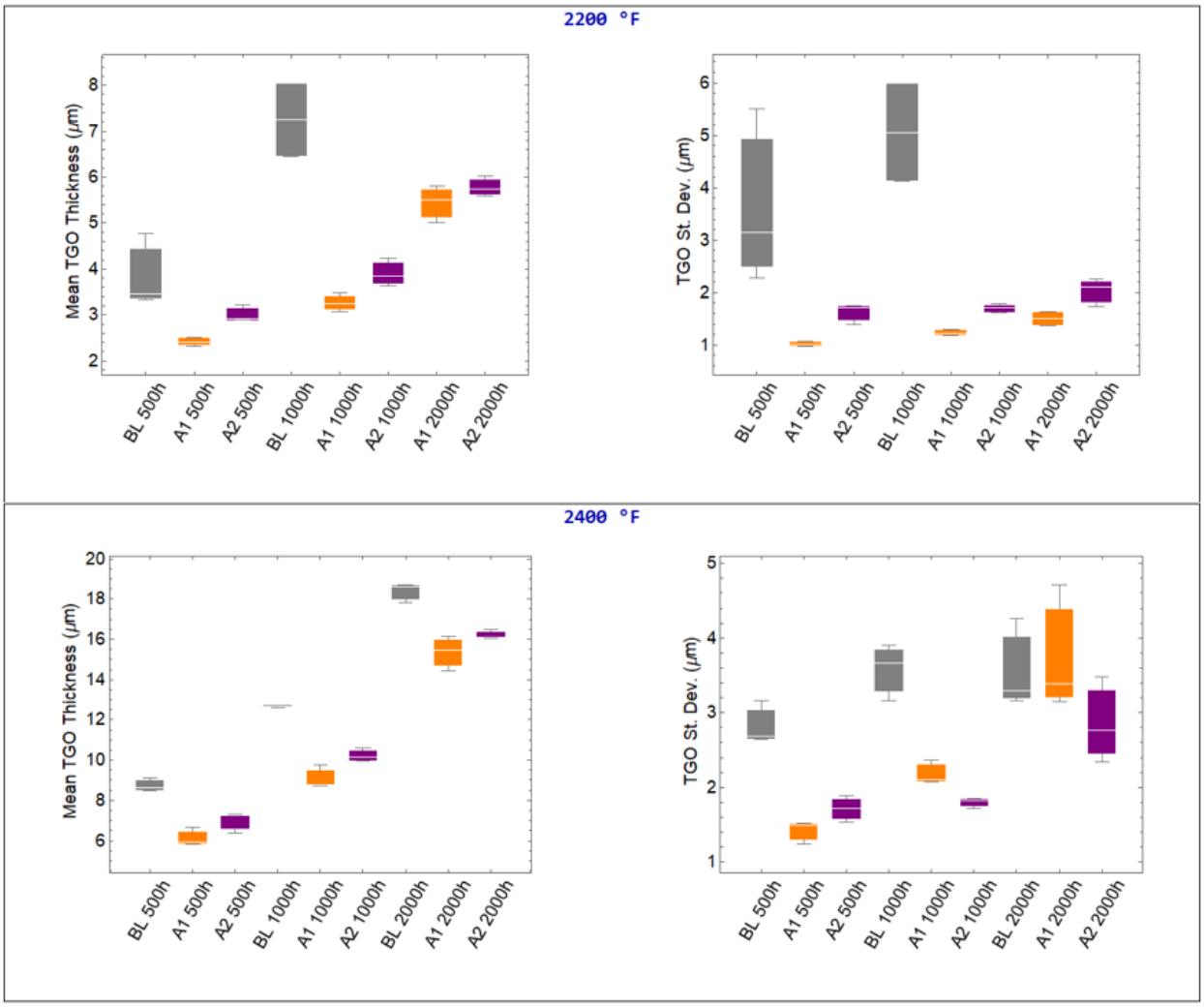

Figure 54: Mean TGO thickness and standard deviation of measurement for isothermal steam testing at 2200°F and 2400°F. Thickness measurements are from the GE method.

Fitting the experimental data points (Figure 55) to the linear-parabolic equation (Equation 1) yields the values for B and A (Equation 2 & Equation 4) for each architecture, which leads to an estimate of the permeability of water in the coatings. Linear-parabolic equation parameters and estimated permeability are reported in

Table 16, along with those from literature and previous development & testing at NASA-GRC (Glenn Research Center). Additional context and details of data treatment can be found in *Sullivan et al., NASA TM-20220016363, January 2023.* GE Arch. 1 & 2 show the lowest observed permeability of the set.

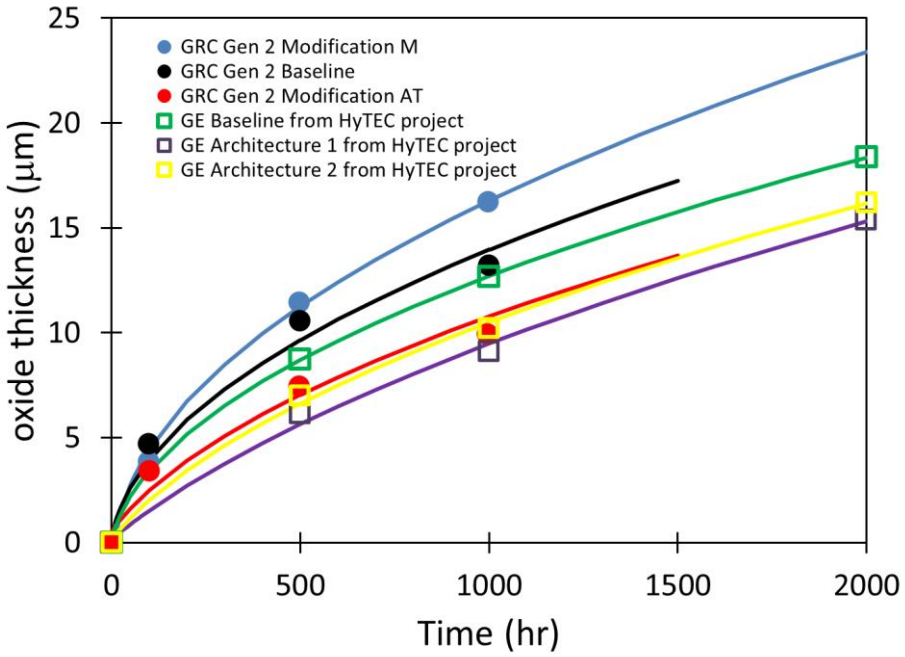

Figure 55: Linear-parabolic fits of several EBC architectures, including those tested under this project at 2,400°F. Arch. 1 shows the slowest TGO growth.

Table 16: Fitting the TGO thickness measurements to the linear-parabolic equation yields the values for A and B, which leads to an estimate of the permeability of water in the coatings

**Lee K., J. Am. Ceram. Soc. 102 (3) 1507-1521 (2018). *Sullivan et al., NASA TM-20220016363, January 2023*

Coating system	$B\left(\frac{\mu m^2}{hr}\right)$	$A\ (\mu m)$	$\delta(\mu m)$	**Permeability (moles/(cm-atm-sec))**
GE Arch 1	0.2362	15.723	356	1.23e-12
GE Arch 2	0.1998	8.632	305	1.63e-12
GRC Gen 2 Modified (AT)	0.18	6.296	254	1.68e-12
Univ Bordeaux YDS .8 mm	1.13	33.879	500	6.98e-12
GE Baseline	0.1879	2.118	356	7.28e-12
GRC Gen 2 Baseline	0.2167	1.6	254	7.94e-12
GRC Gen 2 Modified (M)	0.2928	1.5058	254	1.14e-11
Univ Bordeaux YDS 3 mm	1.31	22.811	500	1.19e-11
Univ Bordeaux YMS .8 mm	1.18	14.382	500	1.70e-11
Stony Brook YbDS	0.1082	0.2407	180	1.87e-11

4.3.2 High heat flux laser testing without CMAS

All three architectures survived Thermal Gradient 1 and 2 test conditions (500 and 1,000 cycles). There was no sign of coating distress for any of the three architectures in either thermal gradient (Figure 56 and Figure 57). Overheating of the fixture material (steel) led to ablation and subsequent deposition on the EBC surface for some early tests under thermal gradient 2 (Figure 57). Replacement of the fixture material with nickel-based superalloy eliminated the problem.

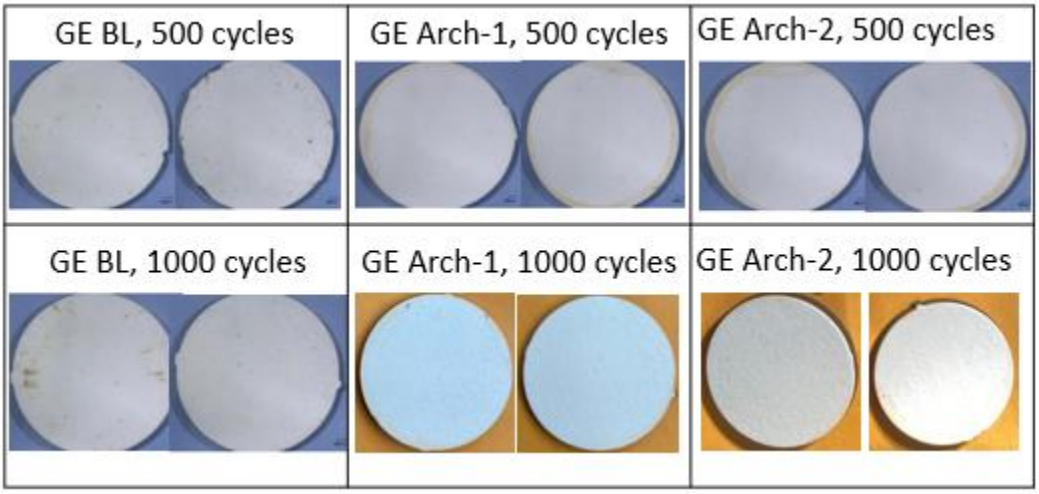

Figure 56: Samples after cyclic exposure to Thermal Gradient 1 (~2,600°F front, 2,100°F back) No coating damage observed.

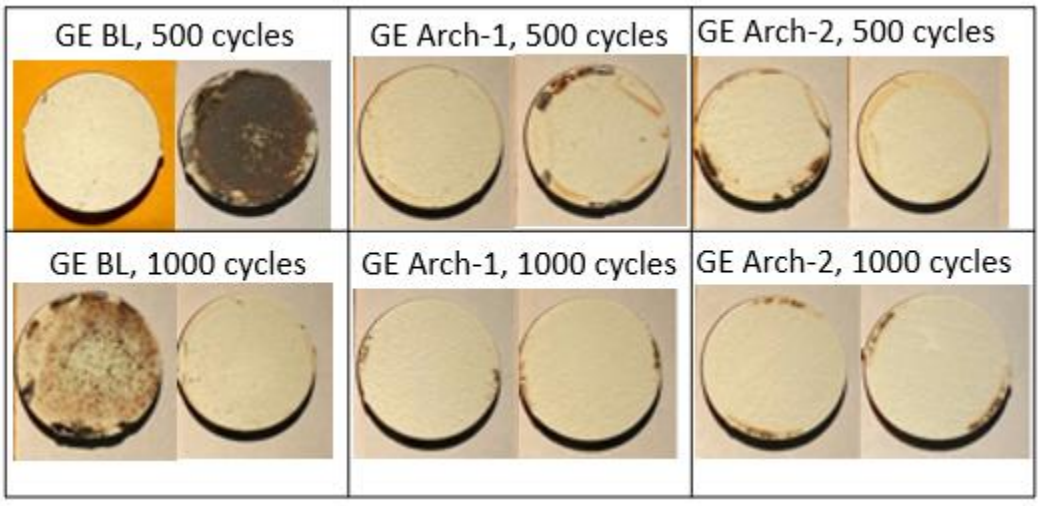

Figure 57: Samples after cyclic exposure to Thermal Gradient 2 (~2,600°F front, 1,900°F back)

No coating damage was observed, though some metal deposition was noted from overheating the fixture and ablating the fixture material.

4.3.3 High heat flux laser testing with CMAS

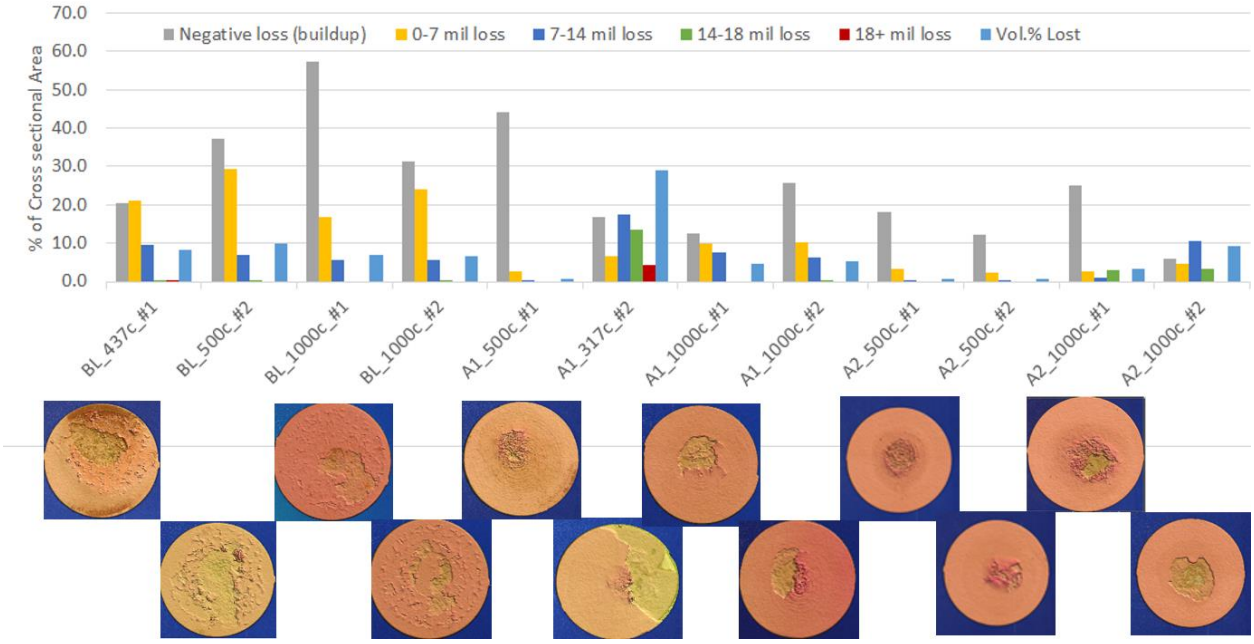

Figure 58: Percentage of EBC surface area lost to various depths after thermal gradient test condition 1 with CMAS (~2,600°F EBC surface and ~2,100°F CMC back). 6 min heating/cooling cycle count indicated.

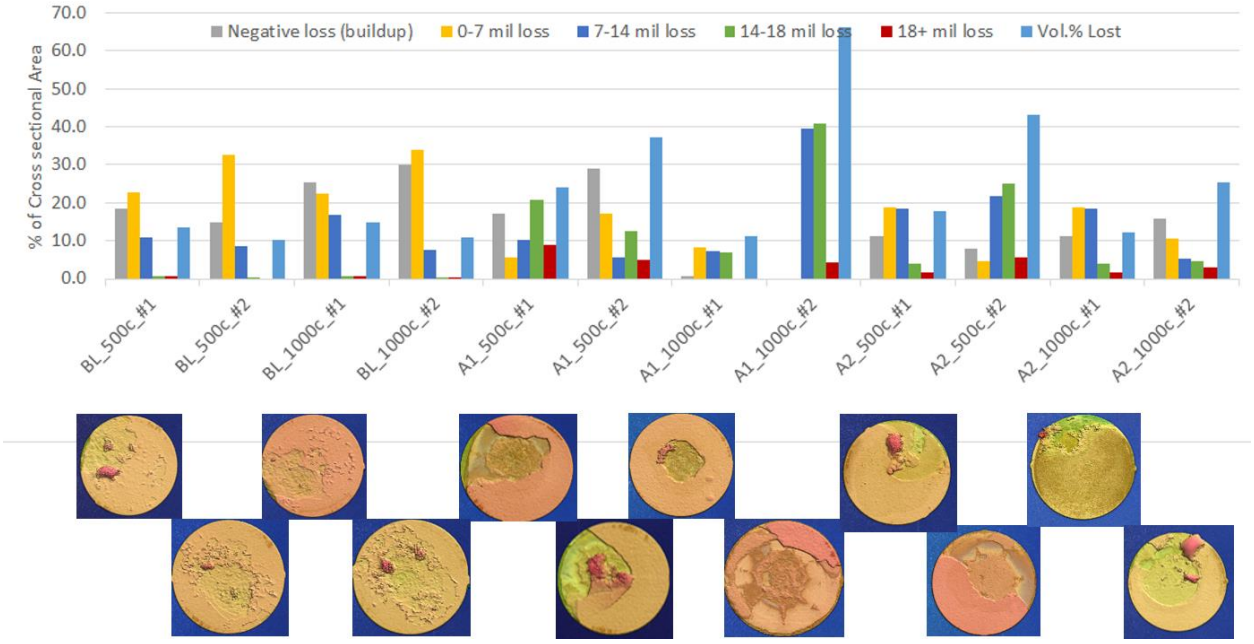

Figure 59: Percentage of EBC surface area lost to various depths after thermal gradient test condition 2 with CMAS (~2,600°F EBC surface and ~1,900°F CMC back). 6 min heating/cooling cycle count indicated.

EBC loss to various depths is presented in Figure 58 and Figure 59 and as percentage of surface area when exposed to thermal gradient test conditions 1 & 2 (TG1 & TG2) with CMAS, respectively. "Vol.% Lost" considers the sum of coating lost within each thickness bin (0-7 mil, 7-14 mil, 18+ mil), and therefore it is the best single descriptor of EBC spallation. The sample images are centered below their respective descriptions.

When comparing Vol. % Lost for Arch. 1 & 2 against BL tested to 1,000 cycles in TG1 and TG2, statistical difference cannot be established between populations by T-test (Table 17). If the probability $p(\mu_i = \mu_{BL})$ were less than 5% of observing these values with equivalent population means we would have rejected the null hypothesis that the mean sample populations are equivalent. Therefore, architectures are not differentiated by this test in the overall performance matrix (Table 18).

Table 17: EBC volume lost from thermal gradient test conditions 1&2 (TG1 & TG2) with CMAS to 1000 cycles. No statistical difference was observed between architectures with a threshold of 5% probability for TG1 or TG2.

	Vol.% Lost at 1000 cycles		Mean	$p(\mu_i = \mu_{BL})$
TG1				
BL	6.9	6.7	6.8	
Arch. 1	4.4	5.3	4.9	0.0516
Arch. 2	3.4	9.2	6.3	0.6702
TG2				
BL	14.9	10.8	12.85	
Arch. 1	11.3	66	38.65	0.45
Arch. 2	12.26	25.3	18.78	0.48

4.3.4 High temperature solid particle erosion

Test samples at all conditions exhibited similar behavior as shown in Figure 60. Cumulative mass loss vs. cumulative erodent curves for Arch-1 and Arch-2 are fairly linear. Arch. 0 (Baseline) has higher degree of non-linearity (higher rate of mass loss in the beginning) suggesting the REMS layer is less erosion resistant than REDS layer.

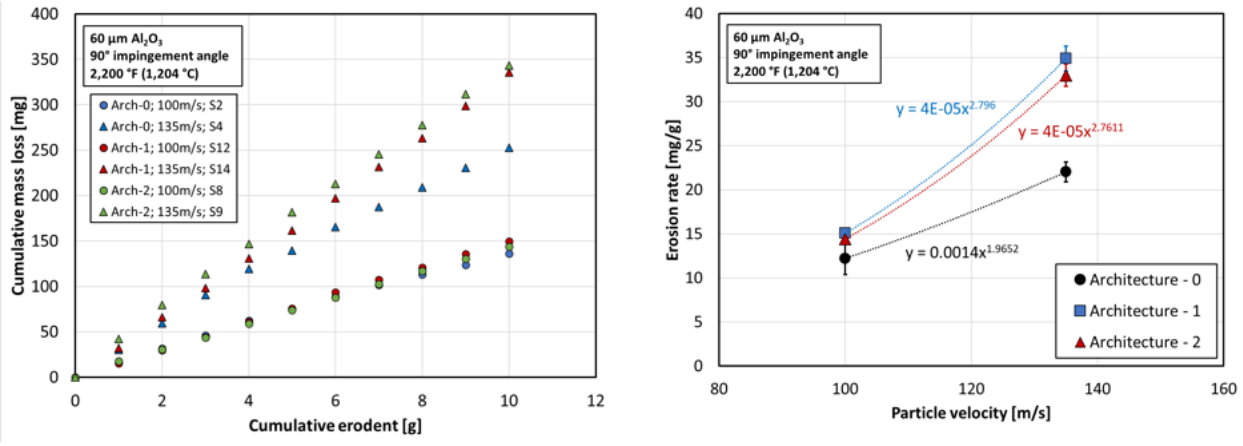

Figure 60: Left: cumulative mass loss vs. cumulative erodent. Right: steady-state erosion rate is calculated from the last 6 data points of the plot on left.

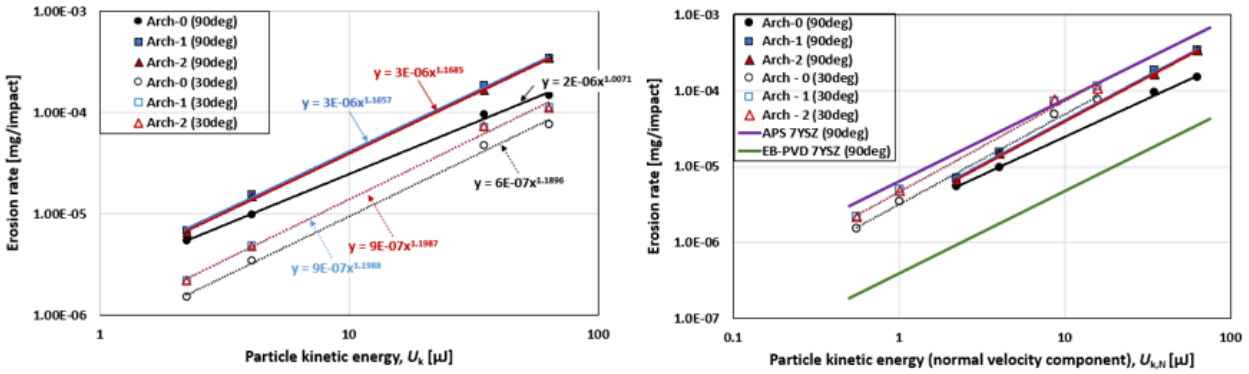

Figure 61: Steady state erosion rates of EBC architectures

Left: Steady state erosion rates vs. particle kinetic energy of GE architectures tested with Al_2O_3 erodent at 90°- and 30°- incidence at 2,200°F (1,204°C).

*Right: Steady state erosion rates vs. normal component of particle kinetic energy for GE architectures tested with Al_2O_3 erodent at 90° and 30° incidence at 2,200°F (1,204°C). APS and EB-PVD 7YSZ coatings are included for context. * Presby, M. et al., Coatings 13 (2023) and *Presby, M. et al, J. Am. Ceram. Soc. (2023)*

Arch. 0 (Baseline) shows the greatest erosion resistance for *90° and 30°* incidence, and Arch-1 and -2 appear to be comparable (Figure 61). 30° erosion data is displaced upward from 90° data when plotted as a function of the kinetic energy of the normal component of particle velocity, indicating that the surface-parallel velocity component also contributes to the erosion process. *(*Figure 61 *right, see Presby et. al. NASA/TM-20230003935 for more detail).* The erosion rates for all three EBC architectures are below or equivalent to those of APS 7YSZ TBC used on metallic liners. Since TBC erosion rates are not life-limiting for our metal liners, we conclude that all EBC architectures meet durability requirements, and the magnitude of difference is not appreciable for the application.

5. Assessment Against TPMs and KPPs

As previously stated, the objective of the HyTEC – Combustor Technology project is to develop technology for a compact, low emissions, rich-burn combustor that maintains a high-level of durability. Relative to the HyTEC technical measurements, the focus of this effort is on Key Performance Parameter – 4 (KPP-4). The goal of this KPP is to improve the durability of the combustor by 5% beyond the current state of the art (SOA) with a minimum goal of being equivalent to the current SOA.

Beyond KPP-4, a review of KPP-1 was completed. Using the calculated weight reduction, an assessment was completed to show that a ~.015% improvement in fuel burn is achieved. Furthermore, the CMC dome results in an opportunity to repurpose cooling flow if desired. However, this repurposing would be at the detriment of durability. An initial assessment of this repurposing showed a potential fuel burn savings of .25% maximum but would result in a durability reduction in multiple hot gas components outside the CDN. Therefore, this fuel burn benefit can not be accounted for at this time.

To validate the durability improvement, a collection of technical performance measures (TPM) was developed for each individual focus area as described below.

5.1 Swirler Attachment TPM Assessment

5.1.1 Threaded Design TPM Assessment

In a clamped design, the joint holding the swirler assembly must be sufficient to overcome the aerodynamic torque of the swirler and prevent slipping while withstanding the vibrational loads due to P4' dynamics. To put this requirement in a measurable deliverable, a minimum clamp load at cold condition is required. This clamp load was determined to be 500lbs; Therefore, the TPM is as follows:

- After experiencing 10^7 cycles of P4' dynamics in TCA and accounting for HTP rig cycle conditions, clamped swirler retains >500lbs of clamp load at room temperature (70°F).

During assembly, the parts were torqued to a target clamp load following the design intent as described in section 3.1.4. To calibrate the torque-tension relationship, strain gauges were used during assembly.

In order to evaluate the remaining clamp load after testing, a slip test was conducted with the results documented in Table 8 in Section 1.1.1. The parts were also retorqued to the target torque at new make based on the new make torque-tension relationship and the slip test conducted to measure the slip value for the target torque condition. This allows to use the slip values measured in the table to assess the clamp load on the joints after testing.

For the G02 design, which is the prime bolted joint configuration being considered, the slip value measured after all testing was 50% less than at new make. Since the friction coefficient is constant (same parts) then the decrease in slip value is due to loss of clamp load on the joint during testing. The reduction in slip value after testing is almost 50%. These results indicate a drop in the cold clamp load from the design clamp at new make to <500lbs after testing. This is below the goal of 500lbs in the TPM.

5.1.2 Pressure Loaded TPM Assessment

In a pressure loaded design, the loads and stress field are less critical than a threaded (clamped) design approach. For the design being assessed here, the primary failure mechanism is wear. This determination is based on experience in legacy combustor designs where components are similarly constrained against

the combustor. For the purposes of this design, there are two different wear concerns that require assessment.

The first area of concern is the axial interface between the swirler assembly and CMC dome. This interface is critical aerodynamically as it can impact the position of the fuel nozzle and swirler relative to each other. If this relative position is outside of an acceptable range, it can cause a number of different performance issues such as fuel mixing and auto-ignition. To put this particular concern in a measurable deliverable, a limit on the amount of wear must be set. This wear limit was determined, using data from current state of the art designs, based on the amount of fuel nozzle recession that can be allowed prior to the initiation of an auto-ignition risk. To comply with export requirements the requirement and results are provided as a non-dimensional percentage. Therefore, the TPM is as follows:

- After experiencing 10^7 cycles of P4' dynamics in TCA and max test point in HTP rig combined measured wear in flare and CMC dome at their interface to have a goal of less than 77% of the set required maximum wear.

Table 9, in section 4.1.5 of the report, documents the measured wear on the interfaces of all the configurations. After completion of testing the G01 configuration, the wear on the swirler to dome interface was measured to be under 77% of the requirement, with the CMC wear contributing less than 38% and the metallic swirler less than 38%. The amount of wear meets the TPM goal of wear under 77% of the requirement for the interface.

The second area of concern is the interface between the swirler and the flare that is intended to restrict the ability of the swirler to rotate. This feature is typically labelled as the anti-rotation feature. The anti-rotation feature is critical to the aerodynamic performance of the combustor as it allows the swirler to spin the air at the point of fuel injection to ensure proper fuel/air mixing. To put this particular concern in a measurable deliverable, a limit on the amount of wear must be set. This wear limit was determined based on comparison to successful legacy experience. Therefore, the TPM is as follows:

- After experiencing 10^7 cycles of P4' dynamics in TCA and max test point in HTP rig combined measured wear in anti-rotation tabs in flare have a goal of less than .005".

Table 9, in section 4.1.5 of the report, documents the measured wear on the interfaces of all configurations. After completion of testing the G01 configuration, the wear on the anti-rotation tab and the matching feature in the swirler was under 0.005". This meets the goal of wear under 0.005".

5.2 Nickel Diffusion TPM Assessment

As previously discussed, the diffusion of nickel into CMC material will have an adverse reaction on the durability of the component. To understand this impact, a prediction of the loss in material properties is required after an amount of nickel diffusion occurs that is equivalent to a full hardware lifetime. However, the design of the hardware can be modified to account for this effect. The design can be modified to lower the rate of nickel diffusion and/or it can be designed to withstand the durability reduction and still meet durability requirements. Ultimately, the goal is to ensure that the effects of nickel diffusion are accounted for within the design effort. Therefore, the TPM is as follows:

- While including diffusion effects on the durability, the swirler to CMC attachment design must not be the analytical life limiting feature of the combustor.

To determine the local durability impact, a few items are needed. The temperature predicted at the nickel to CMC interface can be found using the thermocouple data from HTP rig testing at engine cycle

representative conditions. The time spent at those temperatures can be found using cycle times representative of narrow body commercial engine operation for the typical life of a combustor. Using this information in combination with the nickel diffusion model discussed in section 4.2.1, the G01 configuration results in NiSi diffusion of up to 0.35 mils (0.00035 inches) into the CMC. In comparison, the proposed design, along with the CMC material property samples are roughly 70-80 mils thick (0.07-0.08 inches). Therefore, less than 1% of the material thickness will be subjected to nickel diffusion. For the G02 configuration, the Ni_xSi_y diffusion is up to 5 mils (0.005 inches) into the CMC (up to 7% of the material thickness).

Material testing of CMC samples with nickel diffusion throughout the thickness measured a reduction to material properties in the CMC material. Preliminary analysis on a proposed design for the CMC dome architecture calculates the stresses near the swirler interface with the CMC are in the order of 50% lower than the limiting stress location on the main face of the dome. Therefore, a reduction in material properties less than 50% due to diffusion at the swirler to CMC interface would not cause a change to the life limiting location of the dome. This is true of both the G01 and the G02 configurations.

5.3 EBC Advancement TPM Assessment

The durability of the EBC coating is critical to all CMC components. And with the extensive use of CMC within this combustor design, it plays a pivotal role in the overall durability. As is the case with many technologies, the coating has multiple failure mechanisms. Extensive lab-based testing was conducted to assess each mechanism, with the key performance parameter (KPP) listed in Figure 62.

EBC Coupon Test	KPP
Steam Testing	TGO thickness
Thermal Gradient Testing	Degree of spallation and coating damage
CMAS + Thermal Gradient	CMAS infiltration within EBC and degree of spallation
High Temperature Testing	Erosion rate

Figure 62: KPP per EBC coupon testing type

The goal of this effort is to improve upon the current state of the art and increase the overall durability of the coating system for the given application. Therefore, the TPM is as follows:

- The overall durability of the EBC/CMC system must be equivalent or 5% better than the SOA coating system when accounting for comparative coupon testing results.

To quantify and rank total EBC performance, a matrix was developed to reflect the weighted importance (9, 3, 1) of each test modality to field durability, and the score (9, 3, 1) of each EBC architecture at the most rigorous test durations (Table 18). Weighted importance was assigned to reflect the damage mode potential impact to early life (9), mid/late-life (3), and late life (1). Arch. 1 and Arch. 2 both show considerable improvement over the baseline, namely in steam performance which is a primary indicator of EBC and component health. Therefore, both Arch. 1 and Arch. 2 meet the KPP-4 criteria with improvement above the baseline EBC performance of 67% and 17%, respectively.

Table 18: Performance matrix incorporates the relative importance of each test modality to the EBC durability for liner application.

		Performance Score			Weighted Scores		
Assessment	Importance	A0	A1	A2	A0	A1	A2
Clean Thermal Gradient 1 (1,000c)	9	9	9	9	81	81	81
Clean Thermal Gradient 2 (1,000c)	9	9	9	9	81	81	81
Steam Test (2,200°F/1,000h)	9	1	9	3	9	81	27
Steam Test (2,400°F/2,000h)	9	1	9	3	9	81	27
CMAS 1 (1,000c)	3	3	3	3	9	9	9
CMAS 2 (1,000c)	3	3	3	3	9	9	9
Erosion (30°)	1	9	9	9	9	9	9
Erosion (90°)	1	9	9	9	9	9	9
Total					216	360	252
Improvement (%)						67	17

6. Conclusions / Technology Readiness Assessment

6.1 Swirler Attachment

All three configurations tested in the TCA and HTP rigs successfully completed their dwell periods with all hardware found in serviceable condition.

Post test inspection found that the G03 configuration had lost most of its clamp load after the rig testing campaign with evidence of some swirler rotation after the test. This configuration was used as a baseline since rig testing on the original rotorcraft sized combustor saw some of the swirlers loosen after testing. Therefore, this testing provided confirmation that the G03 design approach results in clamp loss and swirler rotation that is not desirable. Due to this, the G03 configuration is no longer being pursued.

Both the G01 and G02 did better than the benchmark of the G03, there is no indication of swirler movement and in the case of the G02 better preservation of clamp load on the bolted joint was measured. In addition to the joint evaluation after rig testing as stated in the TPM, a duplicate set of hardware was run through a furnace test as described in Section 1.1.1, the results are also tabulated in Table 8. After extended hot time in the furnace (simulating 10,000 engine cycles) the G02 design showed a drop in clamp load, as evaluated in the slip test, of 84%. Those results indicate a drop in cold clamp load from the design clamp to 16% of the design clamp. Both the rig and furnace testing showed a greater drop in clamp load from hot time on the joint than desired. Further improvements on the G02 design could be explored, such as increasing the new make torque value to increase cold clamp load, using the margin available on the material with the current design, exploring the use of a different material with a larger thermal growth expansion coefficient, or adjusting the swirler geometry to allow for torque to be applied aft of the swirler vanes so as to not be limited by yielding limit on the swirler vanes.

The G01 configuration excelled in terms of wear. Since it did not rely on a bolted joint, it was not susceptible to relaxation of loosening of the joint due to combustor vibration. The design also benefited from having its CMC/Metal interface on the forward side of the dome, allowing for cooler temperatures at the interface and reduced the amount of diffusion between the metallic flare and CMC dome. There was minimal wear measured in the interfaces even when subjected to 10^7 cycles in the TCA.

Testing on the G01 configuration matched cycle conditions that would be experienced in a state-of-the-art commercial jet engine, the materials, construction, interfaces and boundary conditions were all the same as what a swirler/flare configuration would see in an engine. After expert review, the mechanical attachment method of the swirler for the G01 configuration was found to meet the requirements of Technology Readiness Level (TRL) 4. This achievement was based on assembling the hardware without complication, withstanding aerodynamic torque after sustained time at take-off power, successfully withstanding P4 dynamic pressure excitation for sustained periods of time, and an ability to retain all hardware at shutdown.

Given that only the G01 configuration met its TPM requirements and achieved TRL4 status, the G01 configuration will be downselected as the design approach moving forward in future combustor demonstrations.

6.2 Nickel Diffusion

The diffusion model generated predicts the progression of the penetration depth with time for both alloys at 1,800°F well. The same diffusion model was checked against the different diffusion tests ran against two alloys, N5 and Inconel 600, 63.45 and 76.83 wt.% Ni, respectively. The twelve tests used in the model check were run at 1,700°F twice for each time period of 50, 100, and 200 hours. The only notable difference between the experiments with the different Ni content in the alloy was the equilibrium Nickel concentration

at the CMC interface with the alloy of 35% for the N5 and 45% for the Inconel 600. The diffusivity calculations for Ni into the CMC as a function of temperature, nickel concentration, and time were developed. The nickel diffusion depth into the CMC combustor dome utilizing a typical narrowbody life cycle requirement and the HTP temperatures measured at the flare interface was calculated for G01 and G02 at 0.35 and 5.0 mils, respectively.

UTS, PL, Young's modulus, shear, and HCF mechanical properties were determined by testing for nickel diffused CMC with Ni wt.% between 10 and 12% in the center of the test specimen. Based on these results, a small reduction in the local material capability will exist for both the G01 and G02 configurations. However, early analysis of the CMC dome design shows that the dome can withstand up to a 50% reduction in the local properties near the swirler interface. Since the material property reduction at full diffusion is less than 50%, this will not result in a reduction in the overall durability of the hardware. Although both the G01 and G02 designs meet the TPM requirement, the G01 design results in a higher capability and is the preferred design from a nickel diffusion perspective.

6.3 EBC Advancement

The following conclusions can be made by the EBC testing conducted under this project:

- Steam testing: Arch. 1 & Arch. 2 performed better than the baseline in all conditions and durations.
- Laser thermal gradient 1 & 2 without CMAS: no coating degradation was observed for all conditions and durations.
- Laser thermal gradient condition 1 & 2 with CMAS: no statistical difference for volume of coating lost was determined between Arch. 1 and Arch. 2 when compared against the baseline architecture.
- Erosion Testing: The baseline architecture showed slightly higher erosion resistance over Arch. 1 and Arch. 2. However, all EBC architectures showed less erosion than APS 7YSZ TBC, indicating that relative performance difference is not appreciable for the application because erosion is not a primary degradation mode for TBC-coated metallic liners.

TRL-4 definition: "Component and/ or breadboard validation in laboratory environment." Project success for laboratory testing is measured against KPP-4: "Meets SOA of baseline" for Min. success, and "Exceeds SOA by 5%" for full success.

- Table 18 indicates that Arch. 1 and Arch. 2 both meet the KPP full success criteria by exceeding performance of the Baseline coating by 67% and 17%, respectively.

TRL-5 definition: "Component and/ or breadboard validation in relevant environment." The TCA and HTP rig tests provided the multi-variate conditions of combined thermal gradient, pressure, vibration, and steam exposure that can be expected in engine operation.

- Our prior experience with Arch. 1 allowed us to predict the increased performance over the baseline and pre-select this coating for the dome/swirler assemblies tested in engine-simulative environments under this project by HTP and TCA rig exposure. All of the EBC-coated surfaces survived the testing without spallation or visual indication of degradation (Figure 34, Figure 35, Figure 36), demonstrating TRL-5 material capability.

Additional TRL maturation/ demonstration of Arch-1 EBC will be tied to the liner component through testing in the FAR and the demonstrator core.

7. Appendix

7.1 Nickel Diffusion

Table 19: Isostatic diffusion data generated and utilized in the nickel diffusion model

TEST #	material 1	Ni %	Specimen ID	Ceramic material	Specimen ID2	Temp (F)	Stress (ksi)	Time (hours)	Additional measurements
ISTAT-2022-001	N5-	63.45	69X31A	CMC matrix	14656-1	1500	5	100	XRD
ISTAT-2022-002	N5-	63.45	69X32	CMC matrix	14656-2	1600	5	100	XRD
ISTAT-2022-003	N5-	63.45	69X30	CMC matrix	14656-3	1700	5	100	XRD
ISTAT-2022-004	N5-	63.45	64N05	CMC matrix	14656-4	1750	1.5	50	XRD
ISTAT-2022-005	N5-	63.45	64N06	CMC matrix	14656-5	1775	1.5	50	XRD
ISTAT-2022-009	Inconel 600	76.83	3SK01	CMC matrix	14656-13	1800	1.5	25	microprobe
ISTAT-2022-010	Inconel 600	76.83	3SK02	CMC matrix	14656-14	1800	1.5	50	microprobe
ISTAT-2022-011	Inconel 600	76.83	3SK03	CMC matrix	14656-15	1800	1.5	75	microprobe
ISTAT-2022-012	Inconel 600	76.83	3SK04	CMC matrix	14656-16	1700	1.5	50	EDX
ISTAT-2022-013	Inconel 600	76.83	3SK05	CMC matrix	14656-17	1700	1.5	100	EDX
ISTAT-2022-014	Inconel 600	76.83	3SK06	CMC matrix	14656-18	1700	1.5	200	EDX
ISTAT-2022-015	Inconel 600	76.83	3SK07	CMC matrix	14656-19	1600	1.5	50	
ISTAT-2022-016	Inconel 600	76.83	3SK08	CMC matrix	14656-20	1600	1.5	100	
ISTAT-2022-017	Inconel 600	76.83	3SK09	CMC matrix	14656-21	1600	1.5	200	
ISTAT-2022-018	N5-	63.45	3SI01	CMC matrix	14656-22	1800	1.5	25	
ISTAT-2022-019	N5-	63.45	3SI02	CMC matrix	14656-23	1800	1.5	50	microprobe and EDX
ISTAT-2022-020	N5-	63.45	3SI03	CMC matrix	14656-24	1800	1.5	75	microprobe and EDX
ISTAT-2022-021	N5-	63.45	3SI04	CMC matrix	14656-25	1700	1.5	50	EDX
ISTAT-2022-022	N5-	63.45	3SI05	CMC matrix	14656-26	1700	1.5	100	EDX
ISTAT-2022-023	N5-	63.45	3SI06	CMC matrix	14656-27	1700	1.5	200	EDX
ISTAT-2022-024	N5-	63.45	3SI07	CMC matrix	14656-28	1600	1.5	50	
ISTAT-2022-025	N5-	63.45	3SI08	CMC matrix	14656-29	1600	1.5	100	
ISTAT-2022-026	N5-	63.45	3SI09	CMC matrix	14656-30	1600	1.5	200	
ISTAT-2022-027	Hast X	48.1	3SJ01	CMC matrix	14656-31	1800	1.5	25	
ISTAT-2022-028	Hast X	48.1	3SJ02	CMC matrix	14656-32	1800	1.5	50	
ISTAT-2022-029	Hast X	48.1	3SJ03	CMC matrix	14656-33	1800	1.5	75	

TEST #	material 1	Ni %	Specimen ID	Ceramic material	Specimen ID2	Temp (F)	Stress (ksi)	Time (hours)	Additional measurements
ISTAT-2022-030	Hast X	48.1	3SJ04	CMC matrix	14656-34	1700	1.5	50	
ISTAT-2022-031	Hast X	48.1	3SJ05	CMC matrix	14656-35	1700	1.5	100	
ISTAT-2022-032	Hast X	48.1	3SJ06	CMC matrix	14656-36	1700	1.5	200	
ISTAT-2022-033	Hast X	48.1	3SJ07	CMC matrix	14656-37	1600	1.5	50	
ISTAT-2022-034	Hast X	48.1	3SJ08	CMC matrix	14656-38	1600	1.5	100	
ISTAT-2022-035	Hast X	48.1	3SJ09	CMC matrix	14656-39	1600	1.5	200	
ISTAT-2022-036	Inconel 600	76.83	3SK10	CMC matrix	14656-40	1800	1.5	25	
ISTAT-2022-037	Inconel 600	76.83	3SK11	CMC matrix	14656-41	1800	1.5	50	
ISTAT-2022-038	Inconel 600	76.83	3SK12	CMC matrix	14656-42	1800	1.5	75	
ISTAT-2022-039	Inconel 600	76.83	3SK13	CMC matrix	14656-43	1700	1.5	50	EDX
ISTAT-2022-040	Inconel 600	76.83	3SK14	CMC matrix	14656-44	1700	1.5	100	EDX
ISTAT-2022-041	Inconel 600	76.83	3SK15	CMC matrix	14656-45	1700	1.5	200	EDX
ISTAT-2022-042	Inconel 600	76.83	3SK16	CMC matrix	14656-46	1600	1.5	50	
ISTAT-2022-043	Inconel 600	76.83	3SK17	CMC matrix	14656-47	1600	1.5	100	
ISTAT-2022-044	Inconel 600	76.83	3SK18	CMC matrix	14656-48	1600	1.5	200	
ISTAT-2022-045	N5-	63.45	3SI10	CMC matrix	14656-49	1800	1.5	25	
ISTAT-2022-046	N5-	63.45	3SI11	CMC matrix	14656-50	1800	1.5	50	microprobe and EDX
ISTAT-2022-047	N5-	63.45	3SI12	CMC matrix	14656-51	1800	1.5	75	microprobe and EDX
ISTAT-2022-048	N5-	63.45	3SI13	CMC matrix	14656-52	1700	1.5	50	EDX
ISTAT-2022-049	N5-	63.45	3SI14	CMC matrix	14656-53	1700	1.5	100	EDX
ISTAT-2022-050	N5-	63.45	3SI15	CMC matrix	14656-54	1700	1.5	200	EDX
ISTAT-2022-051	N5-	63.45	3SI16	CMC matrix	14656-55	1600	1.5	50	
ISTAT-2022-052	N5-	63.45	3SI17	CMC matrix	14656-56	1600	1.5	100	
ISTAT-2022-053	N5-	63.45	3SI18	CMC matrix	14656-57	1600	1.5	200	
ISTAT-2022-054	Hast X	48.1	3SJ10	CMC matrix	14656-58	1800	1.5	25	
ISTAT-2022-055	Hast X	48.1	3SJ11	CMC matrix	14656-59	1800	1.5	50	

8. References

1 P.R. Subramanian T.B. Massalski, H. Okamoto, L. Kacprzak, "Binary Alloy Phase Diagrams, second ed., ," ASM International, Materials Park, OH (1990).

2 Americal Society of Test Methods (ASTM), "(ASTM C1360) Standard Test Method for Monotonic Tensile Strength Testing of Continuous Fiber- Reinforced Advanced Ceramics With Solid Rectangular Cross Section Test Specimens at Elevated Temperatures", (2018).

3 Prakash Jadhav and Chhaya Lande, "Asymmetric Four Point Bend Test Method for Interlaminar Shear Strength in Ceramic Matrix Composites," Materials Science Forum 1094, 19-24 (2023).

4 American Society of Test Methods (ASTM), "(ASTM C1359) Standard Practice for Constant-Amplitude, Axial, Tension-Tension Cyclic Fatigue of Continuous Fiber-Reinforced Advanced Ceramics at Ambient Temperatures Standard Practice for Constant-Amplitude, Axial, Tension-Tension Cyclic Fatigue of Continuous Fiber-Reinforced Advanced Ceramics at Ambient Temperatures1", (ASTM, 2017).

5 J. Crank, *The Mathematics of Diffusion*. (Clarendon Press, 1979).